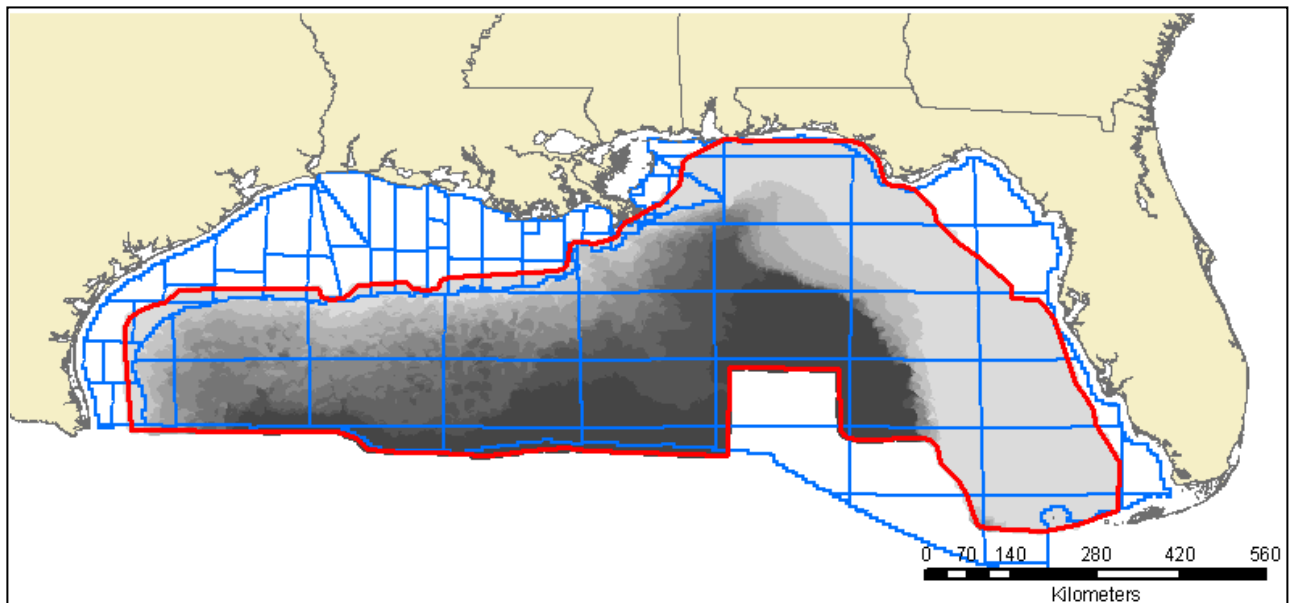


## Preliminary Evaluation of In-Place Gas Hydrate Resources: Gulf of Mexico Outer Continental Shelf

---



U.S. Department of the Interior  
Minerals Management Service  
Resource Evaluation Division  
February 1, 2008

**Front Cover:**

Map of Gulf of Mexico Region study area (outlined in red) with bathymetric color shaded grid as background.

# **Preliminary Evaluation of In-Place Gas Hydrate Resources: Gulf of Mexico Outer Continental Shelf**

---

**Compiled by:**

**Matthew Frye**

**U.S. Department of the Interior  
Minerals Management Service  
Resource Evaluation Division**

## **Acknowledgements**

This report documenting the methodology and preliminary results of the in-place gas hydrate assessment for the United States (U.S.) Gulf of Mexico is the culmination of several years of dedicated effort. The Resource Evaluation Division of the Minerals Management Service gratefully acknowledges the following scientists for their contributions:

Tim Collett, Rick Colwell, Richard Desselles, Barry Dickerson, Scott Edwards, Dick Fillon, John Grace, Jeff Hanor, Jesse Hunt, Gordon Kaufman, Gary Lore, Charlie Paull, Pulak Ray, Carolyn Ruppel, Roger Sassen, Jack Schuenemeyer, Bill Shedd, and Dendy Sloan.

The Methodology chapter (Chapter II) and Appendices A, B, C, D, E and G were authored by a core group of non-MMS contractors that includes John Grace, Gordon Kaufman, and Jack Schuenemeyer.

Any use of trade name, product, or professional services is for descriptive purposes only and does not imply endorsement by the U.S. Government.

# Contents

<b>Acknowledgements</b> .....	ii
<b>List of Figures</b> .....	v
<b>List of Tables</b> .....	vii
<b>Acronyms</b> .....	viii
<b>Executive Summary</b> .....	ix
<b>I. Introduction</b> .....	1
Gas Hydrate Assessment of the Outer Continental Shelf .....	1
Jurisdiction .....	1
OCS Resource Assessments .....	1
What is Gas Hydrate? .....	1
Previous Studies .....	2
Formation and Occurrence of Gas Hydrate .....	2
Production of Gas Hydrate .....	3
Probabilistic Nature of Resource Assessment .....	4
<b>II. Methodology</b> .....	5
Introduction .....	5
Basic Geologic Data .....	7
Charge Module .....	13
A. The Generation Model .....	14
1. Model Structure .....	14
2. Quantity of Organic Carbon in Sediments in the Study Area .....	15
3. Construction of Methanogenic Productivity Function .....	17
a. Modeling Methane Productivity .....	18
b. Model of Methanogenic Productivity of a Single Species of Methanogenic Archaea .....	19
c. Collective Impact of a Community of Different Methanogenic Species of Productivity .....	19
d. Methanogenic Productivity at the Seafloor .....	21
e. Methanogenic Productivity in Buried Sediments .....	23
f. Determining Sediment Permeability at Depth .....	24
g. Determination of the Temperature of Buried Sediment .....	29
h. Asymptotic Organic Carbon Conversion Efficiency .....	29
4. Modeling Generation .....	31
a. Partitioning of Stratigraphic Column .....	32
b. Determination of Generated Volumes of Biogenic Methane .....	34
B. Post-Generation Migration of Biogenic Gas .....	35
1. Spatial Redistribution Submodel .....	37
a. Estimation of Migration Catchment Areas .....	37
b. 100 Percent Dip-Driven Redistribution of Methane within a Catchment .....	40
c. Mixing Ratio for Vertical vs. Dip-Driven Migration .....	42
2. Migration Efficiency Submodel .....	43
a. Migration Efficiency Analysis for Two Conventional Shelf Plays .....	44
b. Broader Analysis of Shelf Play Migration Efficiencies .....	45
c. Estimation of Distribution of Migration Efficiency .....	48
C. Thermogenic Charge .....	49
Container Module .....	50

A. Estimating the Thickness of the Gross Hydrate Stability Zone .....	50
1. Influence of Local Salt .....	51
2. Geothermal Gradient.....	53
3. Water Bottom Temperature.....	56
4. Gas Chemistry.....	57
5. Specification of Final Model for Estimating the Gross HSZ .....	59
B. Estimating the Net Hydrate Stability Zone .....	62
1. Estimating the Thickness of the Undersaturated Zone.....	62
2. Calculating the Thickness of the Net Hydrate Stability Zone.....	64
Concentration Module.....	66
A. Calculation of Matrix Porosity of the Net Hydrate Stability Zone .....	66
B. Calculation of Fracture Porosity in the Net Hydrate Stability Zone .....	67
C. Calculation of the Hydrate Saturation as a Fraction of Void Space.....	67
D. Estimation of Hydrate Concentration in the Net Hydrate Stability Zone .....	69
Integration Module.....	71
A. Estimation of In-Place Hydrates at Reservoir Temperature and Pressure .....	71
B. Conversion of In-Place Hydrate Volumes to Standard Temperature and Pressure.....	71
C. Aggregation of Cell Results to Larger Geographic Aggregates.....	73
<b>III. Underlying Geologic Data, Analysis, and Framework .....</b>	<b>75</b>
Seafloor Bathymetry .....	76
Surficial Seismic Anomalies .....	77
Top of Salt (Basement) .....	79
Sand Distribution .....	81
<b>IV. Results .....</b>	<b>85</b>
In-Place Resources .....	85
Aggregation.....	86
Sand Reservoirs.....	87
Map View.....	88
Disclaimer .....	89
<b>V. Future Work .....</b>	<b>91</b>
<b>References .....</b>	<b>192</b>
<b>Appendixes</b>	
A. Derivation of Productivity Function for a Single Specie.....	A-1
B. Model of Methanogenic Productivity of a Single Species of Methanogenic Archaea.....	B-1
C. Derivation of Productivity Function for a Community of Multiple Species.....	C-1
D. Method for Recovering Price and Sowers Data.....	D-1
E. Conversion of Price and Source Units to Units Used in Generation Model.....	E-1
F. MMS Methodology for Accumulation Density.....	F-1
G. Operating Instructions and Description of Programs.....	G-1

# List of Figures

## I. Introduction

Figure 1: Gas hydrate phase stability diagram for the marine environment (modified from Kvenvolden, 1993) .....	3
---	---

## II. Methodology

Figure 2: Water depth mapped across the area included in the study .....	6
Figure 3: Diagram of the system used to evaluate the volume of in-place marine methane hydrates in the Gulf of Mexico .....	7
Figure 4: Water depth in Green Canyon.....	9
Figure 5: distribution of water depth in Green Canyon .....	9
Figure 6: Sediment thickness (water bottom to top of basement) in Green Canyon area.....	10
Figure 7: Distribution of sediment thickness in Green Canyon.....	10
Figure 8: Percent sand in 610 m below seafloor in Green Canyon .....	11
Figure 9: Distribution of percent sand in 610 m below seafloor in Green Canyon .....	12
Figure 10: Location of buffered surficial seismic anomalies in Green Canyon .....	12
Figure 11: Structure of the charge module .....	13
Figure 12: Schematic of biogenic generation model .....	15
Figure 13: Location of DSDP Leg 96 holes used for the data on distribution of total organic carbon and organic matter quality.....	16
Figure 14: Probability distribution of 773 observations on total organic carbon from Leg 96 cores .....	16
Figure 15: Distribution of 681 observations on total organic carbon from Leg 96 cores, omitting 91 outlier observations from cores 614A and 615 .....	17
Figure 16: Distribution of 681 observations on total organic carbon from the Leg 96 cores against the fitted Weibull distribution.....	17
Figure 17: General relationship between methanogenic productivity and temperature .....	19
Figure 18: A mesa-like function in an interval about a maximum value.....	20
Figure 19: Smooth pasting of three functions to capture qualitative features of productivity of a community of methanogen species.....	21
Figure 20: Data from Price and Sowers (2004) used to interpolate productivity of methanogens at seafloor temperature .....	22
Figure 21: Distribution of $A_{SF}(T_{SF}(WD))$ based on analysis of Price and Sowers data.....	23
Figure 22: Scatter plot of permeability vs. depth for 9,462 observations from GOM commercial oil and gas reservoirs.....	25
Figure 23: Fit of sand permeability (measured in millidarcies) as a function of depth .....	26
Figure 24: Shale porosity versus depth at mean values of parameters, based on Spinelli et al. (2004).....	27
Figure 25: Estimated shale permeability versus estimated porosity .....	28
Figure 26: Shale permeability variation with depth at parameter means.....	29
Figure 27: Empirical distribution of values of $((S1 + S2) * 100) / TOC$ .....	30
Figure 28: Distribution of $((S1 + S2) \times 100) / TOC$ in milligrams of hydrocarbons per gram of organic carbon .....	31
Figure 29: Locations of 100 randomly located pseudowells used in the construction of distributions of sediment thicknesses by geologic time/rock units over the study area.....	33
Figure 30: Distribution of the percent of gross sedimentary thicknesses encompassed by each of the five geologic time/rock units in the study.....	33
Figure 31: Mean volume of generated biogenic gas in Green Canyon.....	35
Figure 32: A schematic diagram of the migration model, showing the interaction of the spatial and efficiency submodels .....	36
Figure 33: Catchment basins where the basement surface has minimal effect on the stratal dip of the sedimentary column.....	38
Figure 34: Steps to create catchment areas for the dip-driven migration sub-model based on the geometry of the basement structure map .....	38
Figure 35: Relation of depth to basement and catchment areas estimated for dip-driven migration analysis .....	39

Figure 36: A schematic of the connection between the summation of gas generation in a catchment to the submodel that redistributes all generated gas in the catchment based on a function of dip.....	40
Figure 37: Estimated curvature of the true vertical depth to top of basement surface.....	41
Figure 38: Algorithm for assigning 100-percent dip-driven charge to a cell.....	42
Figure 39: Estimated mean charge, based on 60/40 dip-driven/vertical migration ratio, in Green Canyon.....	43
Figure 40: Outlines of hydrocarbon limit and play limit for Middle Pleistocene Progradational play.....	45
Figure 41: Probability distribution for the migration/trapping efficiency parameter .....	49
Figure 42: Relationship between geothermal gradient and heat flow from a database of observations on both measures taken from 6,815 marine observations from the “Global Heat Flow Data Base” ..	54
Figure 43: Texas Tech geothermal gradient data against (semitransparent) water depth.....	55
Figure 44: Scatter plot showing an absence of a statistically significant relationship in the 62 Texas Tech data point on geothermal gradient and water depth .....	55
Figure 45: Raw Texas Tech geothermal gradient data and fitted beta distribution .....	56
Figure 46: Raw data on (decimal) percent methane gas from samples located in cells identified as seismic surficial anomalies.....	57
Figure 47: Raw data on (decimal) percent methane gas from samples located outside cells identified as surficial anomalies.....	58
Figure 48: Mean thickness of the gross hydrate stability zone for Green Canyon .....	60
Figure 49: Relative frequency distribution of the mean thickness of the gross HSZ in Green Canyon (mean thickness = 233 meters).....	60
Figure 50: Mean gross HSZ thickness vs. water depth in Green Canyon .....	61
Figure 51: Mean gross HSZ thickness vs. (vertical) distance from salt in Green Canyon .....	61
Figure 52: Influence of shallow local salt (thinning the gross HSZ) exceeding the influence of water depth .....	62
Figure 53: Thickness of the undersaturated zone in Green Canyon (units in meters).....	64
Figure 54: Relative frequency distribution of the thickness of the undersaturated zone in the Green Canyon area (mean thickness = 152 meters) .....	64
Figure 55: Mean net hydrate stability zone thickness in the Green Canyon study area .....	65
Figure 56: Relative frequency distribution of the thickness of the net hydrate stability zone in the Green Canyon area (mean thickness = 123 meters).....	65
Figure 57: Sand porosity and depth from KC 151 used to estimate sand porosity for determination of void space.....	67
Figure 58: Histogram of the combined BR-994 and BR-995 gas hydrate saturation (1-water saturation).....	68
Figure 59: Histogram of the fraction of gas hydrate saturation, Mallik M5L38 well.....	69
Figure 60: Hydrate concentration as a (decimal) percent of bulk sediment volume of the net HSZ in the Green Canyon study area.....	70
Figure 61: Relative frequency distribution of the hydrate concentration as a decimal percent of bulk sediment volume in the net HSZ, Green Canyon area (mean = 0.095) .....	70
Figure 62: Probability distribution of conversion factor to STP .....	72
Figure 63: Distribution of mean gas hydrate volume at STP in Green Canyon (values listed in trillion cubic feet).....	72
Figure 64: Relative frequency distribution of mean in-place gas hydrate volume in Green Canyon (values in BCF per model cell).....	73

### III. Underlying Geologic Data, Analysis, and Framework

Figure 65: Seismic data coverage available for the hydrate assessment .....	75
Figure 66: Seafloor bathymetry across the study area.....	76
Figure 67: Amplitude extraction of the seafloor in the Gulf of Mexico .....	77
Figure 68: Location of all deepwater seafloor anomalies identified in the Gulf of Mexico .....	78
Figure 69: Seismic section with depth units in two-way time (one second of water = 743.7 meters).....	78
Figure 70: Sub-regional example of surficial amplitude anomaly polygons and the 762-m buffer installed for better representation of the anomalies with respect to the model’s cellular structure.....	79
Figure 71: Subseafloor depth to top of salt (or basement) in meters .....	80
Figure 72: Gulf of Mexico basin map showing present day allochthonous salt and depositional limit of autochthonous salt.....	81
Figure 73: Location of wells included in sand count study .....	82



Figure 74: Distribution of sand in the shallow subsurface .....	83
---	----

#### IV. Results

Figure 75: Distribution of in-place gas hydrate resources, Gulf of Mexico .....	85
Figure 76: Mean in-place gas hydrate volume in trillion cubic meters .....	86
Figure 77: Sand-only gas hydrate resource volume, Gulf of Mexico (trillion cubic meters) ..	89

#### Appendix B

Figure B.1: A plot of $f_2(x)=C \times \exp\{-\lambda x^\beta\}x^\alpha$ versus x .....	B-2
Figure B.2: Modified Arrhenius' Law for rate of methane production by a single species of methanogen (in grams of methane/gram of organic carbon/million years) as a function of sediment temperature.....	B-3

## List of Tables

#### II. Methodology

Table 1: Divisions of Stratigraphic Column.....	32
Table 2: Parameters of Gamma Distributions in the Relative Thickness of Each Stratigraphic Interval .....	34
Table 3: Algorithmic Summary of Charge Module.....	34
Table 4: MM7 Progradational Play – Migration/Trapping Efficiency Analysis .....	46
Table 5: Middle Pleistocene Progradational Play – Migration/Trapping Efficiency Analysis.....	47
Table 6: Estimates of Accumulation Density for 18 Unaggregated GOM Shelf Plays.....	48
Table 7: Estimates of Accumulation Density for 9 Aggregated GOM Shelf Plays.....	48
Table 8: Parameter Estimates for Eq. (2.5) .....	56
Table 9: Parameters for Phase Stability Expression in Eq. (2.7).....	57
Table 10: Rescaling of Gas Chemistry Beta Distributions .....	58
Table 11: Parameter Estimates for Eq. (3.2) .....	66
Table 12: Wells Used in the Analysis of Distributions of Shale and Sand Matrices and Associated Summary Statistics .....	68
Table 13: Distributions on Percent Hydrate Saturation of by Type of Void Space.....	69

#### IV. Results

Table 14: In-place Gas Hydrate Resources for the Gulf of Mexico .....	85
Table 15: In-place Gas Hydrate Resources for the Four Data Areas, Gulf of Mexico (trillion cubic feet) .....	87
Table 16: Sand-only Gas Hydrate Resources for the Gulf of Mexico (trillion cubic feet) .....	88

#### Appendixes

Table D.1: Maintenance Data Recovered from Figure 20.....	D-2
Table D.2: Metabolic Rate Mean Values Adjusted to Seafloor Temperature .....	D-3
Table D.3: Standard Deviations Imputed from Individual Study CI WIDTHS.....	D-4
Table D.4: Standard Deviations of Sample Means Adjusted to Seafloor Temperature.....	D-5
Table D.5: Between Studies Summary Statistics for Temperature Adjusted Metabolic Rates ( $10^{-6}$ Units).....	D-5
Table E.1: Density of Microorganism Cells in Sediments .....	E-1
Table E.2: Productivity of Methanogens in Sediments .....	E-2

## Acronyms

BOE	barrels oil equivalent
DSDP	Deep Sea Drilling Project
ft <sup>3</sup>	cubic foot
EPAct2005	Energy Policy Act of 2005
GB	Garden Banks
GC	Green Canyon
GERG	Geochemical and Environmental Research Group
GIS	geographic information system
GOM	Gulf of Mexico
GOMR	Gulf of Mexico Region
HSZ	hydrate stability zone
KC151	Keathley Canyon Block 151
km <sup>2</sup>	square kilometer
m	meter
mbsf	meters below seafloor
md	millidarcies
mg/g	milligram per gram
MLE	maximum likelihood estimate
MM7P	Middle Miocene 7 Progradational
MMS	Minerals Management Service
MPLP	Middle Pleistocene Progradational
M/S	Milkov and Sassen
MWD	measured while drilling
NaCl	sodium chloride
OCS	Outer Continental Shelf
OCSLA	Outer Continental Shelf Lands Act
ppt	parts per thousand
PT	pressure-temperature
RTP	reservoir temperature and pressure
STP	standard temperature and pressure
TCF	thousand cubic feet
TOC	total organic carbon
TWT	two-way travel time
USGS	United States Geological Survey
UZ	undersaturated zone
WBT	water bottom temperature

## Executive Summary

This report documents the Minerals Management Service's (MMS) efforts to date in developing a model for performing assessments of potential quantities of methane hydrates located on the Outer Continental Shelf (OCS). This initial effort focused on modeling in-place quantities of biogenically-sourced gas hydrate in the Gulf of Mexico (GOM). At this time, estimates of in-place gas hydrate resources are presented herein without regard to technical or economical recoverability. In the future, the model will be modified to incorporate thermogenically generated methane, will be expanded to include the rest of the OCS, and will stochastically estimate technically and economically recoverable resources.

Gas hydrates are ice-like crystalline substances occurring in nature where a solid water lattice accommodates gas molecules (primarily methane, the major component of natural gas) in a cage-like structure, known as a clathrate. Gas hydrates form in the shallow subsurface along continental margins and below the permafrost in polar regions, where pressure and temperature conditions provide a zone of hydrate stability (referred to as the *hydrate stability zone*). On the GOM OCS, gas hydrates can form in water depths in excess of about 400 meters, provided that an adequate supply of methane is available and that temperature and salinity are not excessive. The thickness of the hydrate stability zone in the GOM has been modeled in excess of 1,000 meters. Due to excessive temperatures and pressures, gas hydrate will not form at seafloor depths that far exceed 1,000 meters.

The MMS regional personnel in the GOM assessed an area of approximately 450,000 square kilometers where pressure and temperature conditions provide a stable physical environment for the formation of gas hydrate, and where seismic data are available for subsurface interpretation. Supporting subsurface information (wellbore, geological, geochemical, and paleontological) were obtained from public, proprietary, and unpublished sources. Hydrates are predicted to accumulate in sandstone reservoirs, shales, and fracture reservoirs within the hydrate stability zone.

The assessment model structure consists of over 200,000 cells that measure 2.32 km<sup>2</sup> each (5000 feet (ft) x 5000 ft). This stochastic model incorporates the uncertainty of many input variables through multiple trial runs, producing a distribution of results where the mean is the expected value. The model methodology is based on mass balance, where inputs include an initial endowment of organic carbon, a conversion productivity function, a volume of candidate reservoir rock, and a fraction of the rock volume that allows for hydrate concentration. Aggregated model results are based on 1,000 Monte Carlo trials.

The total volume of biogenically generated in-place gas hydrate on the GOM OCS using this methodology is projected to range from 11,112 trillion cubic feet (TCF) to 34,423 TCF, with a mean estimate of 21,444 TCF. The geographically-referenced model projects relatively large volumes of these resources to accumulate near the margins of minibasins and at the front of the Sigsbee Escarpment. The MMS model predicts that, of the mean estimate, 6,717 TCF will reside in sandstone reservoirs, and the remaining 14,727 TCF will reside in shale and fractured reservoirs.



# Chapter I. Introduction

## Gas Hydrate Assessment of the Outer Continental Shelf

This report summarizes the Minerals Management Service's (MMS's) effort to date in the development of a methodology and stochastic model to assess the natural gas hydrate resource potential on the Outer Continental Shelf (OCS). This initial release contains in-place results from the Gulf of Mexico (GOM) basin, with similar results to be delivered from the Atlantic, Pacific, and Alaskan basins in the near future. Full documentation of the assessment model methodology and a mathematical description of model version 3.38 are also included in this report.

Similar to previous large scale assessments (Collett, 1995), this report identifies only in-place gas hydrate resources, with limited reference to technical or economic recoverability. The recoverable resources will be modeled in the next phase of the assessment and identified in a future release.

## Jurisdiction

The [Outer Continental Shelf Lands Act](#) (OCSLA) of 1953 provides for the jurisdiction of the United States over the submerged lands of the OCS, and authorizes the Secretary of the Interior to lease such lands for mineral development. In 1982, the Secretary of the Interior designated the MMS as the administrative agency responsible for the leasing and development of all mineral operations on the OCS. Under the OCSLA, the MMS implements an OCS oil and gas exploration and development program that currently provides the Nation with 30 percent of its domestic oil production and 20 percent of its domestic natural gas production.

Since its original enactment in 1953, the OCSLA has been amended several times, most recently as a result of the Energy Policy Act of 2005 (EPAAct2005). To promote natural gas production from gas hydrate resources on the OCS and Federal lands in Alaska, Congress included provisions in the EPAAct2005 to address gas hydrate production incentives (section 353), and provide for a continued program of methane hydrate research (section 968). Section 353 of EPAAct2005 provides for a program of royalty relief if the Secretary determines that such royalty relief would encourage production of natural gas from gas hydrate resources.

## OCS Resource Assessments

The MMS periodically conducts assessments of undiscovered resources in order to optimize management of the energy resources on the OCS. Historically, these assessments have largely focused on conventionally recoverable natural gas and crude oil quantities. Since its inception in 1982, the MMS has completed systematic assessments of these conventional resources on the OCS in the years 1985, 1990, 1995, 2000, and 2006.

In addition to conventional resources, the 1995 assessment included for the first time an appraisal of in-place gas hydrate resources. The hydrate component of the assessment was lead by the United States Geological Survey (USGS) and included an analysis of any U.S. jurisdiction where conditions were favorable for hydrate formation, including the Federal OCS and permafrost regions in Alaska. The MMS plans to conduct a comprehensive assessment of the Nation's unconventional natural gas hydrate resource base when the methodology and model structure described herein are finalized.

## What is Gas Hydrate?

Gas hydrates are ice-like crystalline substances occurring in nature where a solid water lattice accommodates gas molecules (primarily methane, the major component of natural gas) in a cage-like structure, also known as clathrate. Gas hydrates form under conditions of relatively high pressures and low temperatures, such as those found in the shallow subsurface under many of the world's oceans. One cubic foot of hydrate at reservoir temperature and pressure yields approximately 160 cubic feet (ft<sup>3</sup>) of gas at atmospheric temperature and

pressure. The amount of natural gas in methane hydrate worldwide is estimated to be far greater than the entire world's conventional natural gas resources (Collett, 2002).

### **Previous Studies**

Gas hydrate represents a potentially enormous untapped domestic energy source. The most comprehensive estimate for the mean in-place amount of gas hydrate in the United States was developed by Collett (1995), who presented a mean value of  $3.2 \times 10^{17}$  ft<sup>3</sup> (320,222 trillion cubic feet). This estimate was revised by Collett (1997) to approximately  $2.0 \times 10^{17}$  ft<sup>3</sup> based on data from Ocean Drilling Program Leg 164. Historical global estimates of marine hydrates have varied considerably, ranging from  $1.1 \times 10^{17}$  ft<sup>3</sup> (Meyer, 1981) to  $2.7 \times 10^{20}$  ft<sup>3</sup> (Dobrynin et al., 1981). Current global estimates of both marine and nonmarine hydrate accumulations are now believed to be close to  $7.0 \times 10^{17}$  ft<sup>3</sup> (Collett, 2002). Localized estimates for the GOM range from approximately  $4.2 \times 10^{14}$  ft<sup>3</sup> (Milkov and Sassen, 2001) to  $3.8 \times 10^{16}$  ft<sup>3</sup> (Collett, 1995). The Milkov and Sassen (2001) estimate is based on an area of only 59,000 square kilometers (km<sup>2</sup>), compared to an area of 240,000 km<sup>2</sup> for the Collett (1995) assessment.

Prior to the 1960's, gas hydrate was studied as an academic research interest and for its role as a nuisance in pipeline transmission of natural gas and as a safety hazard in drilling conventional oil and gas wells. In the 1960's, the first suspected production from gas hydrate was reported from the Messoyakha field in western Siberia. Throughout the 1980's and in recent years, gas hydrate has become a topic of increasing interest, particularly in countries such as Japan and India where domestic sources of natural gas are very limited. Although a significant amount of knowledge concerning the physical and chemical properties of gas hydrate and its formation and recognition criteria have been developed, numerous technical challenges remain before gas hydrate can be considered as a viable energy source.

### **Formation and Occurrence of Gas Hydrate**

Gas hydrate forms only within a specific range of pressure and temperature conditions and when a sufficient supply of natural gas and water is present. A pressure–temperature phase diagram that shows the zone (PT-window) of pressure and temperature combinations where gas hydrate is stable as shown in figure 1 (Kvenvolden, 1993) for deepwater marine sediments at a given water depth. The location and dimension of the PT-window of gas hydrate stability is affected by the composition of the gas, the pore-water salinity, and the local temperature gradient. In the GOM particularly, the presence of large salt features reduces the size of the hydrate stability zone and adds significant complexity to its shape.

The formation and preservation of gas hydrate follow many of the same principles of conventional petroleum systems—i.e., requirements for an effective source of methane, a migration pathway, suitable reservoir rock, and seal. However, the existence and maintenance of a specific pressure, temperature, and chemical regime for the reservoir rock becomes an additional condition. As sufficient quantities of natural gas migrate through a favorable P-T regime for gas hydrate in the presence of sufficient quantities of water and other suitable chemical conditions, gas hydrates form. Gas hydrate has been observed as a disseminated accumulation within the pore space of sedimentary units, as well as in a more massive form that is hosted in faults, fractures, and nodules. Hydrate-bearing sedimentary sections range in thickness from a few centimeters to tens of meters (Collett, 2002). Although most of the marine gas hydrate occurrences are in clayey sediments with very little permeability having low gas hydrate concentrations, the GOM holds the possibility of having sand reservoirs that could have high gas hydrate saturations.

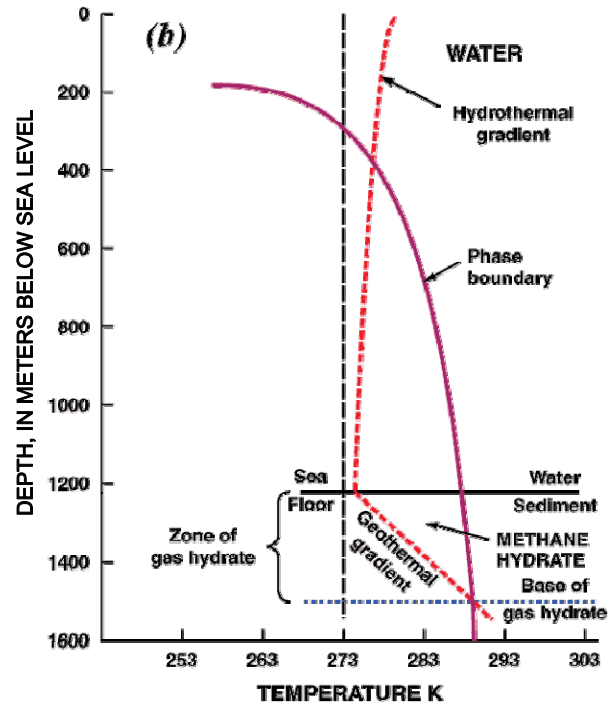
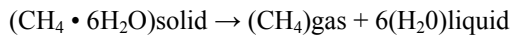


**Figure 1. Gas hydrate phase stability diagram for the marine environment (modified from Kvenvolden, 1993).**

### Production of Gas Hydrate

The dissociation of gas hydrate is represented by the following expression:



The energy value of the produced gas is ten times what is needed for the dissociation of hydrate (Holder et al., 1982). Depressurization, thermal stimulation, and inhibitor injection, or a combination of these methods, have been considered as possible methods of production for gas hydrates. Recent production testing in the Mallik project in Canada utilized a combination of depressurization and thermal stimulation. Depressurization has been judged to be the most economic method (Sloan, 1998), and this is reinforced by the production testing of the Mallik project (Dallimore and Collett, 2005). Collett (2002) points out that the extraction of gas by depressurization may suffer from the formation of ice or reformation of gas hydrate due to the endothermic property of gas hydrate dissociation.

Our knowledge on gas hydrate production from natural reservoirs comes primarily from laboratory studies and modeling using numerical simulators. However, these simulations and modeling efforts utilize real data from the field or production test data, such as that obtained from the Mt. Elbert project on the North Slope of Alaska, the Mallik production test in Canada, and borehole information from suspected hydrate accumulations in the deepwater GOM. The short-term tests at Mt. Elbert and Mallik have answered many questions, while raising many more that can only be addressed by a series of long-term production tests in a variety of settings. Knowledge gathered from these studies about the thermodynamics and the kinetics of formation and dissociation of methane hydrate will influence production strategies. The effect of sediment properties on the behavior of hydrate dissociation and resultant water and gas flow through the reservoir needs to be established for application of large-scale simulators to evaluate production capabilities (Moridis et al., 2006). The biggest need, therefore, is for a controlled and extended production test from a natural hydrate accumulation to provide a meaningful dataset to calibrate and validate emerging models.

Though the resource base is potentially huge, there is currently great uncertainty about the quantity of hydrate that can be commercially extracted. It is important to recognize that methane hydrate science is still relatively new. Demonstrating the energy resource potential of gas hydrate poses significant technical challenges. If current obstacles can be overcome, natural gas from hydrate could become an abundant domestic source of energy for the future.

### **Probabilistic Nature of Resource Assessment**

With any resource assessment, there are numerous uncertainties regarding the geologic framework and the petroleum systems analysis of a given area, and their collective effect on the location and volume of undiscovered resources. Specifically, uncertainties include the presence and quality of source rocks, reservoir rocks, and traps; the timing of hydrocarbon generation, migration, and entrapment; and the location, number, and size of accumulations. In this particular assessment of in-place gas hydrate on the OCS, many of these uncertainties associated with conventional oil and gas resources are exacerbated as they are applied to the unconventional, poorly understood, resource base of gas hydrate.

The value and uncertainty associated with many of these factors can be qualitatively expressed (e.g., “there is a high probability that the quality of source rocks is good”). However, in order to develop volumetric resource estimates, the value and uncertainty regarding many factors must be quantitatively expressed. When feasible, each of these factors – including the volumetric resource estimate derived from them – is expressed as a range of values with an associated probability of occurrence.

In order to capture the uncertainty in the evaluation process, the estimate of undiscovered in-place gas hydrate is expressed as a cumulative probability distribution, where a specified volume or more of resources corresponds to a probability of occurrence. The low estimate corresponds to the 95<sup>th</sup> percentile value of the distribution, the mean estimate corresponds to the statistical average of all values in the distribution, and the high estimate corresponds to the 5<sup>th</sup> percentile value of the distribution. As in most stochastic resource assessments, and certainly in one where a new methodology has been developed and deployed, the reader is encouraged to view the mean estimate as the expected value.



## Chapter II. Methodology

### Introduction

This chapter describes the methodology being developed for the assessment of in-place natural gas hydrates in the GOM. At its core, it is a mathematical model that captures essential features of methane hydrate generation and deposition. The model is used to generate maps and numerical outputs of key attributes, and provides a preliminary probabilistic estimate of in-place methane hydrate volumes. The Gulf of Mexico Region (GOMR) office of the MMS produced several of the foundational input data sets and provided overall support for the project. Other experts from a variety of fields contributed both data and advice to development of the model.

Key characteristics of this study are:

- (1) Analytic methods employed are based on mass balance – an input-output analysis. Inputs are the mass of organic carbon available for conversion to methane, the volume of rock that possesses the physical and chemical conditions required to contain hydrates, and the fraction of that rock volume that constitutes effective void space into which hydrates can concentrate.

While there are other possible methodologies, mass balance has two important advantages: it is transparent and allows extreme variable disaggregation. Therefore, as new and better information about total organic carbon in sediments, or heat flow or an improved formulation of hydrate phase relationships becomes available, the system can be easily updated.

- (2) It is cell-based. The study area is 457,933 km<sup>2</sup> and is divided into a grid of 202,079 cells, each 2.32 km<sup>2</sup> (figure 2). The mass balance analysis is applied to each cell, providing a level of spatial resolution that supports detailed mapping.

The spatial distributions of in-place methane hydrates, both in absolute geographic space and its relative spatial distribution (e.g., clustering), have a critical impact on the fraction that will be technically and, ultimately, economically recoverable.

- (3) It is stochastic. Many input variables are treated as uncertain quantities and are assigned probability distributions. In some cases, parameters of these distributions are also treated as uncertain quantities. Consequently, key output variables are also uncertain quantities with probability distributions determined jointly by model structure and these probability distributions.

A fundamental advantage of this approach is that the large, complex model system can use Monte Carlo sampling to generate empirical distributions of key output variables such as the volume of hydrates in place in the GOM. As the number of Monte Carlo trials increases, the empirical distribution of each output variable converges to a probability distribution logically coincident with the model's structure and initial conditions assigned to input variables.

Probability distributions assigned to input variables and to model parameters are, in some cases, derived exclusively from statistical analysis of data, and in other cases, from expert judgment or from a combination of both. Empirical distributions displayed in this report and summary statistics derived from them are based on 1,000 Monte Carlo trials.

A highly disaggregated model-based assessment of in-place hydrates enhances our understanding of the marine gas hydrate resource base and the role of methane hydrates in the Earth's carbon cycle, and leads naturally to a complementary analysis of the fraction of in-place methane that is technically recoverable. The in-place model presented here will be expanded to allow projection of volumes of technically recoverable hydrates from the GOM.

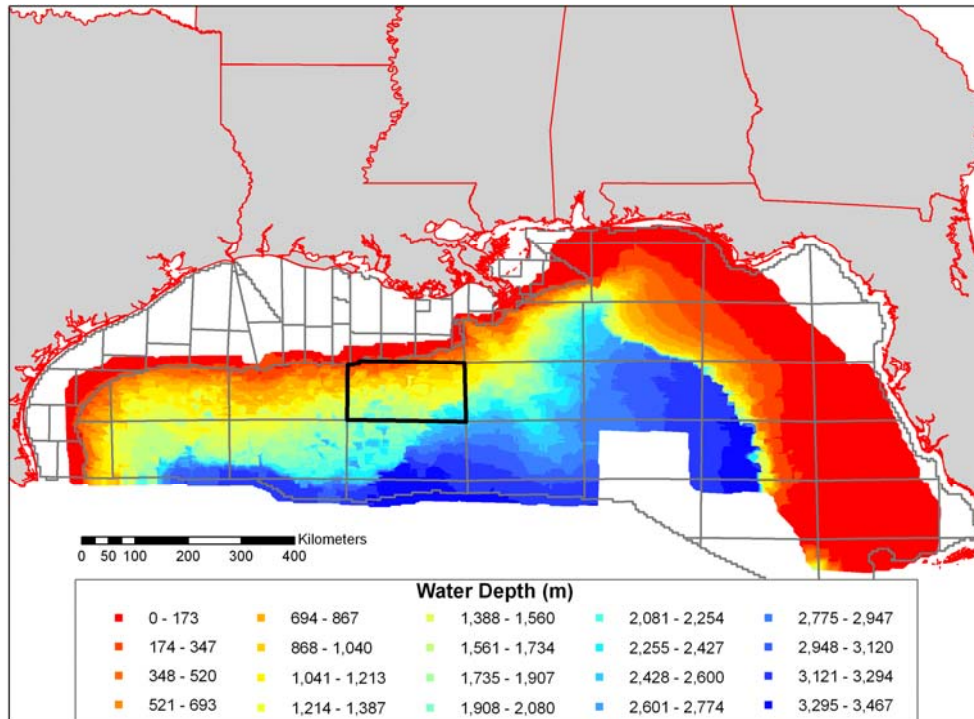


**Figure 2. Water depth mapped across the area included in the study. Areas toward the coast are not included because they do not meet water depth minimums for the occurrence of gas hydrate. Some deep water areas in U.S. waters are excluded because of the absence of seismic data. The Green Canyon protraction area is outlined in black.**

The software application through which the analysis is performed is composed of four modules (see figure 3). Within each of the modules, there are models that either characterize input data or represent biological, chemical, or physical processes or describe output variables. In some cases, a main model may be constructed from two or more sub-models. The four modules are:

- (1) Charge: The charge module contains a generation model and a migration model. A Monte Carlo trial of the generation model produces the amount of biogenic methane produced in each cell at that trial. The migration model aggregates generation into hydrodynamic catchment areas and then spatially redistributes a fraction of the catchment's generated gas at that trial to each cell within it. One thousand such trials yield an empirical probability distribution of the volume of methane charge available to the hydrate stability zone in each cell. Thermogenic gas generation is not modeled.
- (2) Container: The container module determines the bulk volume of rock that can contain hydrates. It provides a probability distribution of gross and net hydrate stability zone (HSZ) thicknesses and the mid-point depth of the net HSZ in each cell. Components of this module represent factors which determine where hydrates may form based on temperature, pressure, and pore-water chemistry.
- (3) Concentration: The concentration module provides a probability distribution of volume of hydrates per unit of bulk rock volume in the net HSZ, conditional on it being charged with methane. It includes models of rock porosity, based on depth and lithology, and of the fraction of void space that can be saturated by methane hydrates.
- (4) Integration: At each Monte Carlo trial, the charge module's output and the volume of candidate void space generated by the container and concentration modules are compared. The smaller of the two volumes is retained and recorded. Executing the model over 1,000 trials yields a distribution of in-place methane hydrates in each cell. A separate module allows aggregation of cell results.

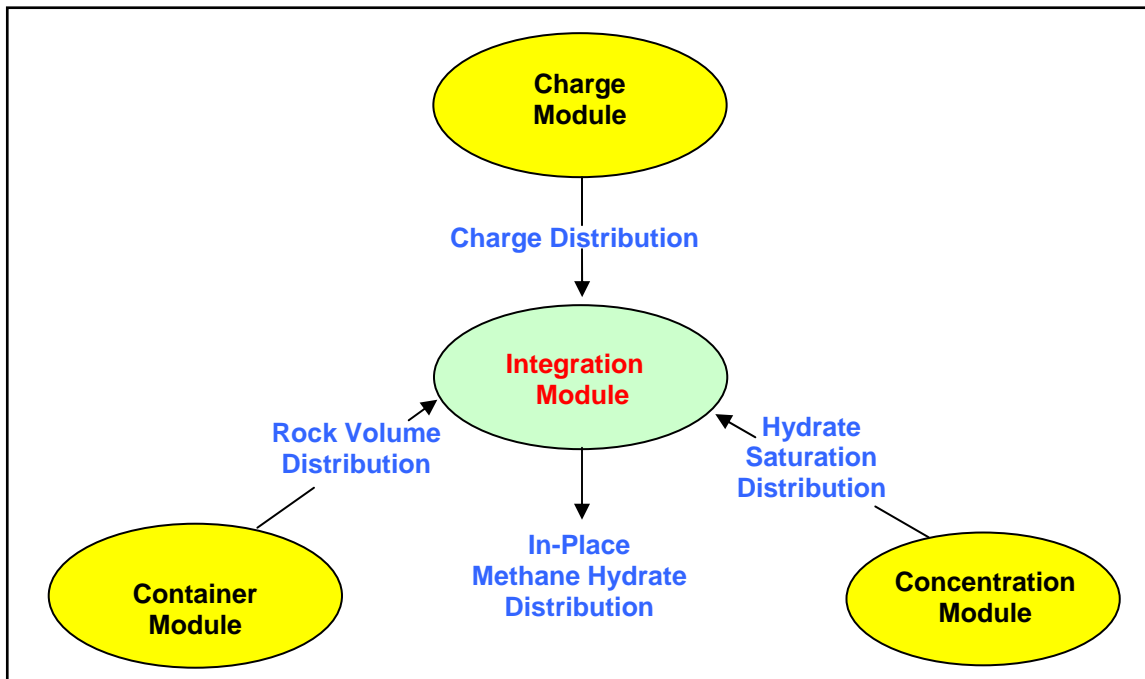


**Figure 3. Diagram of the system used to evaluate the volume of in-place marine methane hydrates in the Gulf of Mexico.**

In the section that follows, the four fundamental data sets used in the evaluation of in-place hydrate in the GOM are described. The four component modules in figure 3 are then described in detail. Two MMS protraction areas, Green Canyon (GC) and Garden Banks, serve as illustrative examples of how the analysis works. Both of these areas are representative of the analysis conducted for the GOM as a whole. The GC protraction area, outlined in black in figure 2, is 21,773 km<sup>2</sup> and contains 9,385 cells. Garden Banks is immediately west of GC and is of similar size and contains a similar number of cells.

### Basic Geologic Data

Evaluation of in-place hydrates in the GOM rests on the data provided by several individuals and groups. Four framework data sets were constructed by MMS personnel in the New Orleans region. Chapter III describes how these data sets were developed. The value of each variable within a cell is represented as a point at the cell centers.

- (1) Bathymetry is derived from the 3-D seismic surveys used by the MMS-GOMR team for the project. Water depth in GC (see figure 4) spans a very large part of the total range of water depth in the entire study area. The distribution of water depth in GC is shown in figure 5. Water depth determines two key variables:
  - (a) Pressures at and below the seafloor, both functions of water depth, are determinants of the thickness of the gross HSZ.
  - (b) Temperature at the seafloor, also a function of water depth, is also a determinant of gross HSZ and plays a role in the biogenic gas generation model.
- (2) Depth to top of basement is interpreted and gridded from the same 3-D seismic data sets by the MMS-GOMR team. Throughout most of the study area, depth to top salt is used to represent depth to top of basement. In several areas south and east of the Sigsbee Escarpment with limited salt, the basement

datum is shifted to specific stratigraphic marker horizons. A map showing the datum shift (see figure 33) and its rationale is provided in the following chapters by the MMS-GOMR team.

Depth to top of basement is used for three purposes:

- (a) Subtracting the bathymetry from the depth to basement yields an isopach of the sedimentary section in each cell, which is used in the biogenic methane generation model.
- (b) The true vertical depth of the basement is used as a surface for estimating the relative dip of strata for the migration model.
- (c) Where the basement is composed of salt, the depth to basement is used to measure the distance to salt, which affects the thickness of the gross HSZ through its influence on both connate water salinity and temperature in the sedimentary section.

Figure 6 shows the thickness of the sedimentary section (from the water bottom to the top of basement) for GC; its distribution is shown in figure 7. Throughout GC, the basement datum is top salt.

- (3) Percent Sand in the top 2,000 feet (610 meters [m]) below seafloor is interpreted from well log and seismic data by the MMS-GOMR team using methods described in Chapter III. The results for GC are shown in figure 8 and figure 9. It is assumed that the top 610 m of section throughout the study area is composed completely of sand and shale.

Sand percent is used in the analysis for two purposes:

- (a) To estimate porosity used in calculating the volume of methane in hydrate-saturated rock in the concentration module.
- (b) To compute a ratio between permeability at the seafloor and buried sediments; this is used in the generation model as an instrumental variable for water flux.

- (4) Surficial Seismic Anomalies were identified by the MMS-GOMR team. These represent areas where a seismic signature associated with present or past venting of methane to the seafloor was identified. The method of identification is described in Chapter III. Beyond the area of the anomalies as mapped, the MMS-GOMR team decided that by surrounding mapped anomalies with a 2,500-ft (762-m) buffer, they more accurately reflect the area where venting occurred or is occurring. The buffered anomalies in GC appear in figure 10. The rationale for this decision is also provided in Chapter III. The buffered anomalies play two roles in the analysis:

- (a) Where anomalies are identified, all available void space in the net HSZ within that cell is filled to saturation with hydrates.
- (b) These anomalies ground-truth the analysis and help calibrate migration efficiency in the charge module.

The buffered anomalies constitute 10.9 percent of the area of Green Canyon.

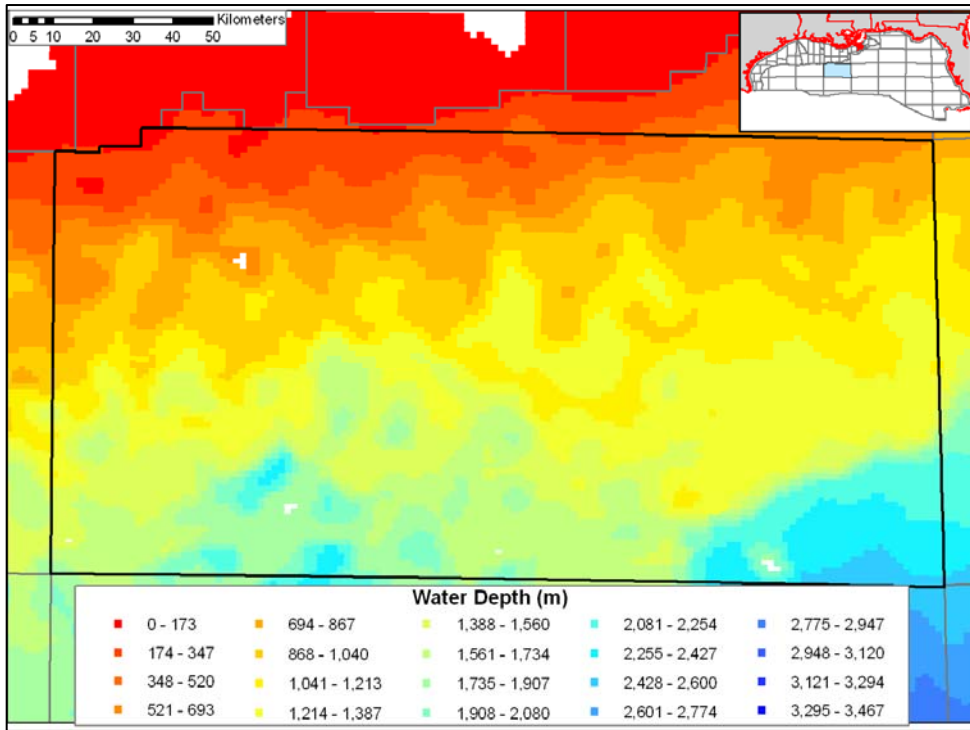


Figure 4. Water depth in Green Canyon.

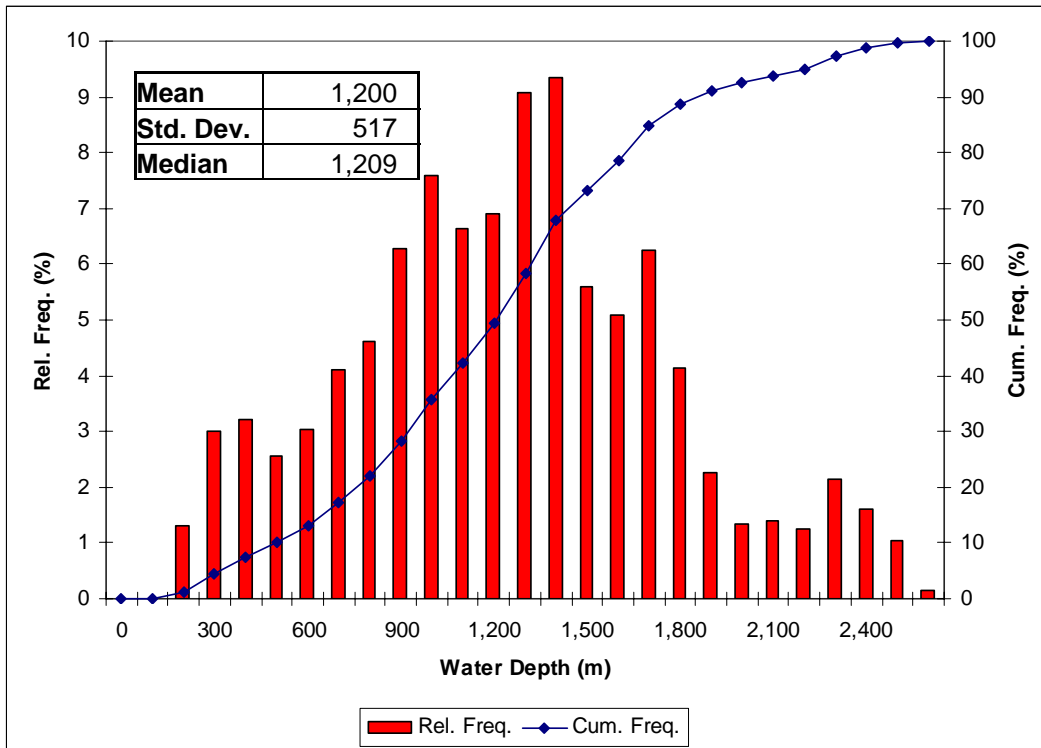


Figure 5. Distribution of water depth in Green Canyon.

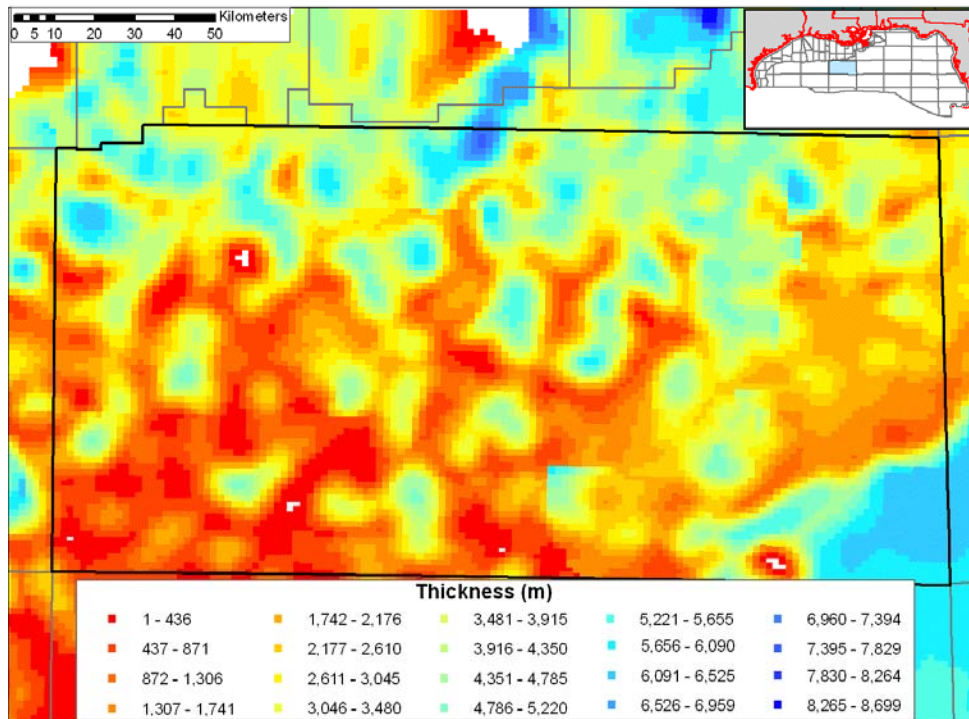


Figure 6. Sediment thickness (water bottom to top of basement) in Green Canyon.

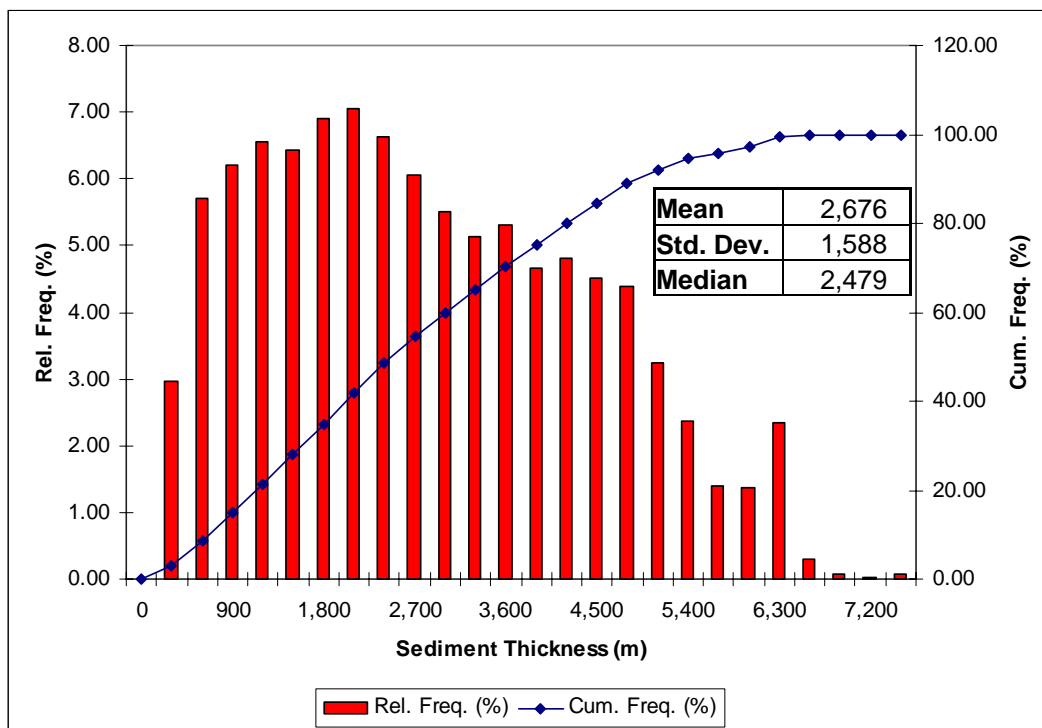
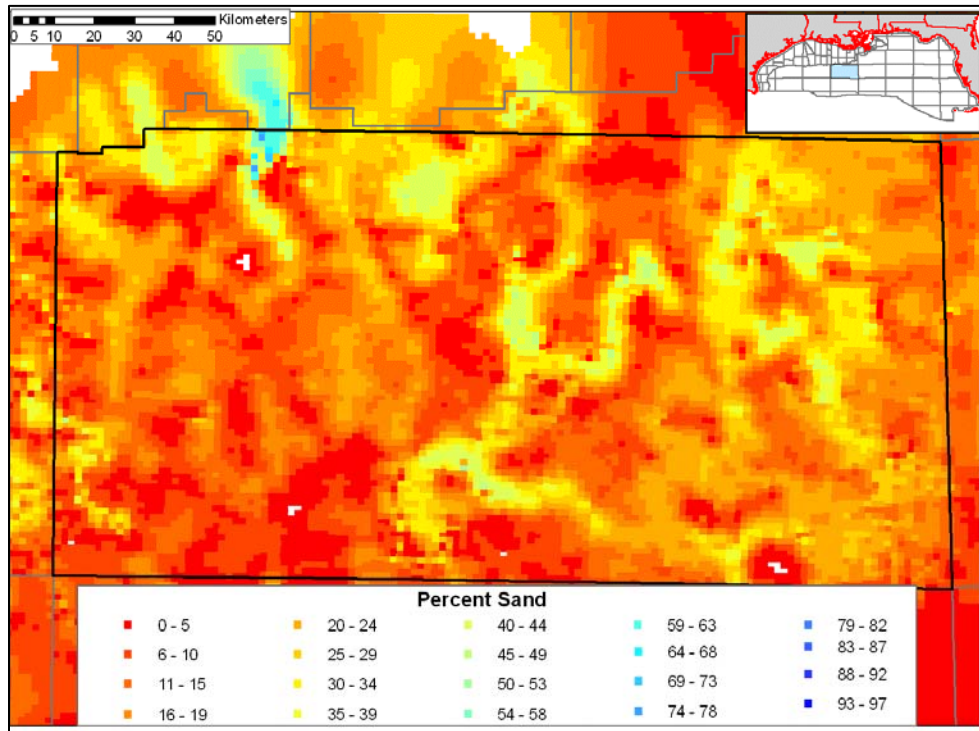


Figure 7. Distribution of sediment thicknesses in Green Canyon.



**Figure 8. Percent sand in 610 m below seafloor in Green Canyon.**



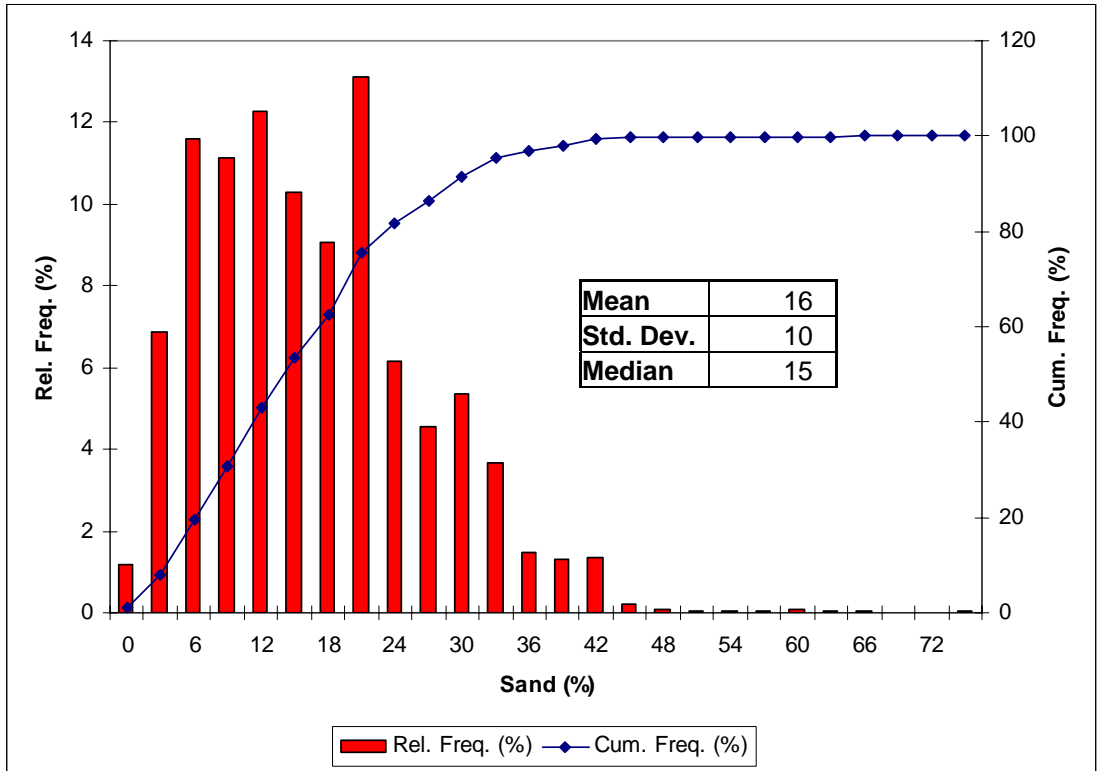


Figure 9. Distribution of percent sand in 610 m below seafloor in Green Canyon.

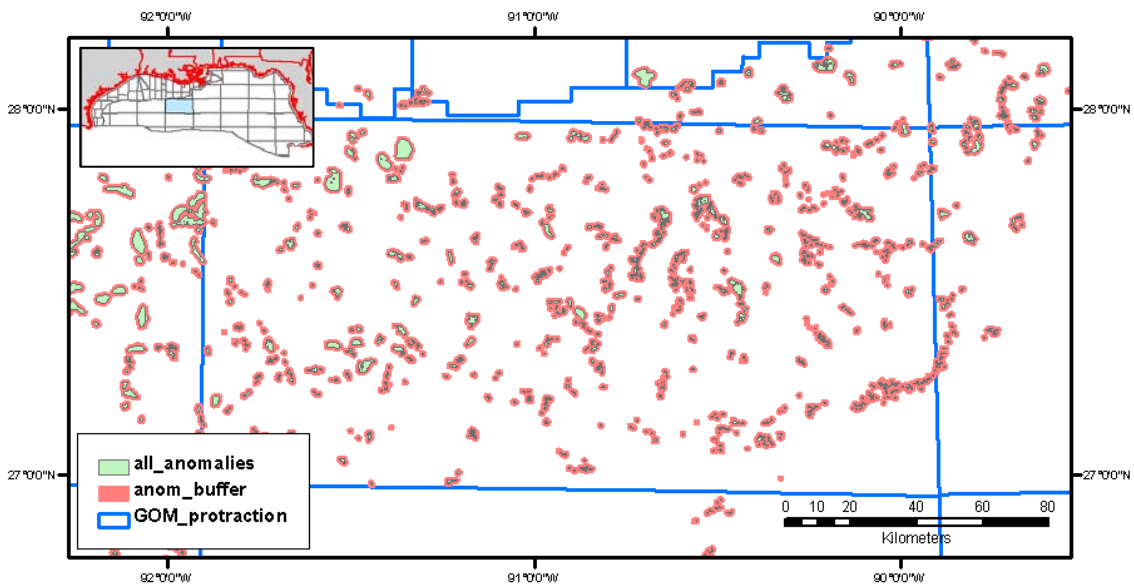


Figure 10. Location of buffered surficial seismic anomalies in Green Canyon. Green polygon is actual areal distribution; pink polygon represents 2,500-ft buffer.



## Charge Module

The charge module is designed to produce a probability distribution of the volume of methane delivered to the hydrate stability zone. In the absence of charge, the existence of a methane hydrate stability zone, in itself, is insufficient for formation of methane hydrates. The charge module consists of two models: a methane generation model and a model of methane migration from the point at which it was generated to the hydrate stability zone (see figure 11).

In the integration module, the volume of gas delivered to the HSZ in a cell is compared to the available pore volume in the HSZ that can be saturated with hydrates. If there is more gas charge volume than pore volume for it to saturate, the available pore volume is completely filled with hydrate; then the volume of methane hydrates is equal to available pore volume. This is the “container-limited” case. If there is less charge volume than available pore volume in the HSZ, the distribution of charge becomes the distribution of in-place hydrate volumes. This is the “charge-limited” case.

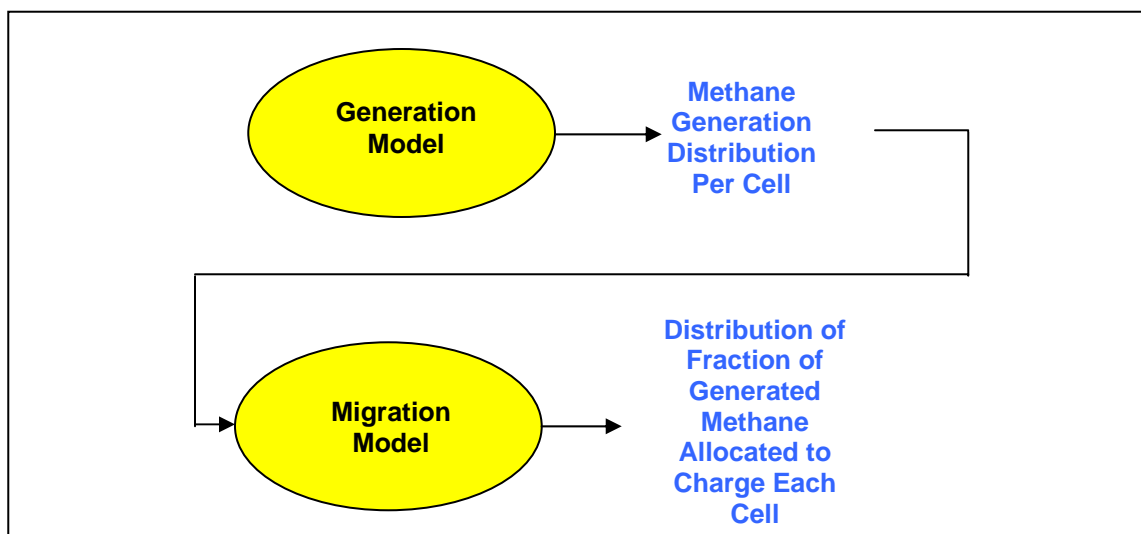


**Figure 11. Structure of the charge module.**

The probability distribution of charge in a cell also plays a role in the determination of the thickness of the undersaturated zone that inhibits hydrate formation in the shallowest part of the section below the seafloor. The relationship between those two variables will be discussed in section IV (container module) of this chapter.

From extensive empirical evidence, it is known that both biogenically and thermogenically generated methane contribute to methane hydrates. This has been observed worldwide and specifically in the GOM (Milkov and Sassen, 2001). Thus, the ideal way to do a mass balance-based assessment of methane hydrates is to include charge generated both biogenically and thermogenically.

In this phase of the project, however, thermogenically generated gas is *not* included in the analysis of charge (*similar to* Collett, 1995). The strongest impediment is lack of usable data for modeling thermogenic gas generation from source rocks in the study area. In the GOM, source-rock investigations have been done with sufficient resolution to type the lithologies and general ages of hydrocarbon sources (*e.g.* Hood et al., 2002). However, many of these analyses do not include source interval cores for the geochemical characterization required to produce quantitative estimates of hydrocarbon production by volume, phase, and time over burial. More importantly, there is a lack of systematic isopachs of proposed sources to complete the volumetric data required for mass balance analysis of thermogenically generated methane.

Failure to consider thermogenic gas in our analysis of charge is an important limitation of this phase of the study. However, the effect on aggregate methane available to charge the HSZ is, in our judgment, relatively small:

- (1) Given the migration model employed to move biogenic gas from where it was generated to where it became available to charge the HSZ, thermogenically generated methane would likely follow the same paths, re-enforcing the biogenic-only geographic distribution of methane hydrates.
- (2) The empirical distribution of biogenic versus thermogenic gas in seafloor sampling programs in the study area (most prominently, those organized through Texas A&M University) may point to a way to make bulk volume corrections for the absence of thermogenic methane in the charge module.
- (3) One ad hoc “fix” to the omission of thermogenically generated gas in the estimate of charge is employed in this study: For all cells in the model that fall within the bounds of a buffered surficial seismic anomaly, the available pore volume in the net HSZ is assumed to be fully saturated – even if there is charge limitation (considering biogenic gas alone). The rationale is that, if there is sufficient methane flux to vent methane to the seafloor surface (in gas and/or solid phases), the available pore volume must be fully saturated, and, if biogenic gas is not available to completely saturate the section, thermogenic gas is available to do so.

## **A. The Generation Model**

### *1. Model Structure*

The general structure of the biogenic methane generation model is mass balance. Simplistically, a mass of organic carbon is input to the model of a production function (see figure 12). This function determines the efficiency of its transformation to biogenic methane and produces an estimate of the output mass of methane. Mass balance models for thermogenic hydrocarbon generation were first introduced in the 1980s. However, we believe that this is the first use of the technique to model biogenic methane production in hydrocarbon resource analysis. While this model pushes data and analytic protocols to their limits, informed guidance of domain experts lends authority to the analysis. Due to our limited knowledge and data, there is less reliance on well-established procedures than is typical in hydrocarbon resource assessment.

Key contributors to generation model development were Dr. Fredrick (Rick) Colwell, Oregon State University, a microbiologist, and Dr. Roger Sassen, Texas A&M University, a geologist and geochemist. The fine structure of the model is strongly influenced by their advice; in addition, they provided empirical data and data references, and assisted in interpretation of those data and results from the model in the course of its development.

The discussion of the charge module begins with a review of basic input data describing total organic carbon (TOC) in the sediments of the study area. A description of how the methanogenic productivity function used in the model is built and the rationale for the choice of functional forms follow. Finally, we describe how the sedimentary column is divided into discrete stratigraphic units, how their thicknesses are determined and how the generation model operates. The model is designed to enhance our ability to use Monte Carlo sampling for inputs and outputs while maintaining ground-truth integrity. In this model, most input variables and model parameters are represented by probability distributions.

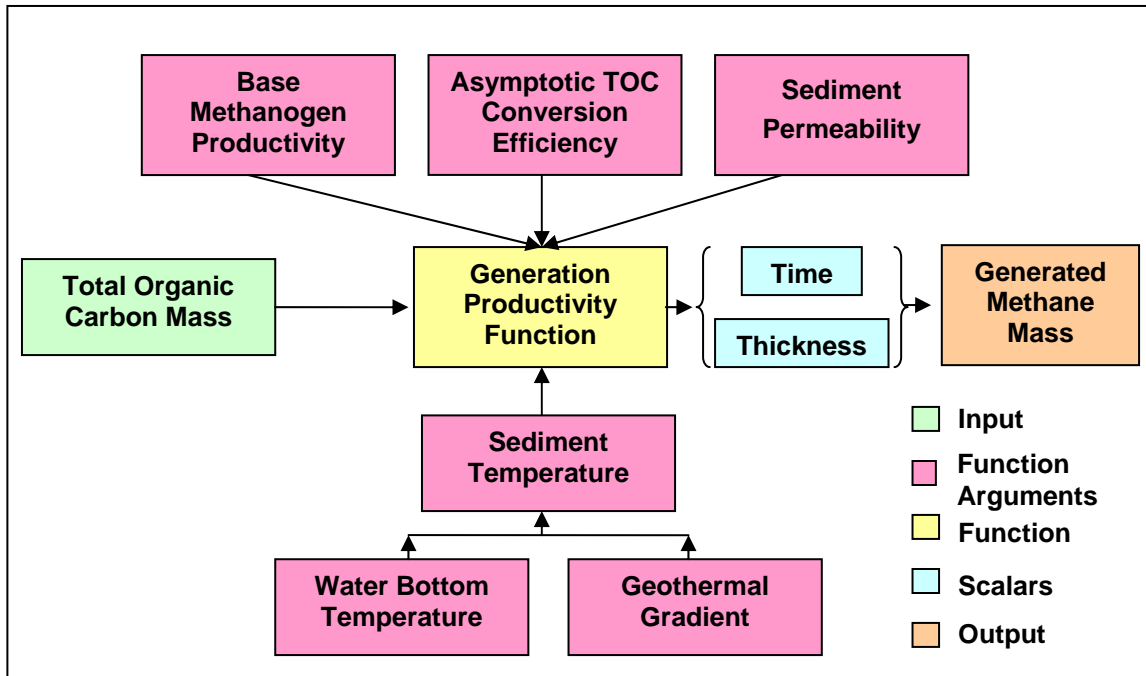


**Figure 12. Schematic diagram of biogenic generation model. Input variables, all function arguments, the unit thickness scalar and the output – methane generated – are treated as uncertain quantities, represented by probability distributions. Geologic time period lengths are deterministic.**

## 2. Quantity of Organic Carbon in Sediments in the Study Area

An empirical data set provided by Dr. Sassen, based on work of the Deep Sea Drilling Project (DSDP) (Bouma et al., 1986), is used to support the computation of the quantity of TOC available in a cell to convert to methane. The TOC input is based on analyses of shallow core data obtained in DSDP Leg 96 at Sites 614A, 615, 616, 617, 618, 619, 620, 621, 622, 623, and 624. As can be seen in figure 13, the sites of collection are neither numerous nor in any sense randomly distributed across the study area. Moreover, at the locations sampled, holes are clustered. We understand, however, that this data set represents all available DSDP data in the GOM study area where both TOC has been collected and hydrolysis performed on it (discussed below).

While not an ideal sample, these data do approximately span the range of water depths relevant to the present study. Moreover, their locations relative to the modern Mississippi River fan are useful. One of the clusters is directly in the course of the fan, one cluster is in shallow water offset downstream along the modern lateral current crossing Mississippi deposition, and the rest of the data are offset in the opposite direction in deeper water. We believe that the ranges observed in this data set approximate the results of what a well-designed program to sample over the same vertical interval would yield.

The DSDP Leg 96 data consists of 773 observations. They are taken from 13 cores that typically cover the first 100 to 200 meters below the seafloor (mbsf); however, the deepest observation is 360 mbsf. The data are expressed as percent dry mass organic carbon as a fraction of total sediment mass. The conversion of the weight percent TOC data to the absolute mass of carbon in the sediments is based on a bulk sediment density of 2.1 grams per cubic centimeter.

A critical assumption made about the quantity of organic carbon input to the generation model is that that the DSDP Leg 96 data adequately characterizes TOC laterally across the entire study area. We also extended this assumption vertically, and used the same probability distributions on TOC (from the Leg 96 data, collected over the modern 100 to 200 mbsf), to characterize the *vertical distribution* of TOC in the *entire* sedimentary section of the study area. That is, the distribution of TOC in GOM sediments is a first-order stationary process, not only in the two lateral dimensions, but also in depth. These are surely refutable assumptions, but necessary, given

that geographic limitations of the extant data and the fact that no vertical profiles of organic matter quantity and quality deeper than those taken by Leg 96 have been made available.

The relative frequency distribution of TOC data is nearly normal, with the exception of several outliers associated specifically with two of the cores. The areal distribution of all data is shown in figure 13.

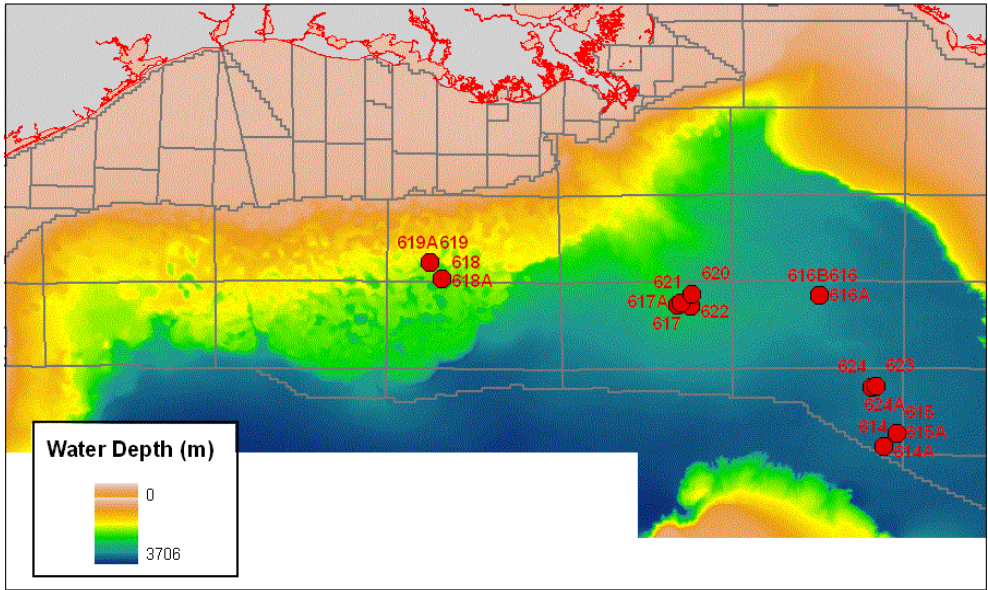


**Figure 13. Location of DSDP Leg 96 holes used for the data on distribution of total organic carbon and organic matter quality.**

After further statistical analysis, and discussion with Dr. Sassen about the organic matter recovered in the coring program, some outlying observations were omitted. An empirical distribution of TOC based on remaining data appears in figure 14. The final choice of functional form for the distribution of TOC used in the study is based on sample data that omit observations from cores 614A and 615 (see figure 15). The mean of the retained TOC data is 0.849 percent and the standard deviation of the distribution is 0.26 percent, both based on 681 observations. Both values are in line with expectations.

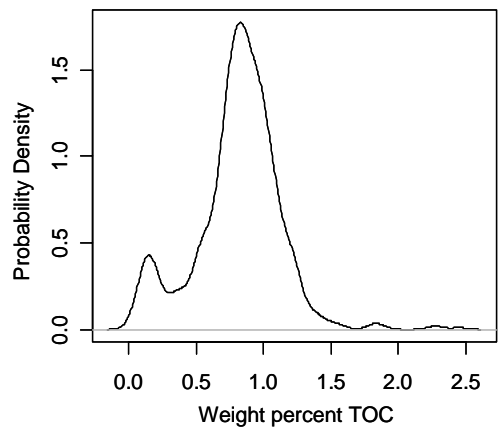


**Figure 14. Probability distribution of 773 observations on total organic carbon from the Leg 96 cores.**

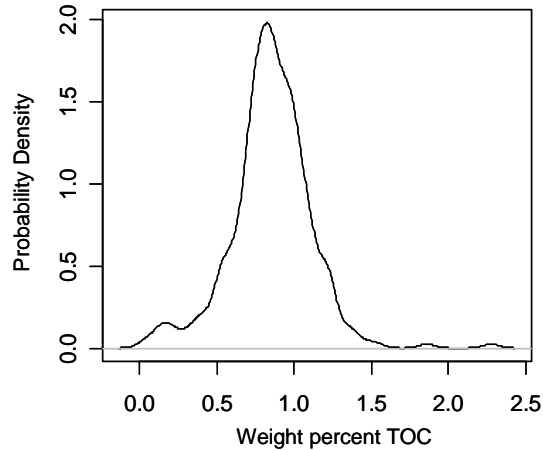


**Figure 15. Distribution of 681 observations on total organic carbon from the Leg 96 cores, omitting 91 outlier observations (12% of the total population) from cores 614A and 615.**

A continuous probability density function is fit to the raw, empirical distribution of data in figure 15 and used in model calculations. A Weibull distribution fits the data quite well. The data and a Weibull distribution fit, based on the 681 retained observations on TOC, appear in figure 16. The parameters of this Weibull distribution fit to TOC data are: Location = 0; Scale = 0.94; Shape = 3.35

At each Monte Carlo trial, independent draws from this Weibull distribution are made—one for each cell. The trial value of (decimal percent) TOC in sediments is multiplied by bulk sediment density to produce an input value for the mass of organic carbon entering the productivity function.

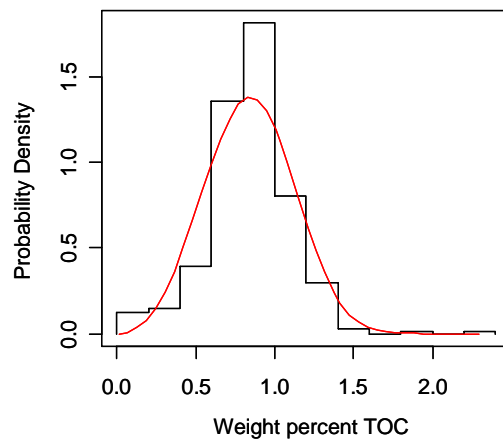


**Figure 16. Distribution of 681 observations on total organic carbon from the Leg 96 cores (black) against the fitted Weibull distribution (red).**

### 3. Construction of Methanogenic Productivity Function

Once a mass of organic carbon is in hand, the generation model translates it into methane: the input mass is multiplied by a function representing the efficiency with which organic carbon is converted by methanogenic archaea to methane. Productivity is defined as a *rate*, measured in grams of methane produced per gram of organic carbon input to the system per unit of time (here per one million years).

This process is complex. The model represents the metabolic reactions of communities of methanogenic archaea to changes in their environments as sediments are deposited on the seafloor and progressively buried. Our description of how this rate is modeled is divided into two parts.

The first part represents our understanding of how the productivity of a *single species* of methanogen, living at the seafloor, responds to changes in ambient temperature. This relationship is then generalized because the methanogenic community we seek to model is, in fact, composed of *multiple species*. Mathematical representation of the collective effects of multiple species on the metabolism of organic matter is, unfortunately, far more complex than simply summing the contributions of each species.

Biogenic methane arises not just from methanogens at the seafloor, but from the entire methanogenic community of the entire sedimentary section. In practical terms, for the GOM, this involves rock extending from the seafloor to depths of 2,000 to 4,000 mbsf. A consequence is that relationships which drive methanogenic productivity in a seafloor environment must accommodate very different environments at depths of up to 2-4 km below the seafloor.

#### a. Modeling Methane Productivity

The productivity, or rate at which methanogenic archaea convert organic carbon to methane in a given environment, is assumed to be a function of ambient temperature in that environment. An example of the particular function we use to represent the rate of methane produced by a collection of species in a given environment is shown in figure 17:

- (1) The intercept is productivity at the minimum value of the temperature domain (marked A). The value assumed by the intercept is a critical value because it *scales productivity at all temperatures*. In our model, the intercept captures the collective influence on the dependent variable (methane production rate) of all explanatory variables *other than temperature*.
- (2) As temperature increases above its minimum, methane productivity increases monotonically over a finite temperature interval (marked B). This is the domain of Arrhenius' Law, an exponential growth law which declares that the rate of a chemical reaction doubles for every 10°C increase in temperature.
- (3) Additional heat ultimately slows the rate of productivity. It peaks at a finite temperature (marked C). In the example shown in figure 17, the shape of the rate function in a neighborhood of peak productivity is dictated by interactions among multiple species of methanogens, each contributing to the total mass of methane produced.
- (4) As temperature continues to increase above peak productivity temperature, the rate of productivity rapidly declines (marked D).
- (5) Finally, as with any biologic organism, there is a temperature limit beyond which organisms can no longer survive; biologic metabolism of organic carbon ceases—and so does biogenic methanogenesis (marked E).

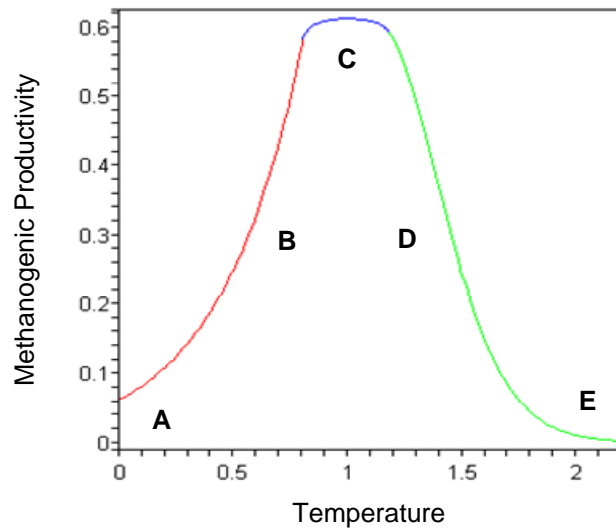


**Figure 17. General relationship between methanogenic productivity and temperature. Letters denote domains discussed in the text.**

Our model of methanogenesis begins with analysis of productivity of a single species under seafloor conditions. It is then extended to incorporate productivity by methanogenic communities in buried sediments. Modeling of productivity proceeds in three steps:

- (1) Construct a rate function of temperature assuming that all methane is produced by a single species of archaea. This captures the basic dynamics of the process.
- (2) Recognize that methanogenesis in marine sediments is most likely the collective contribution of a community of many species methanogenic archaea. Modify the single-species function to reflect this.
- (3) Extend the model of productivity under seafloor conditions to include subsurface conditions. This is handled by modeling the intercept (“A” in figure 17) to be a function of a ratio sediment permeability at the seafloor and sediment permeability at subsurface depths. As stated earlier, the intercept is a fundamental parameter—it directly scales the temperature/productivity function shown in figure 17 above.

b. Model of Methanogenic Productivity of a Single Species of Methanogenic Archaea

Our model of the rate at which organic carbon is transformed into methane by a single species of methanogenic archaea incorporates the qualitative features of productivity described above. The starting point is to model productivity over the lowest temperature domain to which methanogens would be exposed: temperature at the seafloor. The derivation of the production function for a single species is a fairly complex process, and is described in detail in Appendix B.

c. Collective Impact of a Community of Different Methanogenic Species on Productivity

Biogenically sourced marine methane hydrates are likely created by several distinct microbial species operating in concert. A consequence is that a plot of in situ measurements of methane generation rates versus temperature is likely to be multi-modal. If a large enough number of distinct microbial species are present, this plot could appear to be relatively “flat” in an interval about a peak rate temperature (Price and Sowers, 2004).

Isolates in pure cultures are usually not representative of community behavior: they have normal shaped curves with lowest, optimal, and highest temperature that depend on taxa, and they are not challenged by the factors that would be present in the natural environment.

One way to represent this characteristic is to treat generation as a (probability) mixture of more sharply peaked production rate functions, one for each single microbial type's production rate; mixture rates correspond to relative proportions of microbial types in the sample data. Another is to model the rate of methane production as a function of temperature to exhibit mesa-like behavior in a temperature interval containing a peak production rate (35 °C to 45 °C for example) followed by a decline of this rate as temperature continues to increase.

The second approach, imposition of a mesa-like peak region, to capture the collective impact of a mixture of many species of methanogens is adopted for this study (Deming and Huston, 2000). Under reasonable assumptions about how methanogenic species are mixed, as the number species in an ecosystem increases, the peak of the production rate function produced by mixing may “smooth out” and vary slowly in the neighborhood of a single absolute maximum rate. If so, it is reasonable to model the rate function as mesa-like in a neighborhood of an absolute maximum rate in place of mixing individual rate functions.

To accommodate a relatively “flat” peak in the neighborhood of the temperatures associated with maximum productivity, we modified the form of the function described for the productivity of a single methanogenic species as a function of temperature. Figure 18 is an extreme example of a mesa-like function that allows a smooth transition to it from a strict form of Arrhenius' Law.

The function generating the graph shown in figure B.2 (in Appendix B),  $x^\beta(1-x)^\beta$ , is flexible enough to capture the collective impact of many species on methane production--each with a different maximum productivity over the temperature domain assumed to encompass these maxima (35 °C – 45 °C).<sup>1</sup>

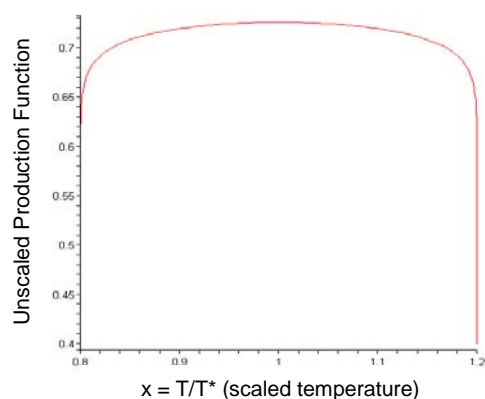


**Figure 18. A mesa-like function in an interval about a maximum value. The x-axis is the variable x (defined in the text); the y-axis is unscaled rate of methanogenic production.**

The mathematics of smooth pasting a mesa-like function like that in figure 18 to an exponential form of Arrhenius' Law for temperatures below about 35°C (below about 0.875 in the scale of the graph) appears in Appendix C. The magnitude of variation in the production rate as x traverses the domain of this function (here 35 °C – 45 °C) is controlled by the parameter  $\beta$ .

Figure 19 shows the result of smooth pasting a mesa-like function, as in figure 18, to Eq. B3 - Arrhenius' Law at  $x=x_0$  (at temperature  $T=27.5$  °C). At  $x=x_1$ , ( $T=$  °C) a rapidly decreasing function is smoothly pasted to the mesa-like function. It declines to a negligible value at a temperature (70 °C) beyond which methanogenesis ceases.

<sup>1</sup> This mesa-like function need not be symmetric: use  $x^\eta(1-x)^\beta$ ,  $\eta \neq \beta$ .



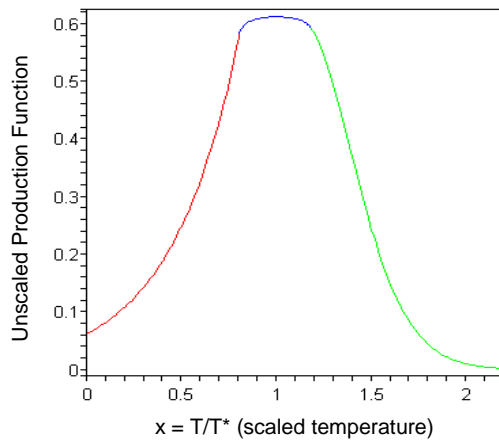


**Figure 19. Smooth pasting of three functions to capture qualitative features of productivity of a community of methanogen species. The red portion of the function follows Arrhenius’ Law. The blue section is the mesa-like function with  $\beta= 0/10$  designed to incorporate mixing of peaks of individual species’ productivity functions. The green section is post-maximum exponential decline in productivity.**

#### d. Methanogenic Productivity at the Seafloor

In order to complete specification of the productivity function, the rate function displayed in figure 19 must be multiplied by a term representing productivity at the seafloor. There are no rich data sets from which the empirical distribution of methane productivity at seafloor conditions can be easily extracted. Dr. Colwell suggested that we base our calculations on data appearing in a study by Price and Sowers (2004).<sup>2</sup> These authors repackage data from a large number of studies of metabolic rates as functions of temperature into a graphical summary (see figure 20). The data in Price & Sowers’ figure 1 comes from many, sharply different ecosystems such as permafrost, polar ocean and ice, permanently covered Arctic lakes, salt marsh tidal creeks, and marine sediments.<sup>3</sup>

We use Price and Sowers graphical summary “Base Methanogen Productivity” in figure 20 to infer seafloor productivity. Their description of the seafloor environment in each of the studies that they review naturally includes temperature. We know that seafloor methanogenic productivity varies widely – even at common temperatures—and their study confirms this fact.

Both the impact of seafloor temperature and the collective effects of variables other than temperature on productivity are represented in the value of the intercept in figure 20. This is the same term,  $A_{SF}(T_{SF}(WD))$ , that appears in Eq. B.2. It scales the marginal rate of methane production at all temperatures at and above seafloor temperature.

Ideally, inferences about seafloor productivity should be based on re-analysis of the raw data used by Price and Sowers to produce figure 20 below<sup>4</sup>. A meta analysis or perhaps, empirical Bayes analysis designed to characterize uncertainty about seafloor temperature metabolic rates could then be done. Unfortunately, the data is *not* published in a form immediately useful for statistical calculations. We can only impute sample statistics from their figure 1.

According to Dr. Colwell, of the three general categories of data identified by Price and Sowers in figure 20, only “Maintenance Data” should be used for inferring an initial production rate for our analysis. All of this

<sup>2</sup> Price, P.B. and Sowers, T., *op. cit.*, p. 4532.

<sup>3</sup> Price and Sowers, *op. cit.*, page 4632

<sup>4</sup> *Ibid.* Figure 1 on page 4634.

particular class of data is for temperatures below 35 °C. Consequently, we model rates in this particular dataset as if they behave according to Arrhenius' Law as in Eq. B.2.

Recovery of estimates of methane production rates from studies used by Price and Sowers to construct figure 20 depend, of course, on the choice of a statistical model that describes how the data were generated. The process of recovering the Price and Sowers data for use in this study is reviewed in Appendix D.

The productivity  $A_{SF}(T_{SF}(WD))$  of a community of methanogens under seafloor conditions, with seafloor temperature ( $T_{SF}(WD)$ ) taken to be 2 °C, is modeled in Price and Sowers units as an uncertain quantity possessing a lognormal distribution. Appendix D describes how Price and Sowers (see figure 20) is used to infer its parameters. This probability distribution of methane productivity under seafloor conditions is one of the main drivers of the generation model.

The natural log of seafloor productivity  $\ln A_{SF}(T_{SF}(WD))/1,000,000$  is normally distributed with mean value - 4.331 and standard deviation 3.25. This implies that the mean of  $A_{SF}(T_{SF}(WD))$  is  $2.628761 \times 10^6$  and that it possesses standard deviation =  $525.3226 \times 10^6$ , both in units of gram of methane/cubic meter of sediment/ million years. The ratio of the standard deviation to the mean is approximately 200, implying that the distribution of  $A_{SF}(T_{SF}(WD))$  is very positively skewed (see figure 21). Values of  $A_{SF}(T_{SF}(WD))$  are converted from Price and Sowers units to grams of methane produced per gram of organic carbon per millions of years by the method described in Appendix E.

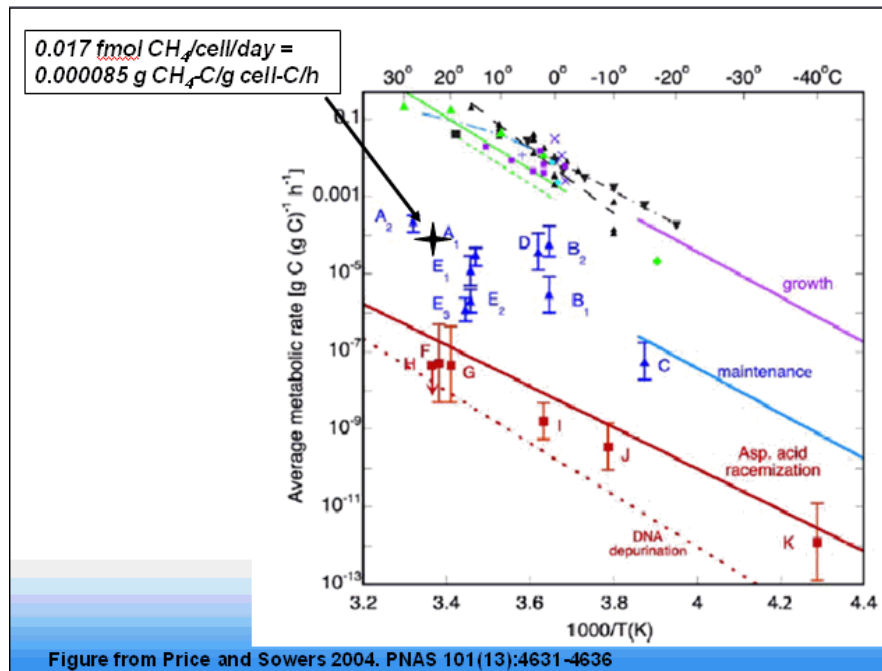


**Figure 20.** Data from Price and Sowers (2004) used to interpolate productivity of methanogens at seafloor temperature. Figure copyright © 1993-2005 by The National Academy of Sciences of America, all rights reserved.

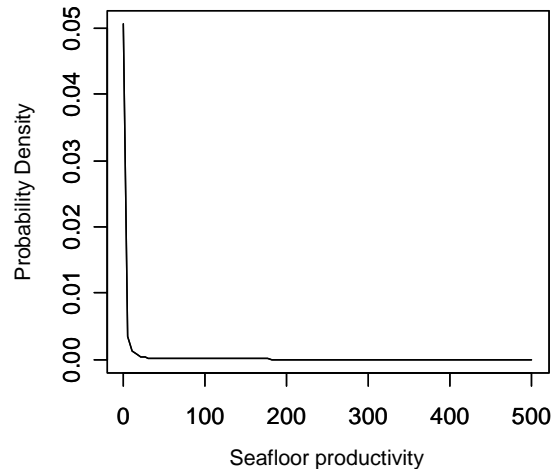


**Figure 21. Distribution of  $A_{SF}(T_{SF}(WD))$  based on analysis of Price and Sowers data.**

#### e. Methanogenic Productivity in Buried Sediments

If methanogenic productivity is solely a function of temperature, determination of its value as a function of temperature in buried sediments is simple: calculate the ambient temperature at the burial depth of interest and read productivity from figure 19, scaled by the intercept of  $A_{SF}(T_{SF}(WD))$ . However, in discussions with Dr. Colwell, we concluded that while temperature shapes the marginal rate of production of methane, the scale of the function is influenced by other variables – most prominently, water flux through the sedimentary environment. At seafloor conditions, water flux through the sediments in which methanogenic archaea live is at its maximum. Sediment compaction on burial diminishes permeability, ensuring that water flux declines as a function of sediment burial depth as well.

The relationship between water flux and methanogenic productivity is direct; as water flux increases, so does productivity and *vice versa*. As we have no observations on water flux through sediments as a function of depth, we adopt permeability as an instrumental variable for it. Water flux, and thereby permeability, plays at least two key roles in methanogenic productivity:

- (1) When permeability/water flux is high, it provides local sources of electron donors and electron acceptors to the microbes in the sediments (D'Hondt et al., 2004; Parkes et al., 2005). For methanogens this would result in higher methanogenic rates. When the permeability/water flux is low, the rate of supply is diminished, and the metabolism becomes input constrained (i.e., archaea starve after consuming the available electron donors and electron acceptors).
- (2) When permeability/water flux is high, accumulated methane, a metabolic waste product of methanogens, is removed from pores. When permeability is low, methane accumulates in the pores. In principle, this accumulation of methane in the pore space is likely to pose a thermodynamic limitation to methanogens making it difficult to produce methane in an environment that is already rich in this gas. There is, as yet, no experimental evidence that this occurs in marine sediments where methane is produced; however, control of product concentrations in other microbial metabolic reactions is essential if cells are to survive at the threshold of what is thermodynamically possible (Jackson and McNerney, 2002).

Dr. Colwell notes that there is research which correlates relative local highs in microbial activity with locations that are sand-shale contacts (Fredrickson et al., 1997), lending support to the use of a function of permeability/water flux as a scaling function for productivity at the seafloor in the generation model. Activity at the boundary between a richer source of organic carbon and a more porous lithology (i.e., a shale/sand contact) relies as much on access to the pores as it does on the general quantity of nutrients available to the reaction.

This relation between permeability and productivity is re-enforced by weighting bulk rock permeability by the sand/shale ratio (see below). As both lithologies are more typically bedded than homogeneously mixed, the higher the sand content, the greater the opportunities for sand/shale contacts to exist in a given section; therefore, the higher the potential for biologic methanogenesis. Because of its dependence on lithology, use of permeability as an instrumental variable also incorporates the positive impact on productivity that arises as the number of sand/shale contacts in the section increases.

A fundamental assumption made in modeling the methanogenic productivity of *buried* sediments is that the intercept of the productivity function (figure 19) *for a given depth of burial is a function of methanogenic productivity at the seafloor ( $A_{SF}(T_{SF}(WD))$ ), scaled by the ratio of sediment permeability at the given depth divided by sediment permeability at the seafloor*. The rate function for productivity at the seafloor, represented in figure 19, remains the same at any depth; it simply “slides” down the y-axis proportionate to the ratio of stratum permeability to the permeability of the seafloor datum.

#### f. Determining Sediment Permeability at Depth

It is well known that sediment permeability decreases with depth. It is also well known that this relationship varies systematically with sediment lithology. In the GOM case, sediments are classified either as “sand” or “shale”. As a function of burial depth, sand loses permeability much more slowly than shale.

In order to find the permeability scaling parameter for the intercept of the productivity function, sand permeability as a function of depth and shale permeability as a separate function of depth are modeled. To fix geologically sensible aggregates of the sedimentary column in each cell, the entire thickness between the seafloor and top of basement (salt) determined by Shedd and Hunt is divided into five stratigraphic units: Lower Miocene, Middle Miocene, Upper Miocene, Pliocene, and Pleistocene.

The practical task, for each of the 202,079 cells in the study, is to determine probability distributions for permeabilities of sediments as a function of burial depth, by stratigraphic unit. For instance, we compute permeabilities of Lower Miocene age during the original deposition in Lower Miocene time; then, re-estimate Lower Miocene permeability again when it was buried under Middle Miocene sedimentation; repeating to capture the effects of burial by Upper Miocene, Pliocene and finally Pleistocene sedimentary units.

We estimate permeability for a given unit at a given depth as follows:

- (1) Assume the sand/shale ratio in the top 2000 feet below seafloor, as mapped by Shedd and Hunt, applies to the entire stratigraphic column in the section (Lower Miocene to Pleistocene).
- (2) Estimate end-member sand permeability vs. depth and shale permeability vs. depth.
- (3) Use the Shedd-Hunt sand/shale ratio for that cell as weights to combine (or mix) “pure sand” permeability and “pure shale” permeability for a given depth,

While there is abundant data on the permeability of commercial sand reservoirs in the GOM, observations are very sparse in the shallowest part of the section (because there are few to no existing commercial hydrocarbon reservoirs there). Because shale is not a reservoir rock, there is *no data* on shale permeability reported to the MMS by operators of GOM oil and gas reservoirs, and there is sparse literature on how shale permeability varies with depth.

Because of the availability of an extensive database on sand permeabilities from MMS, that data is used to construct the sand permeability-depth submodel. Although commercial oil and gas reservoirs in the GOM are not lithologically “pure” siliciclastic sand, this is the best available source for a locally relevant statistical model. In order to give “sand” the widest possible definition, all 9,461 available observations from MMS data on reservoir permeability and depth data are used to produce figure 22.

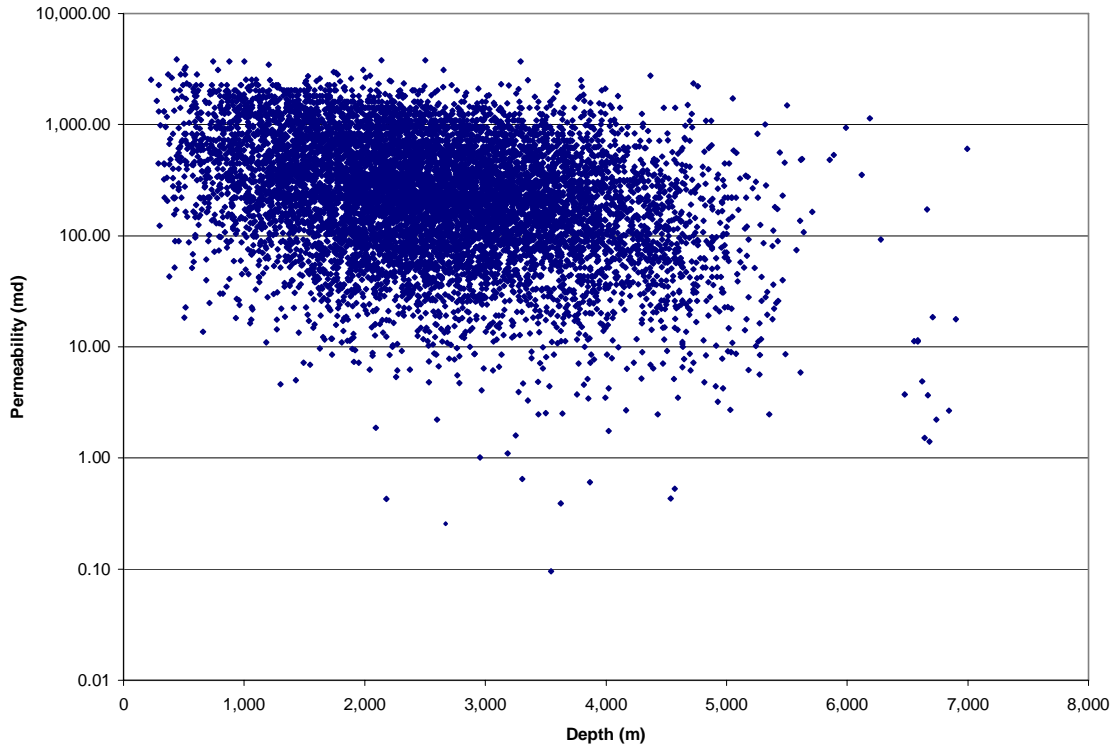


**Figure 22. Scatter plot of permeability vs. depth for 9,462 observations from GOM commercial oil and gas reservoirs.**

To fit a model to the sand permeability data:

- (1) Apply a Box-Cox transformation  $Z(\lambda) = \frac{Y^\lambda - 1}{\lambda}$  to render the transformed data symmetric, where  $Y$  is permeability in millidarcies and  $\lambda$  is a parameter to be estimated.
- (2) Fit a regression model  $f(Z(\lambda) | d) = \alpha + \beta d + \text{error}$  to the data, with  $d$  = depth in meters, and  $\alpha$  and  $\beta$  are regression parameters.
- (3) The fit is  $\hat{f}(Z(\hat{\lambda}) | d) = 10.85 - 0.000258(d)$ , with  $\hat{\lambda} = 0.1530$ .
- (4) To obtain an estimate of permeability as a function of depth, back transform to  $\hat{Y} = (\hat{\lambda} \times \hat{f}(Z(\hat{\lambda}) | d) + 1)^{1/\hat{\lambda}}$

The residual standard error is estimated to be 2.541 on 9,367 degrees of freedom. Adjusted  $R^2$  is 10 percent; while this is small, the parameter estimates possess tight confidence intervals. Figure 23 is a graph of the model fit of permeability (at the maximum likelihood estimators of parameters) as a function of depth:

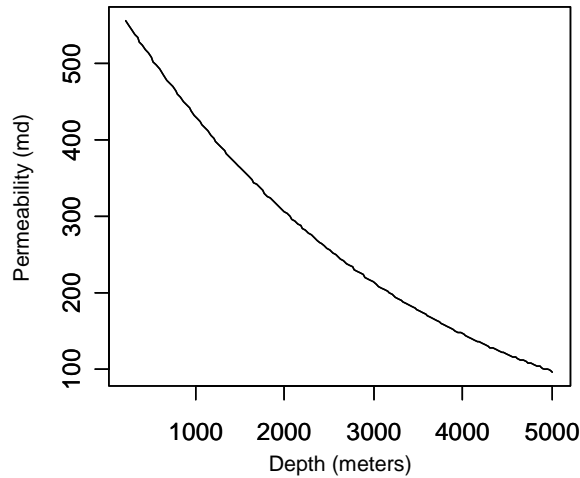


**Figure 23. Fit of sand permeability (measured in millidarcies) as a function of depth.**

The model adopted for permeability of sand sediments at depth  $d$  is

$$(1.1) \quad \hat{Y}(d) = (\hat{\lambda} \times \hat{f}(Z(\hat{\lambda}) | d) + 1)^{1/\hat{\lambda}} = (0.153 \times [10.85 - 0.000258 \times d] + \text{error} + 1)^{1/0.153}$$

Probabilistic properties of parameter estimates and the error term must be specified in order to use Eq. (1.1) as a data generating process model for sampling values of permeability as a function of depth. We assumed that the intercept  $\alpha$ , and slope  $\beta$  are uncertain quantities with means equal to their respective maximum likelihood estimates (MLEs) and standard deviations equal to standard errors of their respective MLEs. In addition, we assumed that the error term has mean 0 and standard deviation equal to the residual's standard error of estimate.

No corresponding shale permeability database exists so we modeled permeability as Spinneli et al. (2004) did in their study of permeability and porosity in fine-grained sediments. Their Table 6.2 presents a model for permeability of fine-grained sediments as functions of depth by a pair of equations: permeability as a function of porosity, and porosity as a function of depth.

Of the five families of sediment types appearing in their table, we judge “fine grained turbidities” to be closest to the “pure shale” end member posited for the GOM. Because of the difficulty of their functional forms, we have imposed a limitation that shale porosity at the seafloor may not exceed 70 percent (expressed here as 0.70). This transforms their shale porosity vs. depth model to the minimum of 0.70 and a normal random variable  $\Omega$  multiplied by a power  $\tau$  of the depth of the sediments in meters (M).

$$(1.2) \quad \phi = \min\{\Omega \times M^\tau, 0.7\}$$

where,

$$\Omega \sim N(0.84, 0.08^2)$$

$$\tau \sim N(-0.125, 0.01^2)$$

Figure 24 is the graph of Eq. (1.2) assuming that the error term is zero.

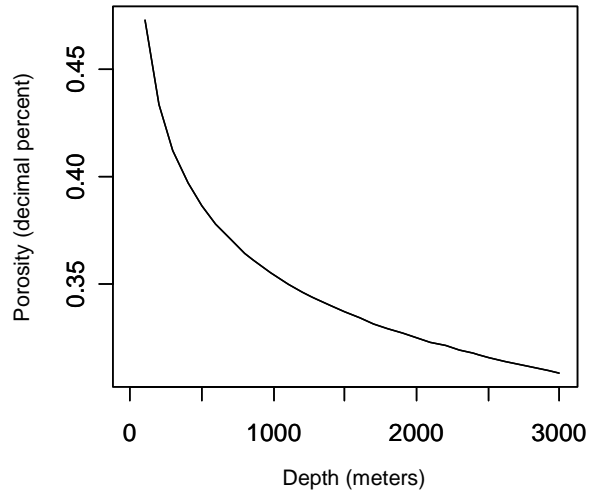


**Figure 24. Shale porosity versus depth at mean values of parameters, based on Spinelli et al. (2004).**

Spinelli et al. (2004) model shale permeability,  $k$ , as a random function of porosity,  $\phi$ , expressed as  $\phi/(1-\phi)$  (figure 25):<sup>5</sup>

$$(1.3) \quad \ln(k) = \ln v + [\omega \times \phi / (1 - \phi)]$$

or

$$(1.4) \quad k = v \times \exp\left\{\frac{\omega \times \phi}{1 - \phi}\right\}$$

Spinelli et al. (2004) did not provide the form of the distribution or an estimate of variance for the parameters, in Eqs. 1.3 and 1.4. As an approximation, each distribution is assumed to be normally distributed with the standard deviation equal to 10 percent of the mean. That is, the parameters  $v$  and  $\omega$  are defined to be uncertain quantities,  $v \sim N(0.0037, 0.000372)$  and  $\omega \sim N(1.7, 0.172)$ .<sup>6</sup>

<sup>5</sup> In Spinelli's original work permeability is in square meters and porosity is in decimal percent. Permeability is rescaled to here to millidarcies (md).

<sup>6</sup> The variance of  $v$  is small enough so that, fortunately, the probability that  $v < 0$  is negligibly small.

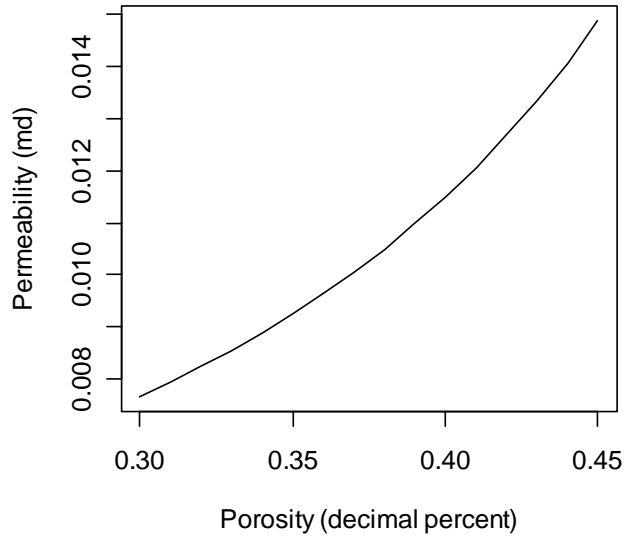


**Figure 25. Estimated shale permeability versus estimated porosity.**

Finally, we have permeability as a function of depth:

$$(1.5) \quad \ln(k) = \ln v + \omega \times \frac{\Omega M^f}{1 - \Omega M^f}$$

or as in figure 26:

$$(1.6) \quad k = v e^{\omega(\Omega M^f / (1 - \Omega M^f))}$$

For each cell, at any given depth, Eqs. (1.1) and (1.6) are used to calculate the end-member sand and shale permeabilities, respectively. The sand/shale ratio from Shedd and Hunt is used to weight these two estimates to create an estimate for sediment permeability at that depth:

$$(1.7) \quad Perm(d) = (SandPerm(d) \times Sand\ fraction) + (ShalePerm(d) \times (1 - Sand\ fraction))$$

In order to compute the scaling ratio for the intercept of figure 19, we need both permeability at depth and permeability of the lithologically identical sediments at the seafloor. For sand, Eq. (1.1) implies a seafloor permeability of 593 millidarcies. For shales, unfortunately, the functional forms used by Spinelli et al. (2004) prohibit evaluation of the functions at zero depth. The permeability of shale at the seafloor is taken to be 1,000 millidarcies, an average of values found using Spinelli et al. (2004) permeability vs. depth function for several fine-grain facies.



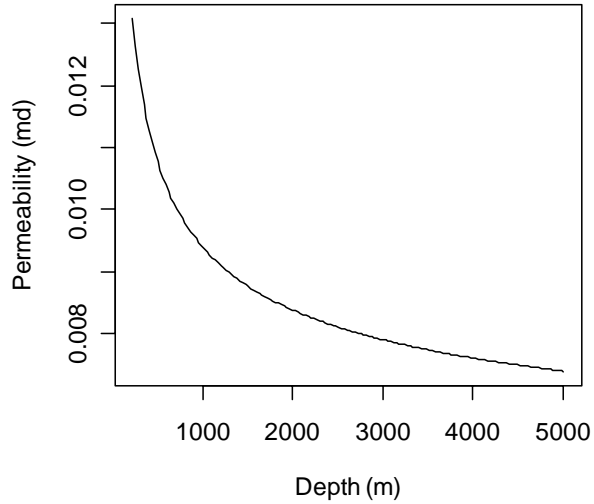


**Figure 26. Shale permeability variation with depth at parameter means.**

Once the ratio of sediment permeability at the seafloor and at depth is in hand, the intercept of the function in figure 19, evaluated at any burial depth,  $d$ , is:

$$(1.8) \quad \left( \frac{Perm(d)}{Perm_{SF}} \right) (A_{SF}(T_{SF}(WD)))$$

#### g. Determination of the Temperature of Buried Sediments

In the generation model, sediment temperature drives the rate of production of methane. Sediment temperature at any given depth below the seafloor is the sum of the temperature at the seafloor plus the depth times the geothermal gradient. How seafloor temperature as a function of depth is determined and the geothermal gradient calculated are described in the container module section of this report.

The probabilistic model adopted for sediment temperature as a function of depth provides a value of temperature in each cell at each Monte Carlo trial.

#### h. Asymptotic Organic Carbon Conversion Efficiency

To complete development of the productivity function shown in figure 19, we must take into account the asymptotic conversion efficiency of organic carbon to hydrocarbons. All organic carbon is not created equally. The chemical characteristics of the carbon molecules that constitute it determine the limit to which it can be converted into hydrocarbons (for any arbitrarily high temperature). This limit is used in analysis of thermogenic transformation of organic carbon to hydrocarbons. We propose that the same limit applies to biogenic transformation.

The susceptibility of organic carbon to transform into hydrocarbons is quantified by a procedure known as hydrous pyrolysis (also known by the commercial name of the apparatus used, RockEval), from which the limiting (asymptotic) value of organic carbon to hydrocarbon transformation is calculated.

In RockEval analysis, a sample of (organically rich) sediment is subjected to several stages of heating over time. In the stage of heating the sample from room temperature to 300 °C, the mass of hydrocarbons produced is called S1. The mass of hydrocarbons produced from the sample from 300 °C to 600 °C is called S2. Because S1 and S2 are measured in units of mass of hydrocarbons generated per mass of sediments, observed values of S1 and S2 are typically normalized by dividing their values by the percent total organic matter (TOC) of the sample being analyzed.

In this study the organic carbon available for biogenic transformation to hydrocarbons begins at very low temperatures (by comparison with thermogenic transformation), so we took the sum of S1 plus S2 as the asymptotic limit of transformation of organic carbon to hydrocarbons (in milligrams of hydrocarbons per gram of organic carbon, mg/g).<sup>7</sup>

$$(1.9) \quad \text{Asymptotic Limit of Organic Carbon Transformation} = ((S1 + S2) \times 100)/TOC$$

The dataset used to estimate a probability distribution for the asymptotic limit of carbon transformation is the same dataset used for analysis of study area sediment TOC, DSDP Leg 96 samples. S1 + S2 data were paired with the TOC data from the same samples.

The raw data of the 681 observations of  $((S1+S2) \times 100)/TOC$  retained in the TOC analysis from DSDP Leg 96 are presented in figure 27. The mean of the  $((S1+S2) \times 100)/TOC$  is 116.18 mg/g. The standard deviation of the distribution is 50.03. The mean is lower than expected for typical Type III organic matter distribution.

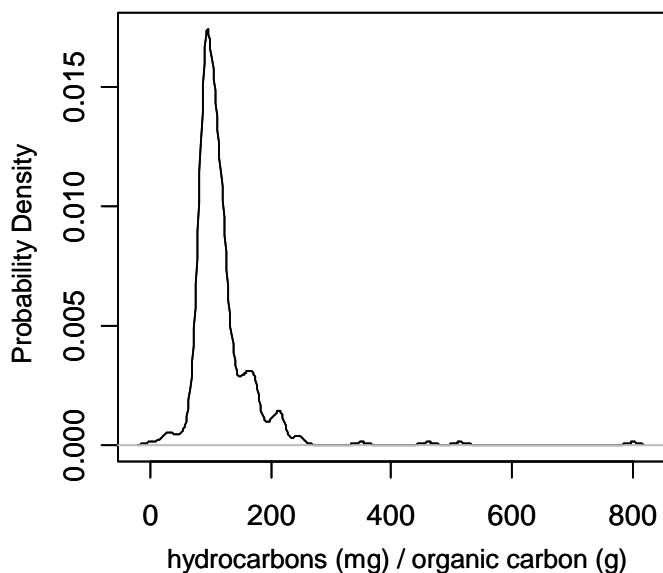


**Figure 27. Empirical distribution of values of  $((S1 + S2) \times 100)/TOC$ .**

As with the case of TOC, a Weibull distribution is fit to data on  $((S1+S2) \times 100)/TOC$ , which is shown in figure 28. For computational ease, asymptotic conversion efficiency is rescaled from mg/g to decimal percent. Parameters of the rescaled Weibull distribution are:

Location = 0; Scale = 130; Shape = 3.5

<sup>7</sup> This contrasts with the practice of using S2 alone when estimating the thermogenic generative potential of a source unit.

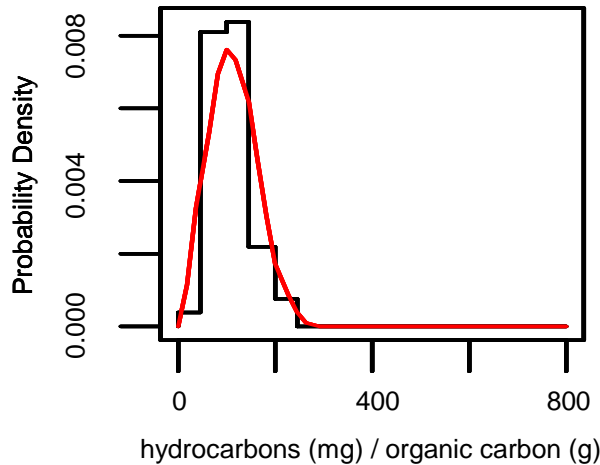


**Figure 28. Distribution of  $((S1 + S2) \times 100)/TOC$  in milligrams of hydrocarbons per gram of organic carbon (x-axis); the y-axis is probability density.**

Calculation of the mass of methane produced, given a mass of organic carbon input, is done by looping through each of five stratigraphic units that cover the sedimentary column of each cell. Starting with the original deposition of organic carbon in any one of those units, the productivity function is integrated over a temperature interval corresponding to top and bottom depths of the unit to determine the amount converted to methane at a period in geologic time. At each time period, the cumulative amount of organic carbon converted to methane is calculated. The mass of organic carbon already converted is subtracted from the mass available for conversion in the next geologic time step. However, if the cumulative amount converted at any time step exceeds the estimated asymptotic conversion efficiency, production of methane ends, and no more is generated in the model for the remaining periods of geologic time.

#### 4. Modeling Generation

The sections above explain the structure of the generation model and its inputs. It is critical to keep in mind that the output of the productivity function in figure 19 is production per unit of time and per unit of organic carbon supplied to methanogenic archaea in the sediments of each cell.

To derive the mass of methane produced in a sedimentary unit in a geologic time period, the rate of methane production function in figure 19 is integrated to derive a cumulative function. This, in turn, is evaluated at top and bottom temperatures of that unit. The difference equals the unscaled mass of methane produced. To get that unit's methane production during a geologic time step, the value of this integral is multiplied by the duration of the time step analyzed (in millions of years) and by the volume of rock in the cell contributing to biogenic methane production.

Repeating this calculation for each sedimentary unit at each geologic time step allows calculation of the total volume of methane generated in a cell over its entire sedimentary extent and all geologic time.

Sedimentary volume is computed as follows: The area of each cell is constant at 2.32 km<sup>2</sup>. The total thickness from the seafloor to the top of basement (salt), estimated by Shedd and Hunt, is divided into stratigraphic units so that the volume of rock and mass of carbon involved in methane production in each cell can be correlated with geologic time. The duration of each of the five geologic time periods is taken from a standard source (Berggren et al., 1995). Together, this allows calculation of numerical values of variables necessary to complete the computation of the methane production in a sedimentary unit over geologic time and a Monte Carlo empirical distribution of biogenic methane production for each cell in the study area.

### a. Partitioning of Stratigraphic Column

The thickness of the stratigraphic column in each cell in the study area is defined to be the total vertical depth to the top of basement (salt) minus the seafloor depth. These thicknesses varied over the GOM from zero (where salt outcrops on the seafloor) to over 8,000 m. From the viewpoint of the generation model, if the entire thickness of sediments in a cell had been deposited instantaneously, the calculation of several depth-dependent parameters would be fairly straightforward. The average temperature, porosity, and permeability of the sedimentary section would be calculated at a single midpoint depth.

However, sedimentation was not instantaneous. Instead, five geologic units are recognized: the Lower Miocene, Middle Miocene, Upper Miocene, Pliocene and Pleistocene. In some cases, particularly in the southern part of the study area, it also would have been prudent to include units older than Lower Miocene. Originally, the plan for calculating the thickness of each unit in each cell was to separately isopach each interval and use those as inputs of sediment thickness for each geologic unit. However, for logistic reasons, we did not have access to the data required to accomplish this during this phase of the study.

As an alternative, a data set from Earth Studies Group (*unpublished data* from Fillon, 2006) was employed to create a distribution of the relative thickness of each of the five stratigraphic units over the study area. The base of each of the five units was defined biostratigraphically in the Fillon data set, based on the marker fossils in Table 1. The duration of each geologic unit is also given in Table 1.

Fillon's analysis provides a set of Gulf Coast basin-wide maps of average sediment accumulation rates over 60 time/rock divisions of the post-Middle Jurassic stratigraphic section. A set of 100 locations was randomly generated within the study area (see figure 29). At each of those locations (or "pseudowells"), the thickness of the units in Table 1 was determined by multiplying the sediment accumulation rates by the length of time covered by each of Fillon's interval maps.

For each of the five time/rock units, the distribution of sediment thickness of that unit, as a fraction of total sediment thickness, is shown in figure 30. As expected, the Pleistocene section is the thickest and possesses the broadest range of values of the five units. Both the range and modal value decline going backward in geologic time.<sup>8</sup>

**Table 1**  
**Divisions of Stratigraphic Column**

Geologic Time/ Rock Unit	Duration (million years)	Age of Base (MYBP)	Marker Fossil Used for Base
Pleistocene	1.95	1.95	Discoaster brouweri
Pliocene	3.1	5.05	Ceratolithus acutus / Globigerinoides mitra
Upper Miocene	5.95	11	Discoaster hamatus
Middle Miocene	7.25	18.25	Marginulina ascensionensis
Lower Miocene	6.4	24.65	Lenticulina jeffersonensis - Aq2/Aq1

Independent sampling of these five distributions to generate a sample of five individual unit sedimentary thicknesses in a cell fails to account for a key constraint: the sum of these five thicknesses must equal the thickness of the entire sedimentary section in the cell. To account for this constraint we assume that the *relative proportions* of the entire stratigraphic column in a cell taken up by five sedimentary units possess a Dirichlet distribution.<sup>9</sup>

<sup>8</sup> As the general history of Cenozoic sedimentation in the GOM is that of basinward progradation of the shelf, the further back in geologic time, the further the distance of the study area is from the extant coastline.

<sup>9</sup> See, for example, Johnson and Kotz (1972). It can be shown that, given a set of independent gamma random variables, the Dirichlet distribution is the distribution of relative proportions of the sum of this set of random variables; i.e., divide each random variable by the sum of all random variables in the set to get these proportions.

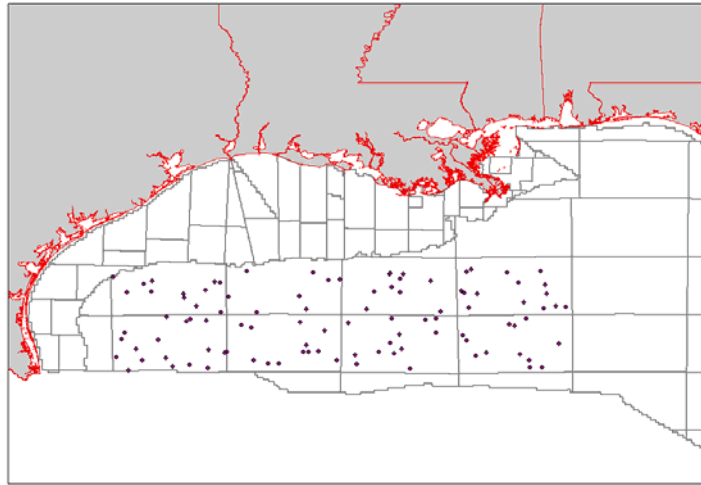


**Figure 29. Locations of 100 randomly located pseudowells used in the construction of distributions of sediment thicknesses by geologic time/rock units over the study area.**

Thicknesses of individual sedimentary units at each of the 100 pseudowell locations are used to estimate parameters of a Dirichlet distribution which, in turn, are used to Monte Carlo relative proportions of the entire sedimentary column in a cell. Multiplication of relative proportions of the cell's total column thickness produces individual unit thicknesses.<sup>10</sup>

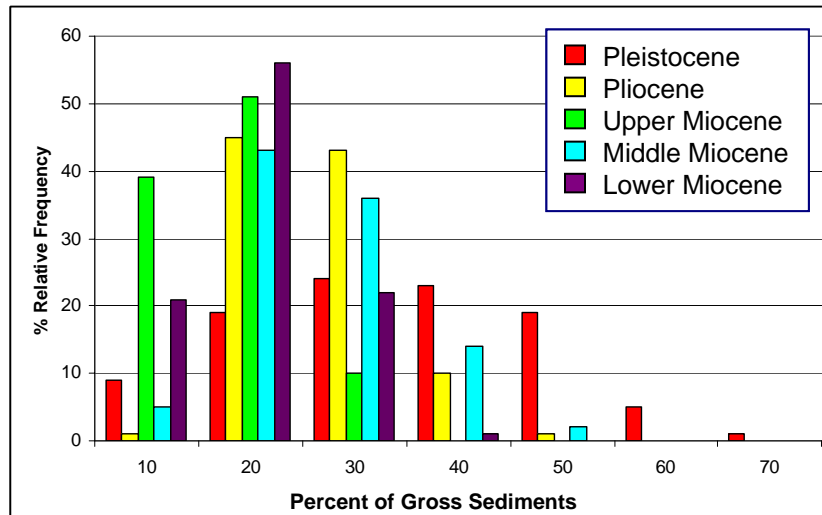


**Figure 30. Distribution of the percent of gross sedimentary thickness encompassed by each of the five geologic time/rock units included in the study, based on 100 samples drawn from the Fillon sediment accumulation rate maps.**

<sup>10</sup> Shape parameters for five gamma distributions, one for each of five sedimentary units, are shown in Table 2. All possess a scale parameter equal to 1.0. At each trial, a Monte Carlo realization of each of the five gamma random variables is rescaled by the sum of all five so that the rescaled proportions add to one. Multiplication of a vector of these five proportions by the thickness of the total sedimentary column in the cell yields a vector of thicknesses of its constituent time/rock units.

**Table 2**  
**Parameters of Gamma Distributions in the Relative Thickness**  
**of Each Stratigraphic Interval**

<b>Geologic Time/ Rock Unit</b>	<b>Gamma Shape Parameter</b>
Pleistocene	1.638
Pliocene	1.500
Upper Miocene	0.976
Middle Miocene	1.464
Lower Miocene	1.133

Each Monte Carlo trial divides the total sedimentary column in a cell into thicknesses of each of the five time/rock units. The mid-point depth of each unit at that trial is computed. These depths are recorded and used to estimate unit permeability.

**b. Determination of Generated Volumes of Biogenic Methane**

Based on the inputs and processes described above, during each Monte Carlo trial, all the described distributions are sampled and combined to produce an output estimate of the volume of in-place methane hydrates in each cell. Typically, there are 1,000 Monte Carlo trials executed for each of the 202,079 2.32-km<sup>2</sup> cells in the GOM study area. These distributions capture cell by cell uncertainty induced by input variable and model parameter uncertainties, and permit calculation of standard statistics such as sample means, variances and ranges. Table 3 summarizes steps in computation of a typical trial value for the biogenic methane generated in a cell.

**Table 3**  
**Algorithmic Summary of Charge Module**

<b>Step</b>	<b>Action</b>	<b>Note</b>
1	Select a catchment	1
2	For cell k = 1 to last cell in catchment	
3	For trial m = 1 to number of trials (default = 1,000)	
4	Initialize age of strata	
5	Get cell water depth, sediment thickness, sand percent, and anomaly	2
6	Draw thickness percents of each stratum	
7	Draw TOC	
8	Draw asymptotic conversion efficiency	
9	Draw water bottom temperature	3
10	Draw geothermal gradient	4
12	Compute thickness of each stratum (i)	
13	Compute mid-point thickness of each stratum (i) and time (j)	
14	Draw seafloor methanogenic productivity	
15	Draw water bottom permeability	
16	Compute stratum sand permeability for stratum (i), and time (j) at depth d	
17	Compute stratum shale permeability for stratum (i), and time (j) at depth d	
18	Compute stratum average permeability for stratum (i), and time (j) at depth d	
19	Compute ratio of permeability of stratum (i) at depth d to seafloor permeability	
20	Compute intercept of productivity function for stratum (i), and time (j)	
21	Integrate marginal productivity function to get cumulative production	
22	Estimate finite integral over ranges of temperatures exposed	
23	Store incremental generation for stratum (i) and time (j)	
24	Compute cumulative generation in stratum (i) through time (j)	

Step	Action	Note
25	Compare cumulative generation through time (j) to asymptotic conversion limit	
26	If cumulative generation stratum (i) > limit (i), set cumulative generation to limit (i)	
27	Sum all incremental generation over all strata	
28	Store result	
29	Begin next trial at Step 3	
30	If final trial, summarize and store methane generation for cell	
31	Begin next cell at Step 2	
32	If final cell in catchment, begin next catchment at Step 1	

Notes to Table 3:

- (1) For the charge module, the GOM study area is divided into hydrodynamically independent catchments composed of a few to scores of cells. How these catchments are constructed is described in the migration model below.
- (2) The anomaly variable is either zero or one, depending whether the cell intersects one of the buffered seismic anomalies identified by Shedd and Hunt.
- (3) and (4) Water bottom temperature and geothermal gradient are described in detail in the container section of this chapter.

The amount of biogenic gas generated in each cell is primarily controlled by the thickness of the stratigraphic section available for conversion to methane (see figure 31). As a result, in areas where the top of salt is very near the seafloor, the generative capacity of the thin stratigraphic section is relatively low. Conversely, deep minibasins with thick stratigraphic sections yield relatively high per-cell generation values. Outboard of the Sigsbee Escarpment, per-cell generation values are relatively high due to the absence of shallow salt and a relatively thick and continuous stratigraphic section.

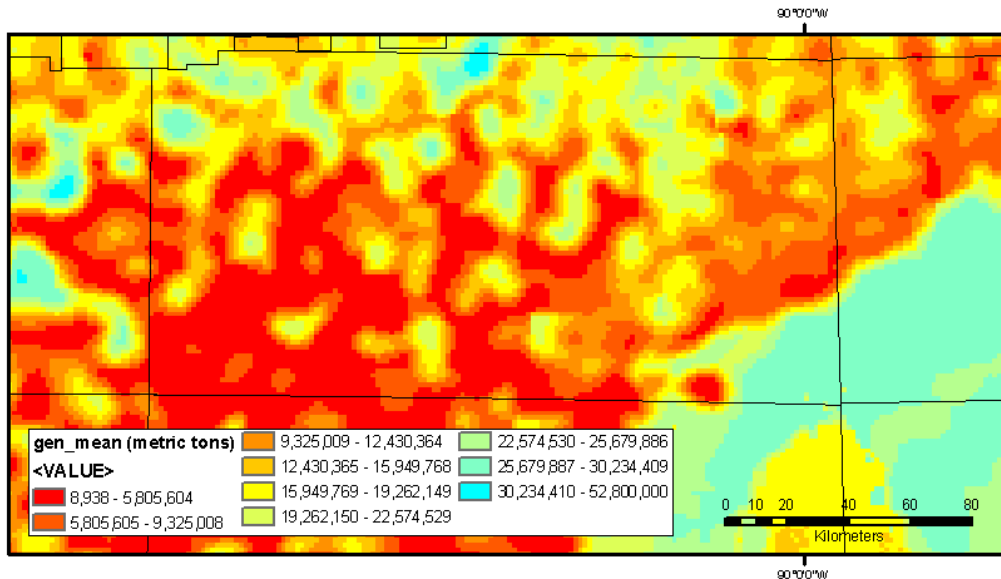


Figure 31. Mean volume of generated biogenic gas in Green Canyon.

## B. Post-Generation Migration of Biogenic Gas

The generation model provides probability distributions of volumes of biogenic methane produced in each cell in the study area. It is certain that not all gas generated in a cell remains in it and charges that cell's HSZ – gas moves laterally as well as vertically. Because a fundamental goal of the project is to produce an assessment with a high spatial resolution (2.32 km<sup>2</sup> cells), we built a model of post-generation migration of methane to locations where it becomes available to charge the HSZ and form methane hydrates.

In addition to the need for spatial resolution of charge, early in the project we recognized that, in the container module, the thickness of the undersaturated zone (UZ) must be estimated and container volume modified to accommodate it. Based solely on temperature and pressure, the (gross) HSZ extends from the phase boundary at the bottom to the seafloor at the top. However, for methane to form hydrates, the water in which it is dissolved must be saturated to at least 100 percent.

At the top of the gross HSZ (i.e., from the seafloor downward), methane saturation in formation water is driven to less than 100 percent. This results from two processes: undersaturated ocean water imposing a concentration gradient with depth, and the action of sulfate-reduction microorganisms. Consequently, despite the presence of requisite temperature/pressure conditions and (undersaturated) methane in formation waters, methane hydrates do not form; this is the UZ. The thickness of the UZ (calculated in the container module described later in this chapter) is a function of flux through the sediment column; thus, a spatial model of methane charge (i.e., flux) is required.

There are two submodels in the migration model (see figure 32). The first submodel represents the distance of lateral movement of methane between cells where it is generated to cells where it becomes available to charge the HSZ. Continuous lateral movement of methane produced in the generation model is represented here as a mix of two end members:

- (1) No lateral movement. In this case 100 percent of migration is completely vertical. Gas generated in a cell is only available to charge the HSZ in that cell (if the HSZ exists in that cell).
- (2) 100 percent of the generated gas is available for lateral migration out of the cell where it is generated. In this case, the directions and magnitudes of gas transport are completely controlled by a function of stratal dip.

In addition to vertical diffusion and dip-driven lateral movement to other cells, gas also moves through the GOM sedimentary section along faults and unconformities. As there is no basinwide mapping of faults and unconformities as migration conduits, gas transport along faults is not separately included in the migration model. We feel, however, that the model of dip-driven migration creates a spatial distribution of charge that, in many cases, captures the impact of migration along faults. Failure to include fault migration is, nevertheless, a limitation of this phase of the study and is probably clearest in an underestimation of the charge potential of off-structure areas where the change in stratal dip is low.

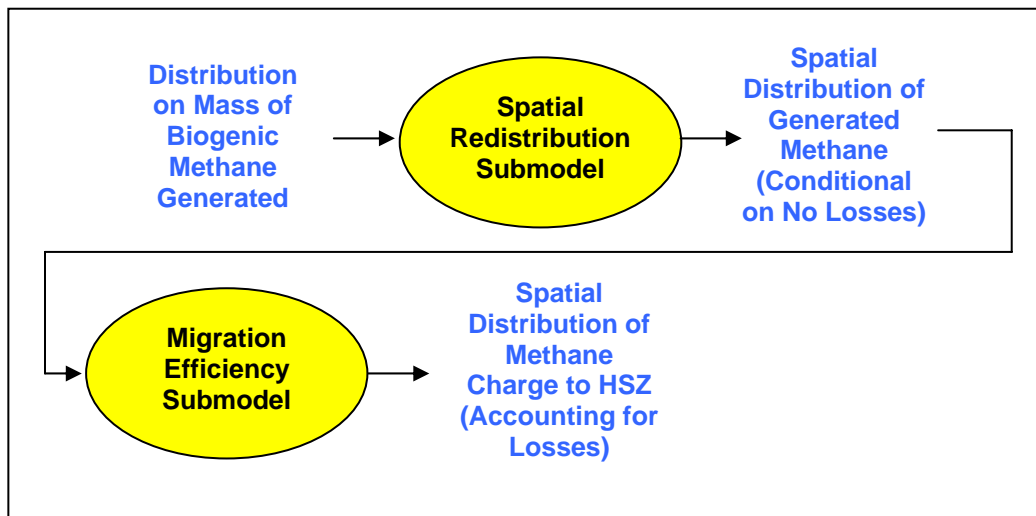


**Figure 32.** A schematic of the migration model, showing the interaction of the spatial and efficiency submodels.



The second migration submodel is non-spatial. It produces a distribution of overall migration efficiency. Migration efficiency is the fraction derived by dividing the mass of methane available to charge the HSZ by the mass of methane generated; one minus this efficiency is the fraction of methane lost in migration. These include all methane mass losses: methane below the HSZ, retained en route from the location of generation; methane that percolated through the HSZ to the overlying UZ; and methane lost to the water column.

These two submodels are combined in the migration model to generate both magnitude and spatial probability distributions of available charge to the HSZ. Charge volume in the integration module is compared to the volume of available pore space to determine the final probability distribution of in-place methane hydrates.

### *1. Spatial Redistribution Submodel*

The spatial redistribution of the mass of methane produced in the generation model captures only “continuous” movements. These are bounded by vertical migration upward in the cell in which the gas is generated; generated gas is completely redistributed laterally based on a theory of dip-driven migration.

If gas migration is 100-percent vertical and methane stays in the cell where it is generated, then the charge map is exactly the same as the generation map (see figure 31 for the mean volume of generation for Green Canyon). This is the 100-percent vertical-migration end member of the spatial redistribution analysis. The wide areal distribution of gas at the surface of the seafloor in the GOM study area suggests that there is a nontrivial likelihood that some share of generated gas percolates from where it is generated straight to the surface. Qualitatively, we presume that the shallower the generation in the section, the higher the probability that the gas remains in the cell where it forms. Therefore, in the spatial redistribution submodel, the assumption of 100-percent vertical migration fully determines the spatial distribution of generated gas.

#### a. Estimation of Migration Catchment Areas

Accepting the limitation that migration along faults and unconformities cannot be included because of lack of data, the alternative to 100-percent vertical migration is that all gas generated is spatially redistributed along the stratal dip. In the simplest model of dip-driven migration, all generated gas would be evacuated from structural lows and redistributed to the structurally highest points in the study area. The magnitude of charge in the cells on the structural highs would be a function of the hydrodynamic catchment areas surrounding them and the volume of generation within the catchment.

Our model builds on this basic idea, with a modification based on empirical data on the spatial distribution of hydrates and hydrate-indicator variables observed on and near the seafloor of the GOM. In adopting this approach, the dip of the surface of the basement estimated by Shedd and Hunt is the basis for estimation of the dip of sediments in the section that control migration. Unquestionably, local dip at any point in the stratigraphic column can be different from the underlying dip of the basement because of faulting, unconformities, compaction, and a host of other reasons. However, the salt-floored basement of the stratigraphic column of the GOM study area is a dramatic and regionally dominant factor in determining stratal dip throughout the sedimentary column of the study area.

Over large areas of the Florida platform and the abyssal plain in the GOM, depositional and allochthonous salt are largely absent. Here, the dip expressed at the basement level is in most cases not conveyed through the remainder of the sedimentary column. Catchment basins in these two geologic settings have been subjectively identified by GOMR interpreters using seismic data analysis, and are not included in the dip-driven submodel described below. Instead, cells within these catchment basins (see figure 33) are assigned a 100-percent vertical migration coefficient.

The geometry of the basement surface is adopted here in the first step of the dip-driven migration submodel for determination of catchment areas across the study area. A catchment is a mirror image of what a watershed is to “migrating” rainwater over a topographic surface. For gas, migrating updip because of buoyancy, a catchment is the union of all contiguous cells across which gas can move laterally without reversing dip (i.e., moving downdip).

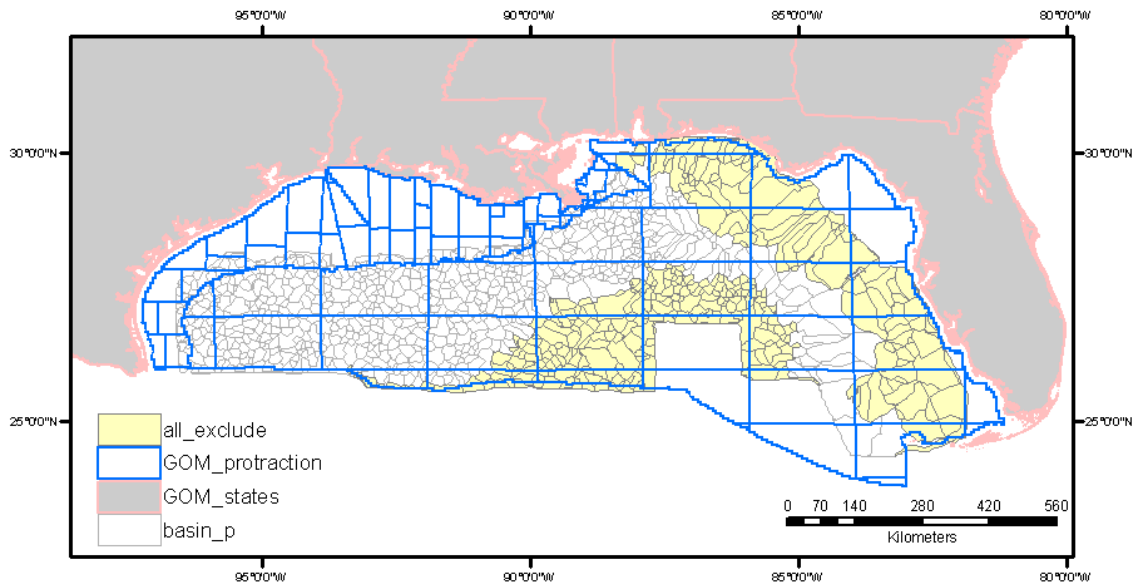


**Figure 33: Catchment basins where the basement surface has minimal effect on the stratal dip of the sedimentary column are highlighted in yellow. Migration of methane is assigned a value of 100-percent vertical.**

Catchments in the GOM are estimated using a geographic information system (GIS), specifically, ArcGIS 9.1 (see figure 34). Two tools from the Toolbox of the Spatial Analyst extension were applied to the raster of basement depth (measured in total vertical distance from mean sea level) prepared by Shedd and Hunt:

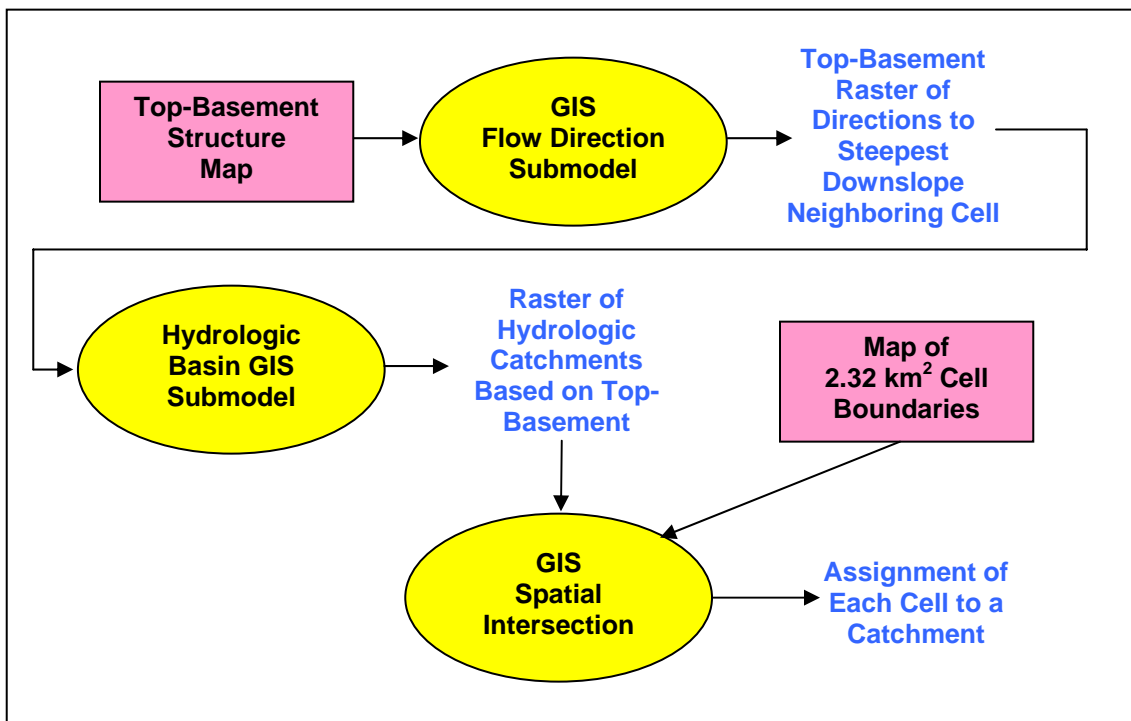


**Figure 34. Steps to create catchment areas for the dip-driven migration submodel based on the geometry of the basement structure map.**

- (1) Flow Direction. For an input surface grid (i.e., depth to top of basement), this tool returns a grid in which each cell records as an attribute the azimuth from it to the cell which is its steepest down-slope neighbor. Steepest descent/ascent is measured by the change in vertical value between neighboring cells divided by the lateral distance between cell centers. The Flow Direction output grid is an input to the Basin tool.
- (2) Basin. From the input grid from the Flow Direction tool, this basin tool identifies ridge lines between catchments and identifies the connected cells within them. For gas migrating updip, no gas would leave the boundaries of catchment defined by the tool, as it would require downdip migration at the ridge lines along the boundary to enter an adjoining catchment.

A catchment area identification (ID) variable is assigned to all of the cells in the study area by spatial intersection within the GIS of the layer containing the catchment boundaries with the grid of 2.32 km<sup>2</sup> cells. The catchment areas for Green Canyon are shown in figure 35 (as grey lines) superimposed on a map of the true vertical depth to the top of the basement.

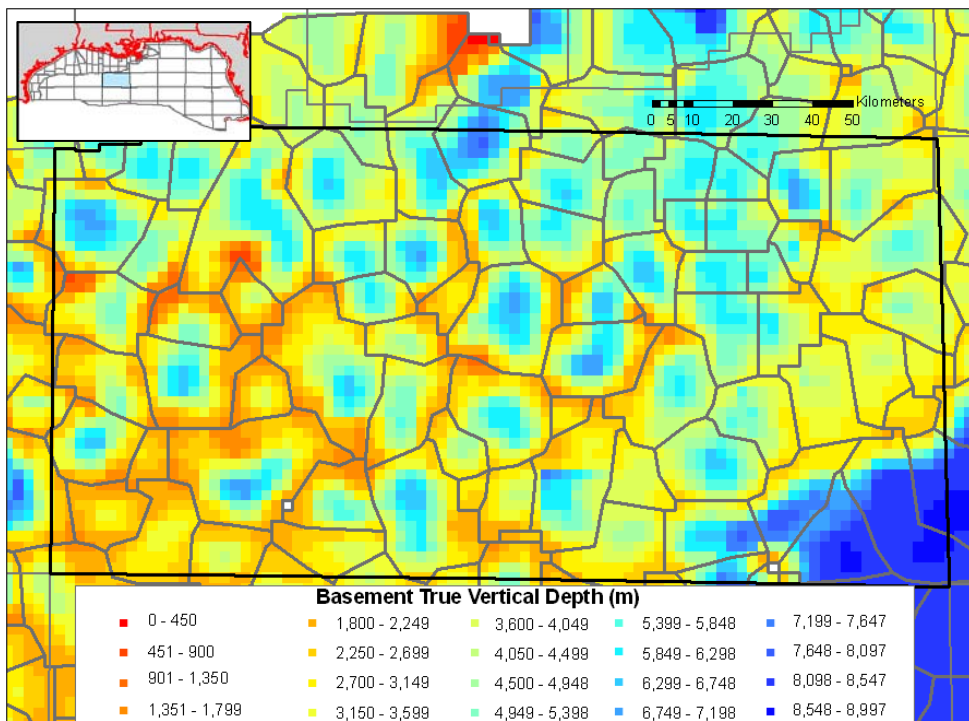


**Figure 35. Relation of depth to basement and catchment areas estimated for dip-driven migration analysis. The boundaries of catchments run along ridge lines in the basement surface such that any gas generated within a catchment would not migrate out of it based on dip-driven movement.**

As the catchments are deemed hydrodynamically isolated systems, the redistribution of gas in the dip-driven migration submodel is conducted *by catchment*. For a single Monte Carlo trial, the value of total generation in each cell is summed up in each catchment. This is the volume of gas to be redistributed across the cells in the catchment based on a function of stratal dip in each cell of the catchment (see figure 36).

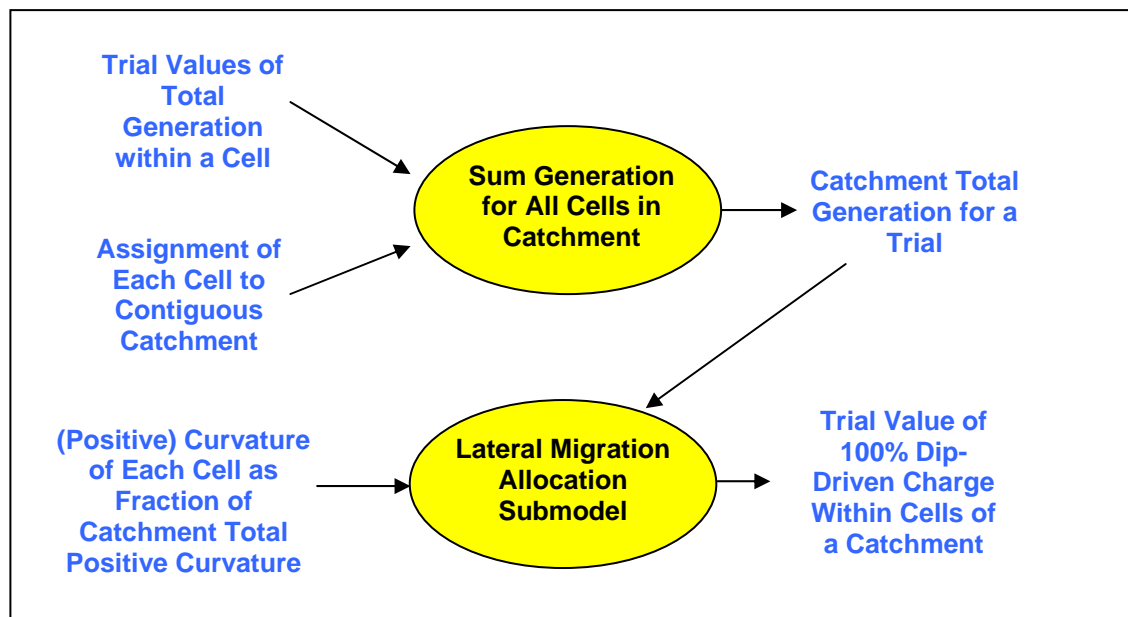


**Figure 36. A schematic of the connection between the summation of gas generation in a catchment to the submodel that redistributes all generated gas in the catchment based on a function of dip.**

**b. 100-Percent Dip-Driven Redistribution of Methane Within a Catchment**

Given that catchment areas are hydrodynamically independent, if all gas generated in a catchment area is redistributed entirely by dip-driven migration, where would the gas concentrate to charge the HSZ? The gas could accumulate simply in the structurally highest points in the catchment, or it could accumulate where the dip of the cell is the highest in the catchment. However, discussions with members of the MMS-GOMR team lead to the conclusion that the empirical distribution of both methane gas vents and observed hydrates is systematically related to structure, but in a more nuanced fashion than these first two hypotheses suggest.

We posit the hypothesis that the focus of dip-driven gas charge in a catchment is a function of the curvature of the strata in it (as measured by the top-basement surface). The first derivative of vertical distance on a three-dimensional surface with respect to lateral distance of a transect on the surface is dip. The second derivative is curvature.<sup>11</sup>

There are three reasons for this approach:

- (1) Empirically, the concentration of direct and indirect evidence of hydrates and gaseous venting of methane at the seafloor appear on the “shoulders” of structural highs in the study area – not on their crests.

<sup>11</sup> The second derivative can be calculated in either the horizontal or vertical plane; here it is calculated in the horizontal plane.

- (2) Coincident with the shoulders of structural highs, anecdotally, is a very high concentration of faults associated with growth of salt diapirs. Evidence of spatial correlation of methane flux with areas of high positive curvature could be either because of stratal migration, the higher density of faults or, most likely, the combination of the two.
- (3) By using curvature, all cells with negative curvature represent the bottom of bowls and would be evacuated of gas.

Computation of the curvature of the basement surface is done in ArcGIS with the Curvature tool in the Spatial Analyst extension. The Curvature tool returns a grid of curvature values for each cell, which is then spatially merged with the grid containing the cell catchment ID and the volume of generated gas for that Monte Carlo trial. The map of curvature of the cells in the Green Canyon protraction area is shown in figure 37. Contour lines of the total vertical depth to the top of the basement (from figure 35) are overlaid on the map of curvatures. Comparing the two, it can be seen that the curvature variable is reflecting the rate of change in dip in the basement surface (i.e., its second horizontal derivative).

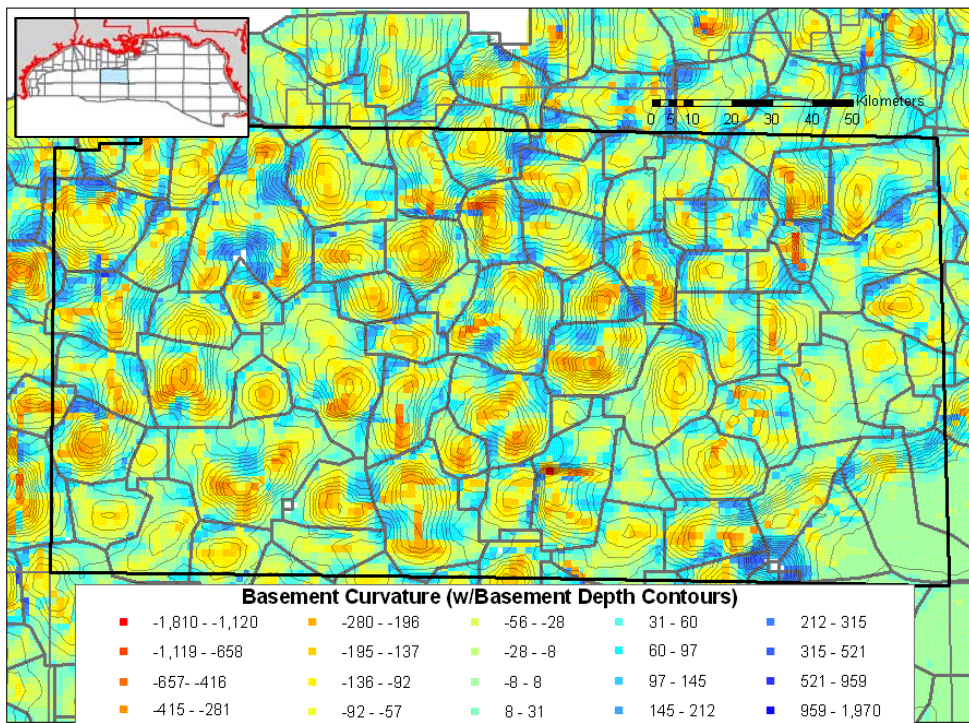


**Figure 37. Estimated curvature of the true vertical depth to top of basement surface. Overlaid on the curvature are contours of the true vertical depth of the top of the basement.**

In the case where migration is 100-percent dip-driven, any cell in a catchment that has a negative curvature would be devoid of gas, as it would have all migrated out. Therefore, in the model of dip-driven migration, all negative-curvature cells are eliminated, and no dip-driven gas charge is assigned to them.

The total generation of gas in a catchment is then redistributed to cells with positive curvature. Curvature values of all cells with positive curvature are summed over all cells in a catchment. The curvature value of each cell in the catchment with positive curvature is divided by this catchment total positive curvature, assigning to each cell the fraction of catchment total curvature belonging to that cell.

For the 100-percent dip-migration case, all gas generated in a catchment on a trial is redistributed to the catchment's cells with positive curvature in proportion to their curvature as a fraction of the total positive curvature in the catchment. Cells with negative curvature get no gas in the 100-percent dip-driven case. The

algorithmic procedure for generating 100-percent dip-driven redistribution of gas in a catchment is shown in figure 38.

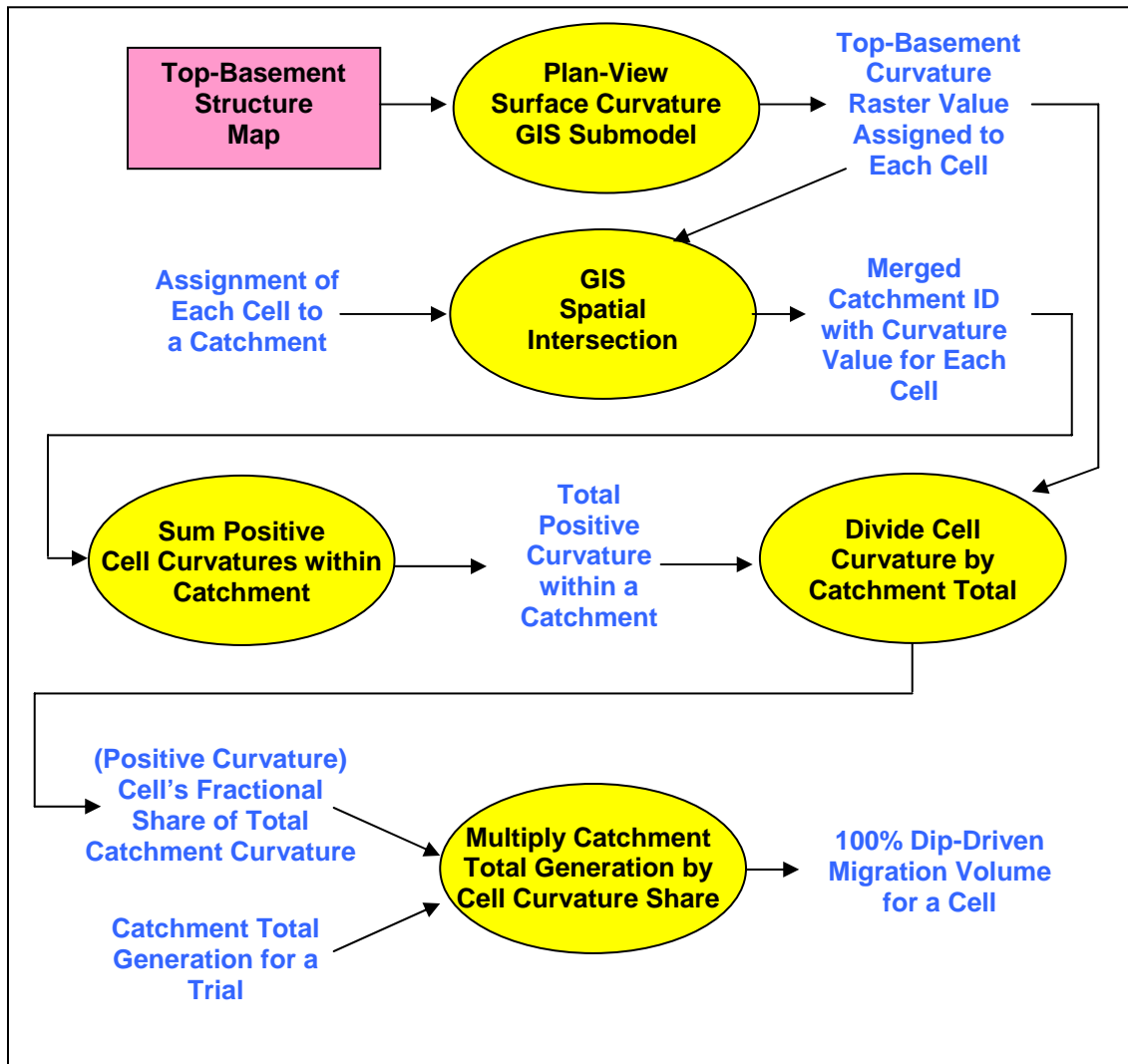


Figure 38. Algorithm for assigning 100-percent dip-driven charge to a cell.

### c. Mixing Ratio for Vertical vs. Dip-Driven Migration

While the analysis of 100-percent dip-driven charge and 100-percent vertical charge represent end members of laterally continuous migration processes, they offer no guidance to what mixture of these two processes best represents the state of nature in the study area.

As a first approximation to a mixing ratio of vertical to dip-driven, the results of both scenarios were compared to the location of the surficial seismic anomalies mapped by Shedd and Hunt. In a test study performed with unbuffered seismic anomaly polygons in the Garden Banks protraction area, the anomaly polygons were overlaid on the 100-percent vertical and 100-percent dip-driven migration maps to determine which of the two scenarios provided more gas to the cells covered by anomaly polygons.



In the Garden Banks test case, anomaly polygons received a greater charge using the 100-percent dip-driven case 59 percent of the time; 41 percent were more fully charged in the vertical migration case. A mixing ratio of 60/40 dip-driven migration is adopted for this phase of the study.

The mixing ratio is considered to be an uncertain quantity. We assign a normal distribution with a mean of 0.6 and a standard deviation of 0.10 to it. In each Monte Carlo trial, a sample is drawn from this distribution (i.e., the mixing ratio) and multiplied by the distribution of dip-driven migration for that cell. The mixing ratio of one minus that value is multiplied by the vertical migration (generation) distribution for that cell to produce a distribution of (mixed-migration mechanism) charge to the cell. The mapped results, which assume 100-percent migration efficiency, are shown in figure 39.

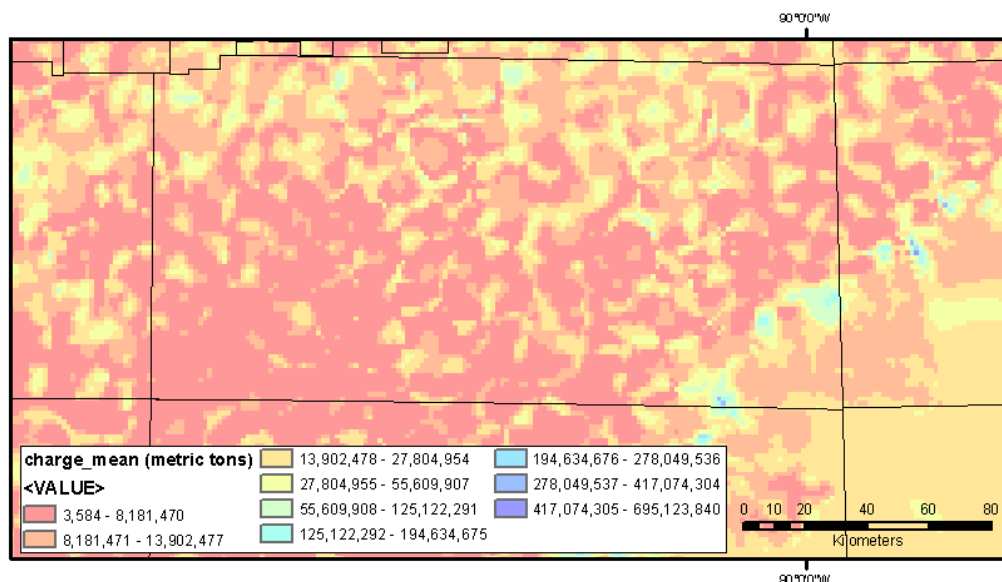


**Figure 39. Estimated mean charge, based on 60/40 dip-driven/vertical migration ratio, in Green Canyon.**

## 2. Migration Efficiency Submodel

Migration efficiency is defined here to be the fraction formed by dividing the volume of gas available to charge the HSZ by the volume of gas generated. For each catchment area, a numerator and a denominator are modeled as a hydrodynamically isolated system. As this definition of migration efficiency is non-spatial, it is used to estimate charge for all cells in a catchment independent of the spatial migration model described earlier. Since methane that passes through the HSZ in gas phase is not available to form hydrates, our migration efficiency parameter implicitly includes trapping, or retention efficiency.

The nature of migration efficiency of oil and gas in conventional hydrocarbon resource assessment has been debated for decades. There is very little consensus about migration efficiency of oil and even less agreement (and understanding) of the efficiency of gas migration. As a result, there is no rich set of analog analyses that informs how much biogenically generated methane in a catchment will be available to form methane hydrates.

We believe that migration efficiency of a system that ends in methane reservoir in hydrate form is greater than the migration efficiency of a conventional system in which methane is reservoir in gas phase. The reason is that hydrate accumulations are, at least to some extent, self-sealing; they are volumetrically less dependent on a competent lithologic top-seal to retain methane in the reservoir. We have no quantitative control on the factor by which hydrate self-sealing improves the retention efficiency of methane in gas phase.

The migration efficiency of conventional hydrocarbon systems serves as a starting point for estimating this parameter for hydrates in the GOM. In this assessment, the starting point is two narrow studies of conventional

oil and gas resources on the GOM shelf. The first is a proof-of-concept analysis, which examines migration efficiency for two GOM shelf plays. The second study, performed by personnel in the MMS-GOMR office, expands and improves the initial analysis.

#### a. Migration Efficiency Analysis for Two Conventional Shelf Plays

The MMS, as part of its assessment responsibilities, has defined several dozen aggregates of oil and gas accumulations on the GOM shelf that it calls “plays.” For each play, MMS defines two geographic boundaries: the “play limit” and the “hydrocarbon limit” (see figure 40). The former defines the area within which hydrocarbons reservoid in the play’s principal reservoir facies are expected to exist. For that reason, the play limit is also known as the “sand limit,” outlining the areal extent of the facies that defines the play (e.g., Middle Pleistocene Progradational).

The hydrocarbon limit is the subset of the play area where mobile hydrocarbons have been found. There is no exact definition of how far from a discovered accumulation the hydrocarbon limit is set; it usually lies within a 1- to 3-mile outboard of the peripheral fields of the play. Nevertheless, within the hydrocarbon limit, there is ample empirical evidence that necessary and sufficient conditions for conventional, recoverable oil and gas accumulations are met.

The objective of the analysis is to compare the area in which a play’s hydrocarbons are assumed to have been generated to the area occupied by discovered and estimated undiscovered accumulations. Assuming that the thickness of the saturated section in all accumulations and in the area between them in a play is relatively uniform, the ratio of area charged to area of generation produces a first-order estimate of migration (and trapping) efficiency.

The basic data for analysis of the Middle Miocene 7 Progradational (MM7P) play and the Middle Pleistocene Progradational (MPLP) play are given in Table 4 and Table 5, respectively. Two approaches are adopted for estimating the numerator—the area charged in conventional oil and gas accumulations. Two approaches are also adopted in estimating the denominator—generation area.

For the numerator, the more conservative approach is to sum the areas of discovered pools reservoid in the play and “gross up” this sum for estimation of the sum of the areas of undiscovered pools. The less conservative approach is to take the areas of entire fields that fall within either the hydrocarbon limit or play limit. For the denominator, the more conservative approach is to use the area defined by the play limit; the less conservative approach is to do the same using the hydrocarbon limit.



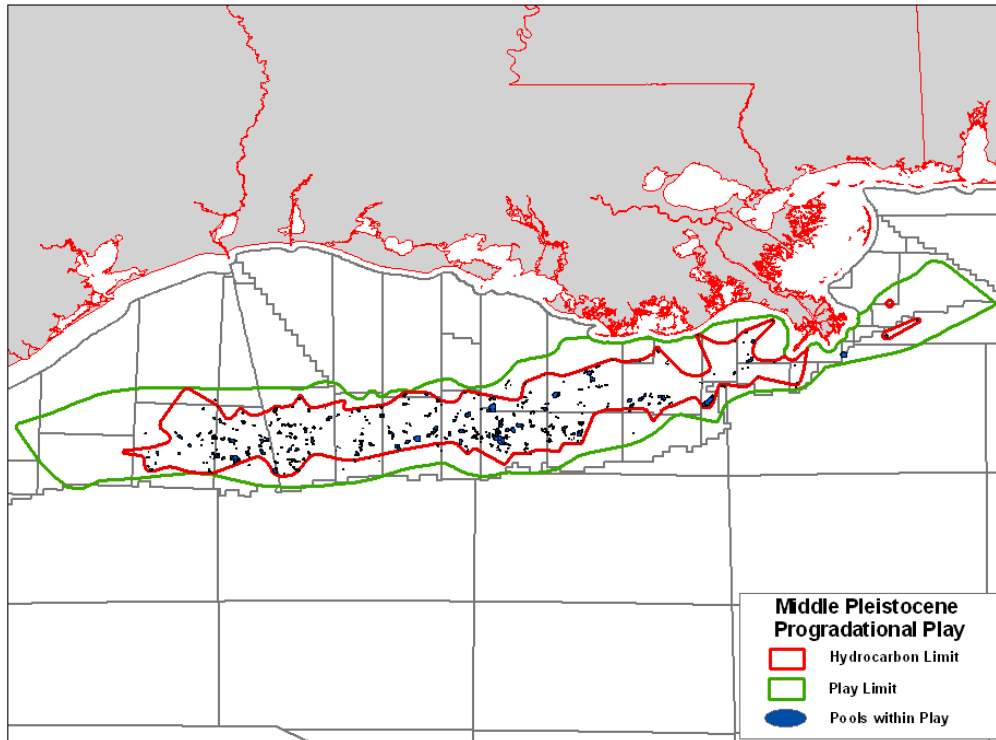


**Figure 40. Outlines of hydrocarbon limit and play limit for the Middle Pleistocene Progradational (MPLP) play. The areal extent of discovered commercial accumulations in the MPLP play are shown as blue polygons.**

These two approaches yield estimates of migration efficiency for conventional resources for the two plays, ranging from approximately 2 percent to 11 percent. The high end of this range aligns with commonly expressed anecdotal ranges for hydrocarbon migration/trapping efficiency. As expected, the “tighter” hydrocarbon limit in the denominator leads to a higher estimated efficiency.

b. Broader Analysis of Shelf Play Migration Efficiencies

Personnel from the MMS office in New Orleans applied the analysis to a total of 27 plays. They provide estimates of migration/trapping efficiency for each of these plays, using two variants of play definitions. Their methodology generally follows that described above; details are provided by the MMS authors in Appendix F.

Results of the MMS migration/trapping efficiency study are shown in Table 6 and Table 7. The MMS team uses both aggregated and unaggregated play definitions (see Appendix F) and does not account for the area that would be occupied by estimated undiscovered hydrocarbons in each play. As a consequence, their estimates of efficiency are lower than the field-level analysis presented for the MM7P and MPLP plays. Moreover, their analysis does not expand the value of the numerator in the efficiency fraction to include the area of entire fields (as in the field-level analysis above), but stays with the stratigraphically consistent practice of including only areas of pools that are reservoirized in the facies that defines the play.

**Table 4**  
**MM7 Progradational Play – Migration/Trapping Efficiency Analysis**

<b>Variable</b>	<b>Value</b>	<b>Units</b>
<b><i>Play Area Data</i></b>		
Area of hydrocarbon limit	8.32 x 10 <sup>9</sup>	m <sup>2</sup>
Area of play limit	3.59 x 10 <sup>10</sup>	m <sup>2</sup>
<b><i>Pool Level Analysis</i></b>		
Number of pools in play	71	
Discovered estimated ultimate recovery	1.59 x 10 <sup>9</sup>	BOE
BOE recovery factor	0.48	
Area of discovered pools	5.71 x 10 <sup>8</sup>	m <sup>2</sup>
Discovered in-place hydrocarbons	3.31 x 10 <sup>9</sup>	BOE
Discovered in-place (pool) plan-view density	5.79	BOE/m <sup>2</sup>
Mean undiscovered hydrocarbons	1.7 x 10 <sup>8</sup>	BOE
Estimated reserve appreciation	3.1 x 10 <sup>8</sup>	BOE
Estimated unproved reserves	1.0 x 10 <sup>6</sup>	BOE
Anticipated total future reserve additions	4.8 x 10 <sup>8</sup>	BOE
Anticipated in-place hydrocarbons (based on RF=0.48)	1.00 x 10 <sup>9</sup>	BOE
Percent total discovered	77	%
Discovered + anticipated in-place hydrocarbons	4.31 x 10 <sup>9</sup>	BOE
Area of discovered + anticipated in-place (pool)	7.44 x 10 <sup>8</sup>	m <sup>2</sup>
<i>Efficiency (pool) based on hydrocarbon limit</i>	<i>8.94</i>	<i>percent</i>
<i>Efficiency (pool) based on play limit</i>	<i>2.07</i>	<i>percent</i>
<b><i>Field Level Analysis</i></b>		
Number of fields within play limit	192	
Area of 192 fields	1.14 x 10 <sup>9</sup>	m <sup>2</sup>
Field proved+appreciation+unproved	8.37 x 10 <sup>9</sup>	BOE
Discovered in-place hydrocarbons (based on RF=0.48)	1.74 x 10 <sup>10</sup>	BOE
Discovered field in-place plan-view density	15.26	BOE/m <sup>2</sup>
Undiscovered field in-place (for 77% discovered)	5.20 x 10 <sup>9</sup>	BOE
Field total in-place (disc'd + anticipated)	2.26 x 10 <sup>10</sup>	BOE
Area of discovered+anticipated in-place (fields)	1.48 x 10 <sup>9</sup>	m <sup>2</sup>
<i>Efficiency (field) based on play limit</i>	<i>4.12</i>	<i>percent</i>
Number of fields in hydrocarbon limit area	84	
Area of 84 fields	6.82 x 10 <sup>8</sup>	m <sup>2</sup>
Field proved+appreciation+unproved	5.15 x 10 <sup>9</sup>	BOE
Discovered in-place hydrocarbons (based on RF=0.48)	1.07 x 10 <sup>10</sup>	BOE
Discovered field in-place plan-view density	15.68	BOE/m <sup>2</sup>
Undiscovered field in-place (for 77% discovered)	3.19 x 10 <sup>9</sup>	BOE
Field total in-place (discovered + anticipated)	1.39 x 10 <sup>10</sup>	BOE
Area of discovered+anticipated fields (in-place)	8.85 x 10 <sup>8</sup>	m <sup>2</sup>
<i>Efficiency (field) based on hydrocarbon limit</i>	<i>10.65</i>	<i>percent</i>

Note: RF = recovery factor

**Table 5**  
**Middle Pleistocene Progradational Play – Migration/Trapping Efficiency Analysis**

<b>Variable</b>	<b>Value</b>	<b>Units</b>
<b><i>Play Area Data</i></b>		
Area of hydrocarbon limit	2.32 x 10 <sup>10</sup>	m <sup>2</sup>
Area of play limit	5.13 x 10 <sup>10</sup>	m <sup>2</sup>
<b><i>Pool Level Analysis</i></b>		
Number of pools in play	169	
Discovered estimated ultimate recovery	2.91 x 10 <sup>9</sup>	BOE
BOE recovery factor	.54	
Area of discovered pools	6.90 x 10 <sup>8</sup>	m <sup>2</sup>
Discovered in-place hydrocarbons	5.39 x 10 <sup>9</sup>	BOE
Discovered in-place (pool) plan-view density	7.81	BOE/m <sup>2</sup>
Mean undiscovered hydrocarbons	3.96 x 10 <sup>8</sup>	BOE
Estimated reserve appreciation	9.07 x 10 <sup>8</sup>	BOE
Estimated unproved reserves	4.0 x 10 <sup>6</sup>	BOE
Anticipated total future reserve additions	1.31 x 10 <sup>9</sup>	BOE
Anticipated in-place hydrocarbons (based on RF=0.54)	2.42 x 10 <sup>9</sup>	BOE
Percent total discovered	69	%
Discovered + anticipated in-place hydrocarbons	7.81 x 10 <sup>9</sup>	BOE
Area of discovered + anticipated in-place (pool)	9.89 x 10 <sup>8</sup>	m <sup>2</sup>
<i>Efficiency (pool) based on hydrocarbon limit</i>	<i>4.26</i>	<i>percent</i>
<i>Efficiency (pool) based on play limit</i>	<i>1.92</i>	<i>percent</i>
<b><i>Field Level Analysis</i></b>		
Number of fields within play limit	389	
Area of fields	2.0 x 10 <sup>9</sup>	m <sup>2</sup>
Field proved+appreciation+unproved	2.47 x 10 <sup>10</sup>	BOE
Discovered in-place hydrocarbons (based on RF=0.54)	4.57 x 10 <sup>10</sup>	BOE
Discovered field in-place plan-view density	22.87	BOE/m <sup>2</sup>
Undiscovered field in-place (for 69% discovered)	2.05 x 10 <sup>10</sup>	BOE
Field total in-place (discovered + anticipated)	6.62 x 10 <sup>10</sup>	BOE
Area of discovered+anticipated in-place (fields)	2.89 x 10 <sup>9</sup>	m <sup>2</sup>
<i>Efficiency (field) based on play limit</i>	<i>5.63</i>	<i>percent</i>
Number of fields in hydrocarbon limit area	216	
Area of fields	1.32 x 10 <sup>9</sup>	m <sup>2</sup>
Field proved+appreciation+unproved	1.78 x 10 <sup>10</sup>	BOE
Discovered in-place hydrocarbons (based on RF=0.54)	3.29 x 10 <sup>10</sup>	BOE
Discovered field in-place plan-view density	24.92	BOE/m <sup>2</sup>
Undiscovered field in-place (for 69% discovered)	1.48 x 10 <sup>10</sup>	BOE
Field total in-place (discovered + anticipated)	4.77 x 10 <sup>10</sup>	BOE
Area of discovered+anticipated fields (in-place)	1.91 x 10 <sup>9</sup>	m <sup>2</sup>
<i>Efficiency (field) based on hydrocarbon limit</i>	<i>8.23</i>	<i>percent</i>

Note: RF = recovery factor

**Table 6**  
**Estimates of Accumulation Density for 18 Unaggregated GOM Shelf Plays**

<b>Play</b>	<b>Play Area (Acres)</b>	<b>Formation Sand Area (Acres)</b>	<b>Formation/Play Percentage</b>
Corsair	1,359,465	78,962	5.81%
Upper Lower Miocene Aggradational	2,674,046	14,195	0.53%
Middle Lower Miocene Aggradational	1,587,594	16,068	1.01%
Middle Middle Miocene Retrogradational	2,608,130	79,050	3.03%
Lower Middle Miocene Retrogradational	4,885,286	84,304	1.73%
Upper Middle Miocene Aggradational	4,524,371	6,247	0.14%
Middle Middle Miocene Aggradational	4,573,674	11,062	0.24%
Lower Middle Miocene Aggradational	1,557,947	9,125	0.59%
Upper Upper Miocene Progradational	21,793,502	1,119,748	5.14%
Lower Upper Miocene Progradational	15,833,259	420,873	2.66%
Upper Pliocene Progradational	24,317,741	658,207	2.71%
Lower Pliocene Progradational	19,000,501	380,582	2.00%
Upper Pliocene Aggradational	13,552,583	103,439	0.76%
Lower Pliocene Aggradational	6,369,109	54,743	0.86%
Middle Pleistocene Progradational	13,095,638	106,133	0.81%
Lower Pleistocene Progradational	16,096,425	661,425	4.11%
Middle Pleistocene Aggradational	9,203,389	122,886	1.34%
Lower Pleistocene Aggradational	15,446,771	156,319	1.01%

**Table 7**  
**Estimates of Accumulation Density for 9 Aggregated GOM Shelf Plays**

<b>Play</b>	<b>Play Area (Acres)</b>	<b>Formation Sand Area (Acres)</b>	<b>Formation/Play Percentage</b>
Pleistocene Aggradational	15,446,771	319,378	2.07%
Pleistocene Progradational	16,096,425	773,572	4.81%
Pliocene Aggradational	13,557,583	158,182	1.17%
Pliocene Progradational	25,751,079	1,039,059	4.04%
Upper Miocene Progradational	21,962,976	1,540,621	7.01%
Middle Miocene Aggradational	4,723,434	26,434	0.56%
Middle Miocene Retrogradational	5,933,524	163,354	2.75%
Lower Miocene Aggradational	3,053,840	30,263	0.99%
Corsair	1,359,465	78,962	5.81%

c. Estimation of Distribution of Migration Efficiency

Although both studies employed to determine migration efficiency are enlightening, neither answers the question: "What fraction of generated methane will be reservoired and retained as hydrates?" Because both studies include only conventional oil and gas accumulations, we assume that the fields and reservoirs studied are sourced principally by thermogenically generated hydrocarbons. In contrast, while we postulate that most biogenic gas is generated within the top 2 km of section below the seafloor, thermogenic hydrocarbons can be generated at depths two to three times as deep.

Because migration efficiency includes the loss of gas in vertical migration between the point of generation and the HSZ, the deeper the source of generation, the greater the presumed loss en route. This alone leads us to expect that the migration efficiency of biogenic gas charging the HSZ is substantially higher than the efficiency of thermogenic gas traveling a much greater vertical distance.

Additionally, unlike conventional oil and gas accumulations in the GOM, methane reservoirs in hydrate form provides at least some self-sealing, obviating the need for a competent lithologic top-seal for a trap to form. Because of this, the highest possible migration efficiency for biogenic gas generated proximate to or even in the HSZ and migrating only a short distance in gas phase before being trapped (permanently?) in the HSZ is 100 percent.

On the other hand, there is no reason to believe that the migration/trapping efficiency for biogenic gas charging hydrates in the HSZ would ever be lower than that observed for conventional hydrocarbons.

The entire GOM hydrate assessment team met several times to discuss the range of migration efficiencies. The most likely value of migration efficiency adopted is several times higher than the mid-point of the range of efficiencies for conventional oil and gas discussed above. The final distribution, combining migration and trapping efficiencies into a single factor, is modeled by a beta distribution. The parameters of it are ( $\alpha = 4, \beta = 10$ ), the mean is 0.286, the mode is 0.25, and the standard deviation is 0.117. The distribution is shown in figure 41.

In summary, there is a good geologically based rationale for assuming that migration efficiencies for gas hydrate are substantially greater than conventional oil and gas migration efficiencies, but no measurable data that confirms it. Until such data become available, we are forced to rely on expert judgment. The distribution shown in figure 41 encodes the expert opinion reached after these discussions.

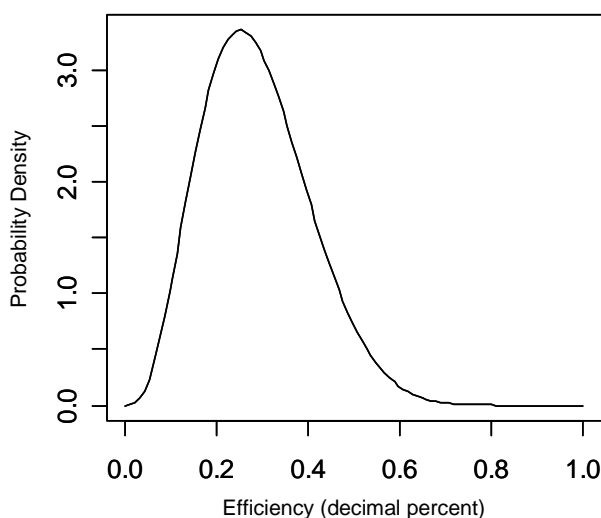


**Figure 41: Probability distribution for the migration/trapping efficiency parameter.**

### **C. Thermogenic Charge**

The treatment of thermogenic charge to the shallow section is pure ad hoc, but, we believe, ad hoc that has a sound scientific basis. As stated earlier, a mass of thermogenically-generated methane per cell was not calculated. However, we assume that if the flux of methane entering the shallow section from below (presumably along fault planes) is large enough for it to vent to the surface, there is little possibility of the hydrate systems in these cells to be charge-limited. Therefore, thermogenic charge in this preliminary analysis is strictly limited to cells that are coincident with the surficial seismic anomalies described in Chapter III.

Thermogenic charge for surficial anomaly cells is handled in the last step of the analysis, after the determination of the accommodation space available in the net HSZ. For all cells within the bounds of anomalies, the estimated accommodation space is completely filled with thermogenic gas.

Many authors (e.g. Milkov and Sassen, 2001) have recognized the presence of thermogenic gas hydrate accumulations in the GOM, especially in the vicinity of active seafloor seeps. While not included in this initial release, the MMS plans to model thermogenic gas generation in the future as the hydrate assessment model is modified and improved.

## Container Module

The study area's rock volume that is a candidate for formation of natural gas hydrates is estimated in two steps. First, we employ a model to estimate the "gross" HSZ. The gross HSZ covers that volume of rock in which pressure, temperature and salinity conditions permit the formation of hydrates, if available pore space and sufficient hydrocarbon charge are present. Second, we then remove a layer of the gross HSZ, starting at the seafloor and extending downward. In this layer, saturation of methane in ambient waters is believed to be below 100 percent. Where formation waters are undersaturated, hydrates will not form. Here we call a layer in which this condition is present the "undersaturated zone" (UZ). The gross HSZ, minus the UZ yields the net HSZ.

### A. Estimating the Thickness of the Gross Hydrate Stability Zone


Estimation of the gross HSZ is based on a basic relationship described by Milkov and Sassen (2001) (hereafter referred to as *M/S*). Their fundamental equation is an implicit function in which two relationships are set equal to each other to establish a phase boundary in temperature and pressure. For pressures less than that at the phase boundary and, simultaneously, temperatures greater than that at the phase boundary, methane will occur in gas phase. At pressures greater than the boundary and, simultaneously, temperatures below the boundary, methane molecules are trapped in frozen water molecules, forming hydrates.

Pressure at a point on or below the seafloor is taken to be a function of its depth below mean sea level (i.e., water depth plus depth below seafloor). Temperature at that point is the sum of temperature at the seafloor plus depth below seafloor times the geothermal gradient. Both seafloor temperature and geothermal gradient are taken by *M/S* to be functions of water depth, as shown in their notation in Eq. (2.1).

Eq. (2.1) is solved for a value of *C*, the depth below the seafloor at which ambient temperature and pressure are equal to the value of the phase stability expression. This depth marks the bottom (in meters below seafloor, mbsf) of the gross hydrate stability zone and thereby defines its gross thickness. If pressure is too low and/or temperature too high in any cell, the thickness of the gross HSZ will equal zero, and no hydrates are expected.

Milkov and Sassen provide three versions of their basic stability equation. The parameters of the phase stability expression in Eq. (2.1) are dependent on the chemical composition of the gas entering hydrate form. The version shown in Eq. (2.1) has the parameters for a gas which is 100-percent CH<sub>4</sub>:

$$(2.1) \quad f(B) = \underbrace{-(-9.6 \times \ln(B) + 88.4) \times C/1000}_{\text{geothermal gradient}} - \underbrace{295.1 \times B^{0.6}}_{\text{water bottom temperature}} + \underbrace{8.9 \times \ln(C + B) - 50.1}_{\text{phase stability expression}}$$


  
 sediment temperature expression

where,

*B* = water depth in meters

*C* = thickness of the hydrate stability zone in meters

Milikov and Sassen use a standard Newton-Raphson algorithm to solve Eq. (2.1) numerically.

The solution to Eq. (2.1) is an estimate of  $C$ , the thickness of the HSZ, for a given water depth. In addition to the parameter values in Eq.(2.1), M/S provide phase stability parameters for gas of 95.6-percent and 90.4-percent methane.

In this study, the basic analytic expression Eq. (2.1) for determination of the gross HSZ is modified in several important ways:

- (1) The M/S approach does not include the influence of local salt on either sediment temperatures or on pore water salinity (which moves the phase stability boundary).
- (2) The expression for water bottom temperature is replaced with what we believe to be an improvement of M/S Eq. (2.1).
- (3) As it is impossible to validate independently M/S' hypothesized representation in Eq. (2.1) of geothermal gradient as a function of water depth, we replace it with a new representation.
- (4) The M/S approach is deterministic while our approach is stochastic; here, some parameters in M/S Eq. (2.1) are regarded as uncertain quantities to which we assign probability distributions.

Our version of Eq. (2.1) is described below.

### *1. Influence of Local Salt*

In the GOM, particularly across the slope, salt plays a major role in tectonics and the distribution of sediments on a large scale. On a local scale, the presence of salt impacts pore water chemistry and local sediment temperature. This chemical impact arises through the dissolution of salt at the face of the salt body and its transport away from the salt body by diffusion and through fluid flow. For all points in the section below the seafloor, where salinity exceeds ocean salinity, the phase stability boundary for hydrates shifts. When this happens, the quantity of salt in pore waters above ocean salinity reduces the temperature at which hydrates will form (for a given pressure), making the gross HSZ thinner than it would be otherwise.

For this phase of the analysis, four assumptions are made about the relationship between pore water salinity and distance from a salt body (Bruno and Hanor, 2003; Hanor, 2004; Hanor, 2007).

- (1) Salinity declines as a linear function of the distance from the salt body (Eq. (2.2)).
- (2) The probability distribution of pore water salinity at the salt body face ( $\mu$  in Eq. (2.2)) is assigned a normal distribution with a mean of 215 parts per thousand (ppt) and a standard deviation of 58 ppt.<sup>12</sup>
- (3) The derivative of salinity with respect to distance from the salt face is assigned a normal distribution, with a mean of 0.11 and a standard deviation of 0.07.<sup>13</sup>
- (4) The derivative of hydrate stability temperature with respect to salinity (in parts per thousand) is 22.7.<sup>14</sup>

The additive influence of local salt on pore water salinity (above ambient 35 ppt) and therefore on the phase stability temperature is modeled as:

$$(2.2) \quad \lambda = (\mu - (\pi * SALT))/22.7$$

where,

$\lambda$  = the reduction in phase stability temperature (in °C) due to pore water salinity greater than ambient because of the presence of local salt.

$\mu$  = pore water salinity at the salt face, in ppt.

$\pi$  = reduction in additional pore water salinity due to presence of local salt as a function of distance from salt, in ppt per meter of distance.

SALT = distance from salt, in meters. The distance from salt is taken as the vertical distance between the seafloor and top of salt.

The term  $\lambda$  is subtracted from the phase stability expression in Eq. (2.1) to account for the influence of local salt on hydrate stability, by raising pore water salinity.

<sup>12</sup> Note that the purpose of this function is to describe pore water salinity due to local salt *above* ambient levels, assumed to be 35 ppt. The mean of the distribution of pore water salinity at the salt face is actually 250 ppt – or 215 ppt above ambient; the fractiles of the normal distribution of  $\zeta$  and the specification of  $\eta$  have a similar offset. The standard deviation is based on subjective estimates of the 10-percent and 90-percent fractiles of the distribution (140 ppt for the low and 290 ppt for the high) gleaned from the articles reviewed.

<sup>13</sup> The 10-percent and 90-percent fractiles for the distance from a salt body at which salinity returns to ambient are estimated to be 905 m and 4,114 m respectively.

<sup>14</sup> The 22.7 is derived by running the Sloan (1998) program with varying temperatures and NaCl:

%NaCl/°C	0	2	4	6	8	10
0	2.55	3.18	3.85	4.67	5.68	6.95
3.5	3.03	3.66	4.44	5.41	6.62	8.14
10.5	4.24	5.18	6.34	7.82	9.73	12.22
17.5	6.91	8.60	10.83	13.79	17.76	23.02
24.5	15.88	20.87	27.41	35.65	45.70	57.61
31.5	64.66	80.20	97.83	117.58	139.49	163.58



Local salt also raises local sediment temperatures. Compared to surrounding sandstone and shale, salt is a differentially effective conductor of heat. The temperature field at the top of the salt body is warped by the increase in heat conducted into surrounding sediments. Following O'Brien and Lerche (1988), the decrease in sediment temperature, as a function of increasing distance from salt, is modeled as shown in Eq. (2.3):

$$(2.3) \quad \varepsilon = \zeta(SALT)^{-\eta}$$

where,

$\varepsilon$  = the increase in sediment temperature in a cell, above the sum of the geothermal gradient and water bottom temperature, as a result of the presence of local salt. It is expressed as a multiplicative factor, where 1 equals no influence.

$\zeta$  = the increase in temperature above ambient, at the salt face, in degrees C.

$\eta$  = the reduction of the influence of salt on heat as a function of distance from salt, in degrees C per  $\ln(\text{distance from salt in meters})$ .

SALT = distance from salt, in meters. Here the distance from salt is taken as the vertical distance between the seafloor and top of salt.

We assume that the increase in geothermal gradient (over ambient) at the salt face is uncertain and assign a normal distribution to it. O'Brien and Lerche's (1988) analysis and data suggest that heat at the salt face ( $\zeta$ ) can be reasonably modeled as a normally distributed uncertain quantity with 10-percent/90-percent fractiles at 1.12 and 1.35 times ambient, leading to a normal distribution with a mean of 1.23 and a standard deviation of 0.09.

The same figures suggest that the rate of decline in the influence of local salt on sediment temperature ( $\eta$ ) reaches ambient temperature at an uncertain distance from local salt; this distance is an uncertain quantity to which a Normal distribution is assigned. The 10- to 90-percent fractile interval for this uncertain quantity is 1,600 m to 2,400 m so that it possesses a mean of 2,000 m and a standard deviation of 312.2 m (the rate of decline parameter is assigned a Normal distribution with a mean 0.03 m and a standard deviation of 0.002m).

The expression in Eq. (2.3) enters the final phase stability equation multiplicatively.

## 2. Geothermal Gradient

Milikov and Sassen's original equation for gross HSZ thickness relies on a functional relationship between geothermal gradient and water depth. Data available to us in this phase of the project do not empirically support that relationship. Our data set consists of estimates of geothermal gradients and heat flows from commercial oil and gas wells drilled in the study area (referred to below as the Texas Tech data (Jones, 2003).

The Texas Tech dataset includes 62 wells drilled on the GOM slope. Of the total, 8 provide a geothermal gradient, expressed in degrees Celsius per kilometer ( $^{\circ}\text{C}/\text{km}$ ) of depth. The remaining 54 report heat flow, expressed in milliwatts per square meter.

The Texas Tech observations recorded as heat flow are converted to geothermal gradient by multiplication of heat flow by 1.1. This conversion is based on a regression analysis of paired observations of heat flow and geothermal gradient from the "Global Heat Flow Database" of the International Heat Flow Commission.<sup>15</sup> The

<sup>15</sup> The data from the "Global Heat Flow Database" are available at <http://www.heatflow.und.edu/index2.html>.

data base contains 8,272 marine observations, of which 6,815 include estimates of both heat flow and geothermal gradient. The data and regression of geothermal gradient on heat flow are shown in figure 42.

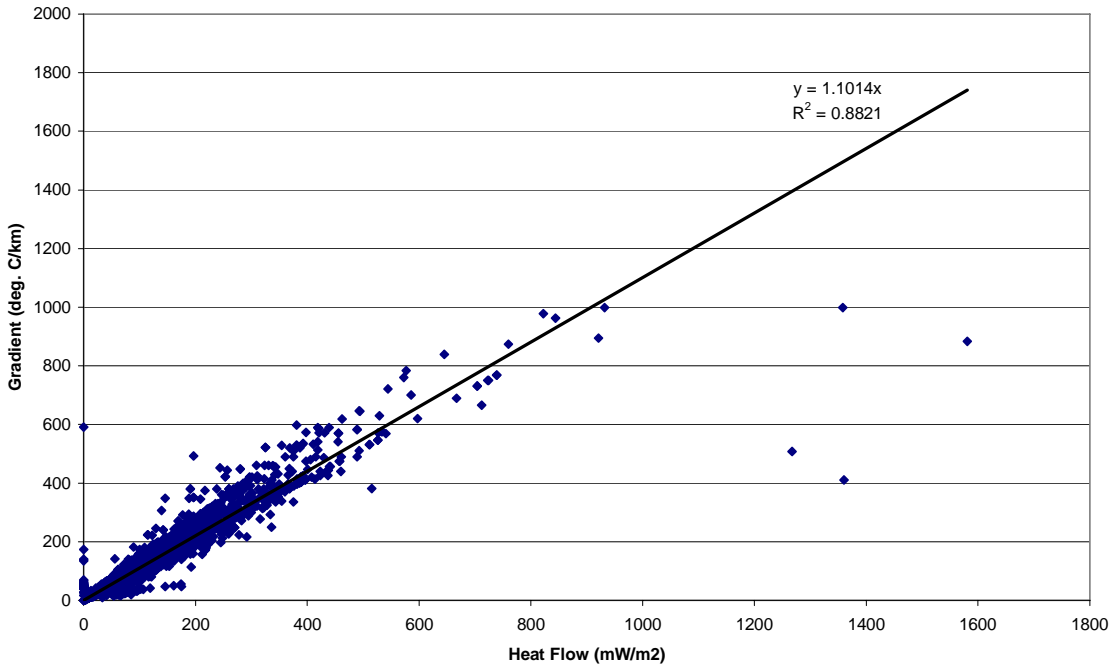


**Figure 42. Relationship between geothermal gradient and heat flow from a database of observations on both measures taken from 6,815 marine observations from the “Global Heat Flow Database”.**

On inspection of the Texas Tech data mapped in figure 43, there is no obvious spatial correlation of geothermal gradient and water depth. Regression of these same data on water depth display no trend; the estimated slope coefficient is practically zero, as is the  $R^2$ , and the correlation coefficient from the 62 Texas Tech points is 0.016 (see figure 44). While a regression of geothermal gradient on water depth that displays a negative slope can be teased from the Texas Tech data, the regression coefficients are statistically insignificant.

The Texas Tech geothermal gradient data, based on 62 wells, has a mean of 40.7 °C/km below seafloor, with a standard deviation of 16.06. The geothermal gradient in our model,  $G$ , is represented by Eq. (2.4).

$$(2.4) \quad G = 14 + 76(X)$$

where,

$x$  is a random variable following a beta distribution.

The parameters of the beta distribution on  $X$  in Eq. (2.4) are  $\alpha = 1.43$  and  $\beta = 2.66^{16}$ . A histogram of the data and scaled fitted density plot are shown in figure 45.

<sup>16</sup> See Evans et al. (2000) for a complete description of the beta and other statistical distribution.

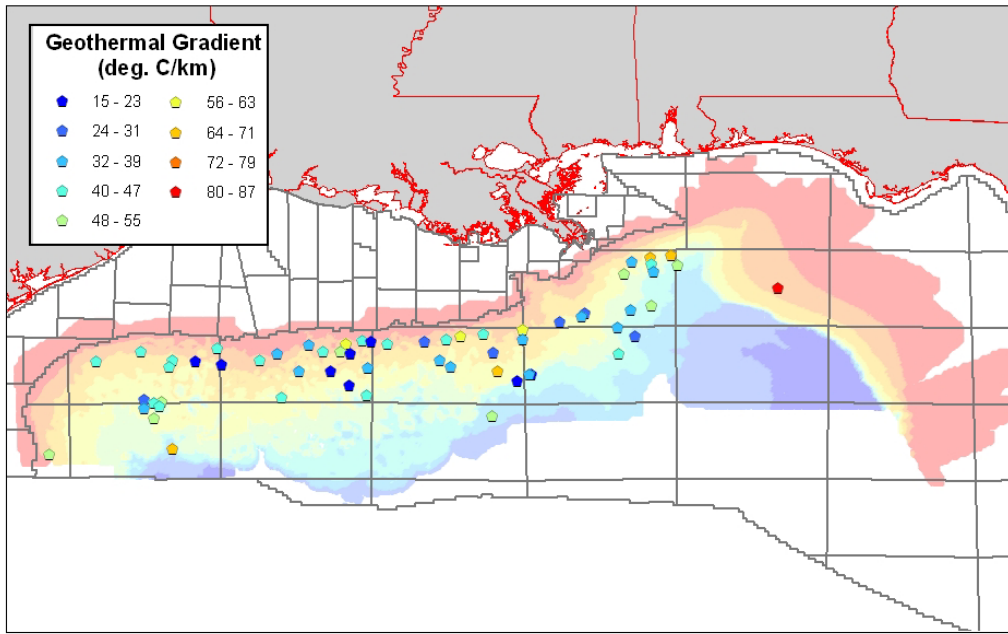


**Figure 43. Texas Tech geothermal gradient data against (semitransparent) water depth. There is no obvious spatial correlation between water depth and geothermal gradient.**

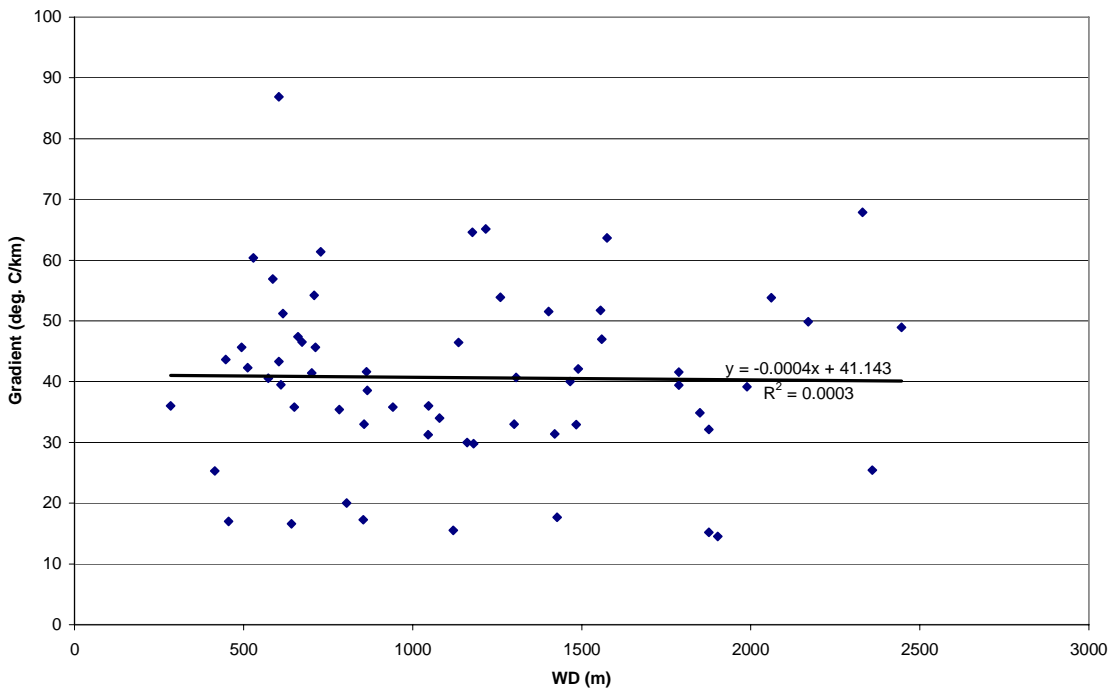


**Figure 44. Scatter plot showing an absence of a statistically significant relationship in the 62 Texas Tech data points on geothermal gradient and water depth.**

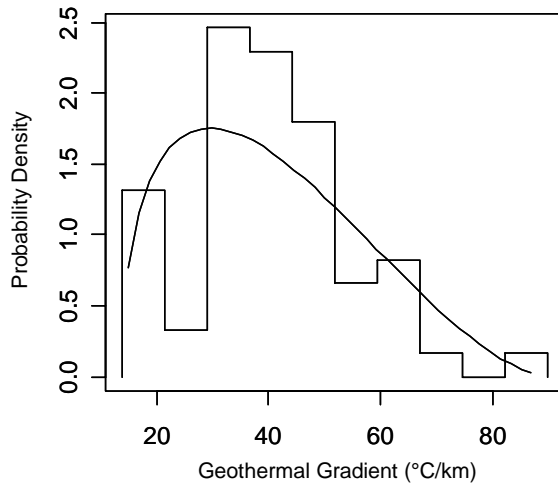


**Figure 45. Raw Texas Tech geothermal gradient data (vertical bars) and fitted beta distribution (line).**

### 3. Water Bottom Temperature

The data used in the analysis of water bottom temperature (WBT) is a combination of 18 vertical profiles obtained from MMS and data from the Johnson Sea Link Dive (Nowlin et al., 2001). The range of water bottom depths from the MMS data is 983.0-2,380.0 m, while the range from the Johnson data is 204.8-908.3 m. The Johnson data were added to obtain information at shallower depths. The form of the model and parameter estimates is shown in Eq. (2.5).

$$(2.5) \quad WBT = a(e^{b(WD)}) + c + \nu$$

where,

WBT = water bottom temperature in degrees Celsius

WD = water depth in meters

$a$ ,  $b$  and  $c$  are parameters to be statistically estimated

$\nu$  = error term.

The nonlinear least squares regression estimates of parameters  $a$ ,  $b$ , and  $c$  are shown in Table 8.

**Table 8  
Parameter Estimates for Eq. (2.5)**

Parameter	Estimate	Std. Error	t-value	Pr(> t )
a	18.2324697	1.2948229	14.08	9.51e-16
b	-0.0031360	0.0001908	-16.44	< 2e-16
c	4.1009028	0.1239134	33.09	< 2e-16

Residual standard error is 0.4425 on 34 degrees of freedom and is assumed to be normally distributed. Residual standard error can be specified in the software system associated with this analysis.

#### 4. Gas Chemistry

Milikov and Sassen's equation (Eq. (2.1)) describes a phase stability relationship for natural gas hydrates; in addition, they provide three sets of values for the slope ( $\delta$  in Table 9) and intercept ( $\gamma$  in Table 9) terms of the phase stability expression. These three parameter pairs correspond to phase stability at three distinct levels of methane as a percent of total gas.

Dr. Roger Sassen, Geochemical and Environmental Research Group (GERG) at the Texas A&M University, also provides a set of 340 observations based on box and shallow piston cores taken over the study area. These include chemical analyses of the hydrocarbons found in the samples as well as the percent of gases that are methane. These data are intersected with the Shedd and Hunt polygons representing surficial seismic anomalies to determine which of the GERG samples lies in an anomaly polygon (on-anomaly) and which lie outside an anomaly polygon (off-anomaly).

Two different distributions on percent methane are fit to the GERG data: one for anomaly areas and one for all areas outside anomalies. The empirical distribution of raw data from both classes, and the fitted distributions that represent them in the model, are shown in figure 46 and figure 47.

**Table 9**  
**Parameters for Phase Stability Expression in Eq. (2.7)**

Methane Content (%)	$\gamma$	$\delta$
100	-50.1	8.9
95.9	-33.9	7.1
90.4	-27.6	6.7

This yields a matrix of four distributions for four parameters: distributions on  $\gamma$  and  $\delta$  for on-anomaly cells and  $\gamma$  and  $\delta$  for off-anomaly cells. These, in turn, are used to derive the values for the terms in Eq. (2.6)

$$(2.6) \quad ((\delta \ln(HSZthnk + WD) - \gamma$$

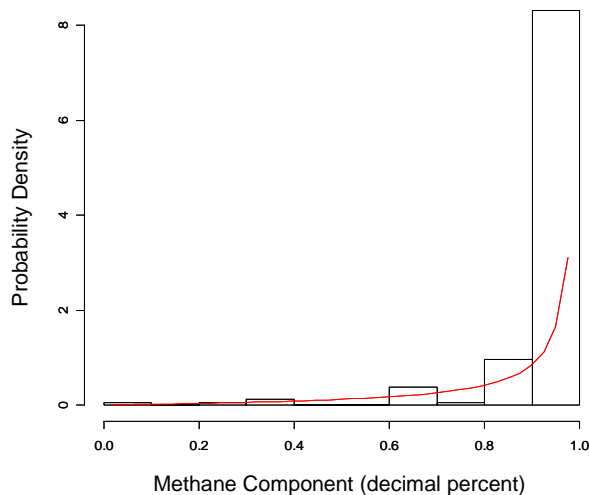


**Figure 46. Raw data on (decimal) percent methane gas from samples located in cells identified as surficial seismic anomalies. Fitted beta distribution shown as red line.**

The mean of the 155 samples taken in on-anomaly cells is 0.9423. The beta distribution fitted to the raw data for on-anomaly samples is  $\alpha = 1.793034$ ;  $\beta = 0.1097103$ .

Raw data and fitted distribution for the samples obtained in cells not associated with surficial seismic anomalies are shown in figure 47. The mean of the 185 raw data points is 0.899. The beta distribution fitted to the raw data for off-anomaly samples is  $\alpha = 1.2379019$ ;  $\beta = 0.1391137$ .

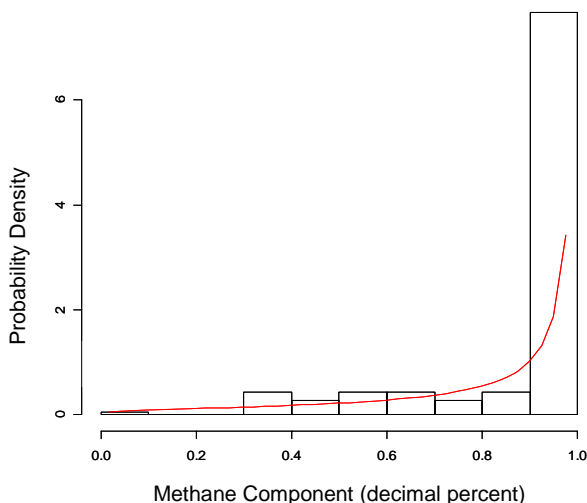


**Figure 47. Raw data on (decimal) percent methane gas from samples located outside cells identified as surficial seismic anomalies. Fitted beta distribution shown as red line.**

The data on the distribution of percent methane were rescaled to produce estimates of  $\gamma$  and  $\delta$  in Eq. (2.6) for both anomaly and off-anomaly cells. The rescaling for all four parameters is given in table 10.

**Table 10  
Rescaling of Gas Chemistry Beta Distributions**

Location	Parameter	Scaling Equation	Final
On-Anomaly	$\gamma$	$\gamma \sim 1 \times \text{beta}(1.793034, 0.10971) + 33.47$	34.41
On-Anomaly	$\delta$	$\delta \sim 2 \times \text{beta}(0.10971, 1.793034) + 7.18$	7.3
Off-Anomaly	$\gamma$	$\gamma \sim 1 \times \text{beta}(1.237902, 0.139114) + 23.66$	24.56
Off-Anomaly	$\delta$	$\delta \sim 2 \times \text{beta}(0.139114, 1.237902) + 6.15$	6.35

Location	Parameter	Beta means	p1	p2	p3	p4
On-Anomaly	$\gamma$	0.942341	1.793034	0.10971	33.46766	1
On-Anomaly	$\delta$	0.057659	0.10971	1.793034	7.184682	2
Off-Anomaly	$\gamma$	0.8989745	1.237902	0.139114	23.66103	1
Off-Anomaly	$\delta$	0.1010255	0.139114	1.237902	6.147949	2

### 5. Specification of Final Model for Estimating the Gross HSZ

To accommodate the changes discussed above, the original M/S equation (Eq. 2.1) was re-written in the following form:

$$(2.7) \quad f(WD) = \underbrace{-\{(GTG \times \varepsilon) \times HSZthk/1000\}}_{\text{geothermal gradient expression}} \underbrace{-\{ae^{b \times WD} + c + v\}}_{\text{water bottom temperature}} \underbrace{+\{(\delta \times \ln(HSZthk + WD) - \gamma) - \lambda\}}_{\text{phase stability expression}}$$

sediment temperature expression

where,

- $WD$  = water depth in meters
- $GTG$  = geothermal gradient, in °C/km
- $\varepsilon$  = multiplicative term for the influence of local salt on sediment temperatures
- $HSZthk$  = thickness of the hydrate stability zone in meters
- $\delta$  = slope of phase stability equation
- $\gamma$  = intercept of phase stability
- $v$  = error of water bottom temperature equation
- $\lambda$  = additive term for the influence of local salt (via salinity) on phase stability temperature.  
Where the calculated value of  $\lambda$  was  $< 1.5$ , it was set to 1.5 (to reflect the impact of ambient 35 ppt salinity)
- $a, b$  and  $c$  = parameters of water bottom temperature equation

Eq. (2.7) is solved by Newton-Raphson for implicit equations. It requires that the derivative of  $f(WD)$ , with respect to the only independent variable ( $WD$ ) in Eq. (2.7) be specified:

$$(2.8) \quad df(WD)/dWD = -\{(GTG \times \varepsilon)/1000\} + (\delta / (HSZthk + WD))$$

Mean values of the gross HSZ generated for the Green Canyon (GC) by a solution to Eq. (2.7) are shown in figure 48, where bathymetry is overlaid on HSZ thickness. The distributions of gross HSZ thickness for GC (by cell) are shown in figure 49. The direct relationship between water depth and gross HSZ thickness is shown in figure 50. The results show that, as expected, as water depth (and therefore pressure) increases, so does the thickness of the gross HSZ. The results also show that gross HSZ calculated in anomaly cells (gas composition drawn from figure 46) has the capacity to be thicker than the gross HSZ calculated in non-anomaly cells (gas composition from figure 47). Other authors have shown the stability zone thickness of thermogenic gas hydrate in the GOM to be significantly thicker than that of biogenic gas hydrate (Milkov and Sassen, 2001).

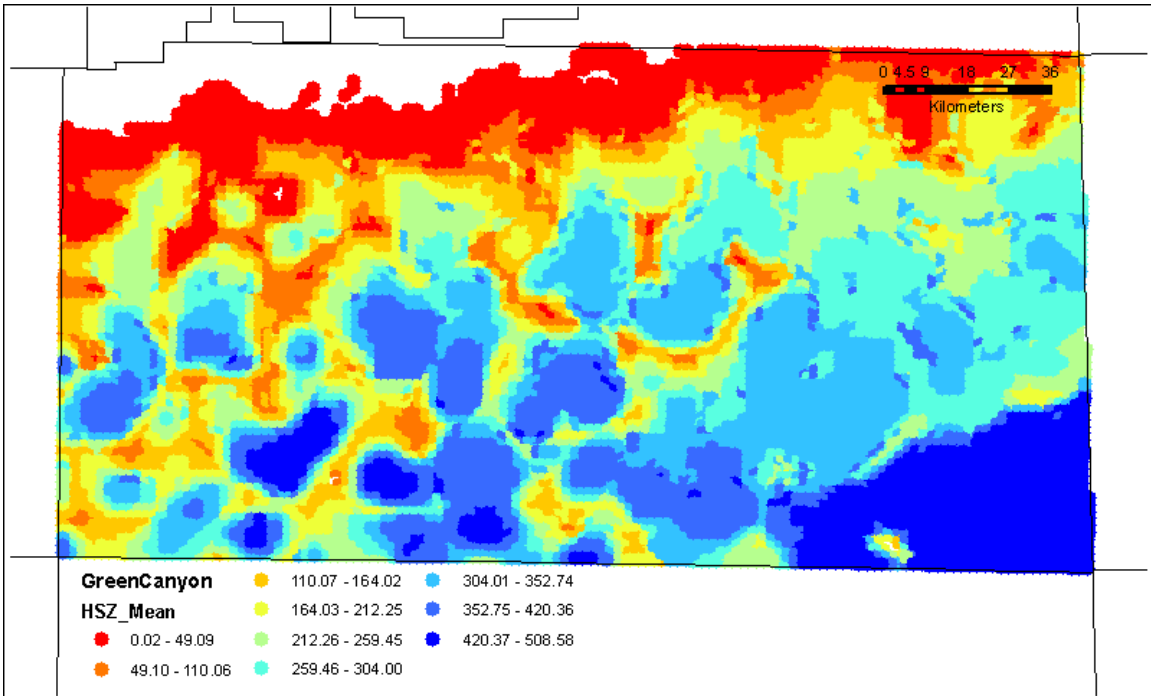


Figure 48. Mean thickness (meters) of the gross hydrate stability zone for Green Canyon.

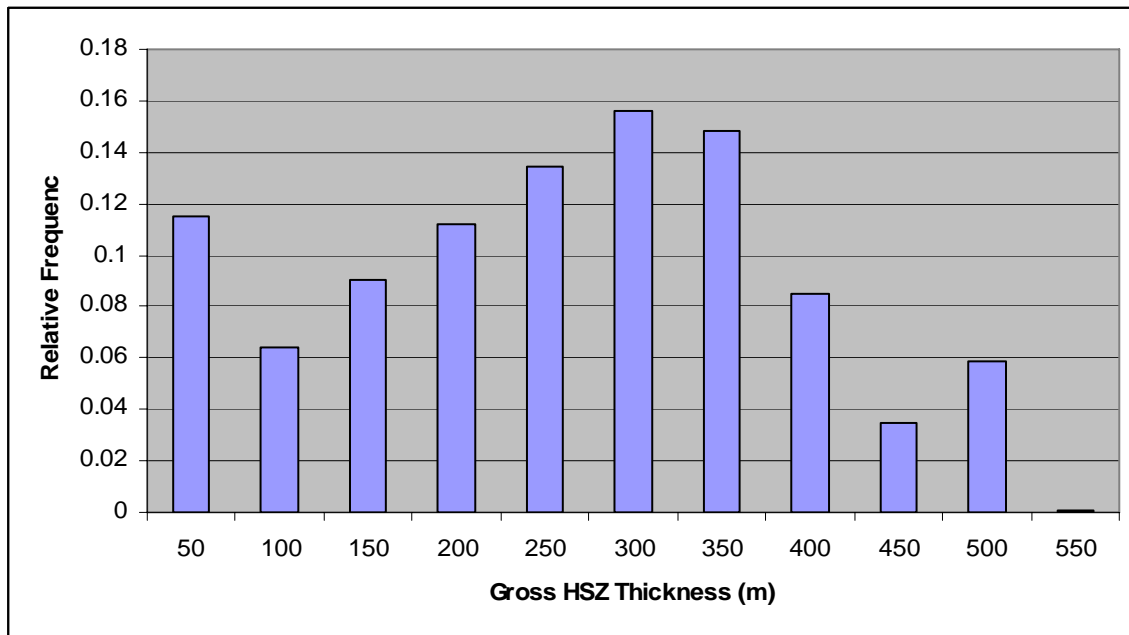
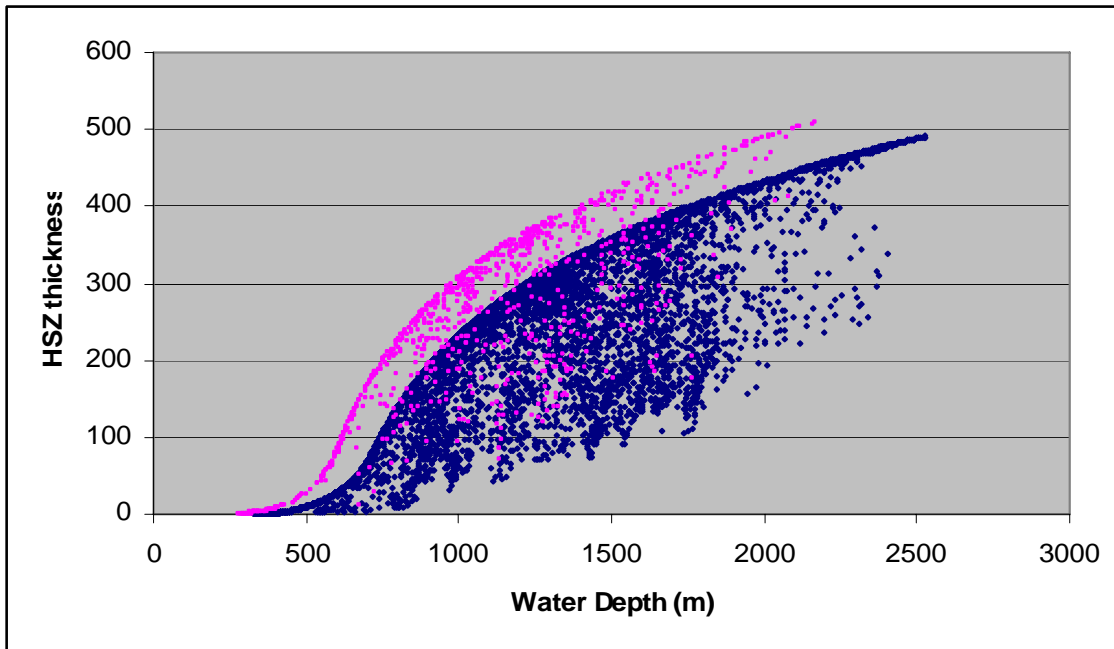


Figure 49. Relative frequency distribution of the mean thickness of the gross HSZ in Green Canyon (mean thickness = 233 meters).





**Figure 50. Mean gross HSZ thickness vs. water depth in Green Canyon. Pink series is from surficial anomaly cells; blue series from non-anomaly cells (units in meters).**

Figure 51 shows the relationship between gross HSZ thickness and (vertical) proximity to salt. Development of gross HSZ thickness is systematically retarded by the proximity of salt, in some cases eliminating the gross HSZ entirely when salt intrudes the pressure/temperature field in which the HSZ could otherwise form. Figure 52 provides a map view of this relationship by comparing isobaths (red lines), contours of depth to top of salt (black lines), and gross HSZ thickness (color fill). The gross HSZ thins over shallow salt intrusions, which, given water depth, would have thicker gross HSZ.

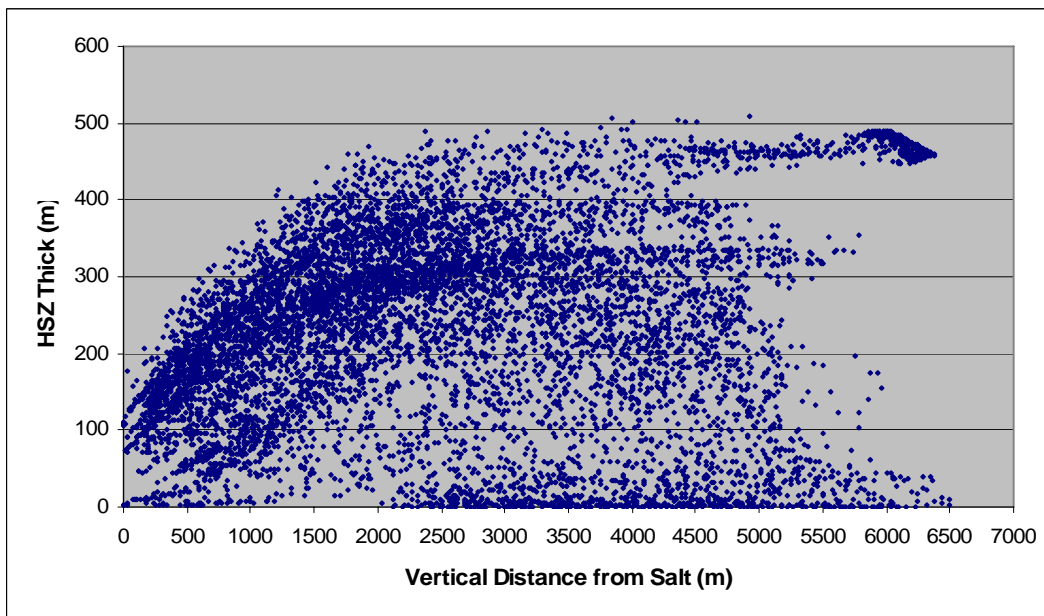


**Figure 51. Mean gross HSZ thickness vs. (vertical) distance from salt in Green Canyon (units in meters).**

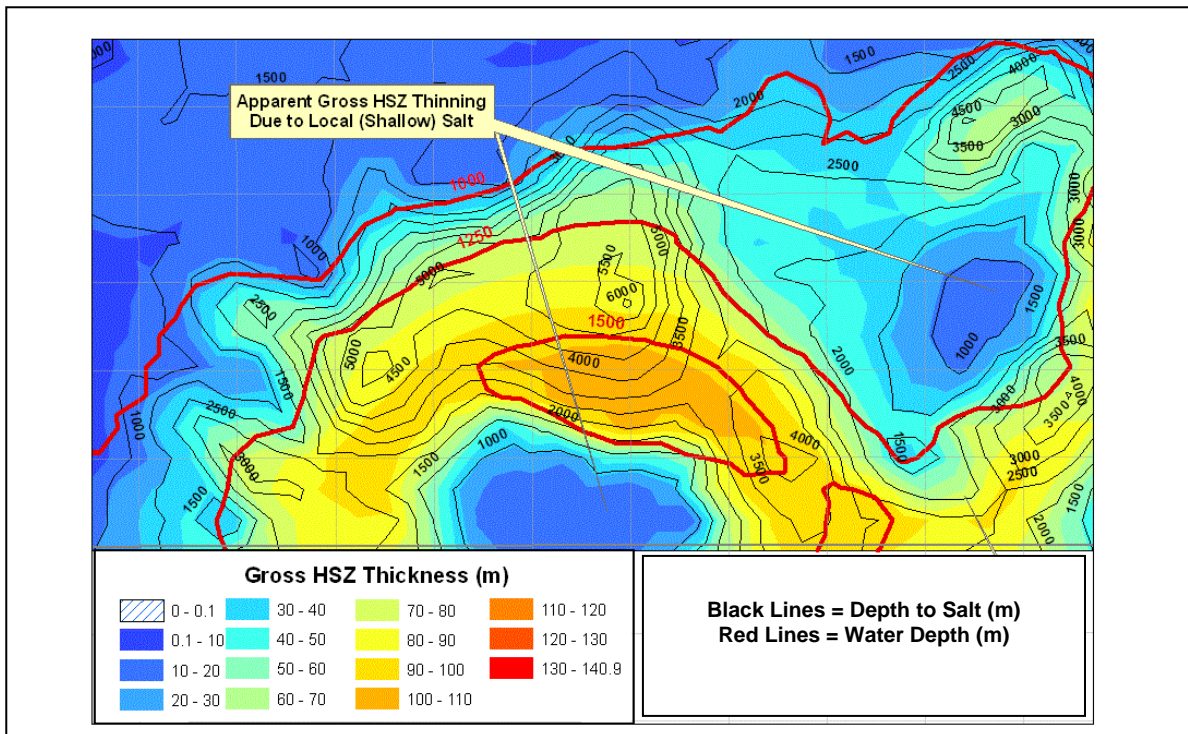


**Figure 52. Influence of shallow local salt (thinning the gross HSZ) exceeding the influence of water depth. Example from the GB study area.**

## B. Estimating the Net Hydrate Stability Zone

These estimates of the gross HSZ thickness take into account pressure, temperature, and salinity. They define the candidate rock volume over which the ambient temperature, pressure, and salinity parameters allow hydrates to form, given void space in the sediment and saturation of methane in formation waters. They do not, however, take into account the influence of activities that extend downward from the seafloor, including the reduced concentration gradient from undersaturated ocean waters and biologic sulfate reduction activity. These processes drive methane concentration below saturation, preventing hydrates from forming. In some cases, this is not for lack of charge, but because “excess” charge from below is being biologically consumed in a process that excludes hydrate formation.

The area of active sulfate reduction by biologic action ranges from zero to roughly 25 m below the seafloor. However, to a depth ranging from 10’s to 100’s of meters beneath the depth of the sulfate reduction zone itself, methane saturation may remain below 100-percent saturation, inhibiting hydrate formation. The vertical thickness from the seafloor downward over which methane saturation is less than 100 percent is referred to here as the *undersaturated zone* (UZ). By eliminating the UZ from the top of the gross HSZ, we estimate the *net* hydrate stability zone.

The method by which we estimate the UZ and, therefore, the net HSZ is described below.

### 1. Estimating the Thickness of the Undersaturated Zone

Our model of the UZ postulates UZ thickness to be inversely proportional to the flux of methane in the shallow section below the seafloor; that is, its thickness is inversely proportional to charge. Where the flux of methane is

so high as to vent to the seafloor (identified in the model by amplitude anomalies on the seafloor surface), the thickness of the UZ is equal to zero. At the other end of the spectrum, where methane flux is lowest (e.g., in the center of the minibasins, which would not receive much, if any, dip-migration-driven gas charge), the UZ is assumed to reach its maximum thickness.

In this analysis, we use the value of methane charge generated by the charge module as input to the model of UZ thickness. This is accomplished in four steps.

- (1) We evaluate the distribution on charge by cell for the entire GOM study area. This yields a description of the distribution, including its mean and fractiles.
- (2) For each cell, there is a mean value of charge from all Monte Carlo trials; the mean charge for a cell is passed from the charge module to the container module.
- (3) The mean charge value for the cell is compared against the GOM-wide distribution to determine the location of the cell mean on the GOM-wide distribution.
- (4) We determine the thickness of the UZ using the algorithm defined below.

Because of outliers in the charge distribution, all cells with mean charge less than the 90-percent (high) fractile of the charge distribution (P90) were assigned UZ thicknesses of zero. All of the cells with mean charge less than the 10-percent (low) fractile of the charge (P10) were assigned a UZ thickness of:

$$(2.9) \quad \text{Undersat} = 220 + (P10 - \text{meanCharge}) \times 30/P10$$

Cells with mean charge between those points were given UZ thicknesses linearly proportionally across the range between the 10- and 90-percent fractiles, i.e.

$$(2.10) \quad \text{Undersat} = ((1 - \text{meanCharge} - P10)/(P90 - P10)) \times 220$$

It is important to note that this calculation was performed using only *the mean charge and not the whole distribution on charge*. This was done for computational speed reasons. The effect of this shortcut was to collapse the variance in the charge data and therefore dampen the total variance propagated through the model. The procedure provided a single estimate of the thickness of the UZ for every cell.

The values relating relative value of methane flux to the thickness of the UZ were provided by Dr. Timothy Collett of the U.S. Geological Survey and Dr. Charlie Paull of the Monterey Bay Aquarium Research Institute (MBARI), and are in accordance with those reported in Paull et al. (2005).

The estimated thickness of the UZ in GC is shown in figure 53; the distribution of the thickness of the UZ by cell is shown in figure 54. The map is generally a reverse image of the charge map (see figure 39).

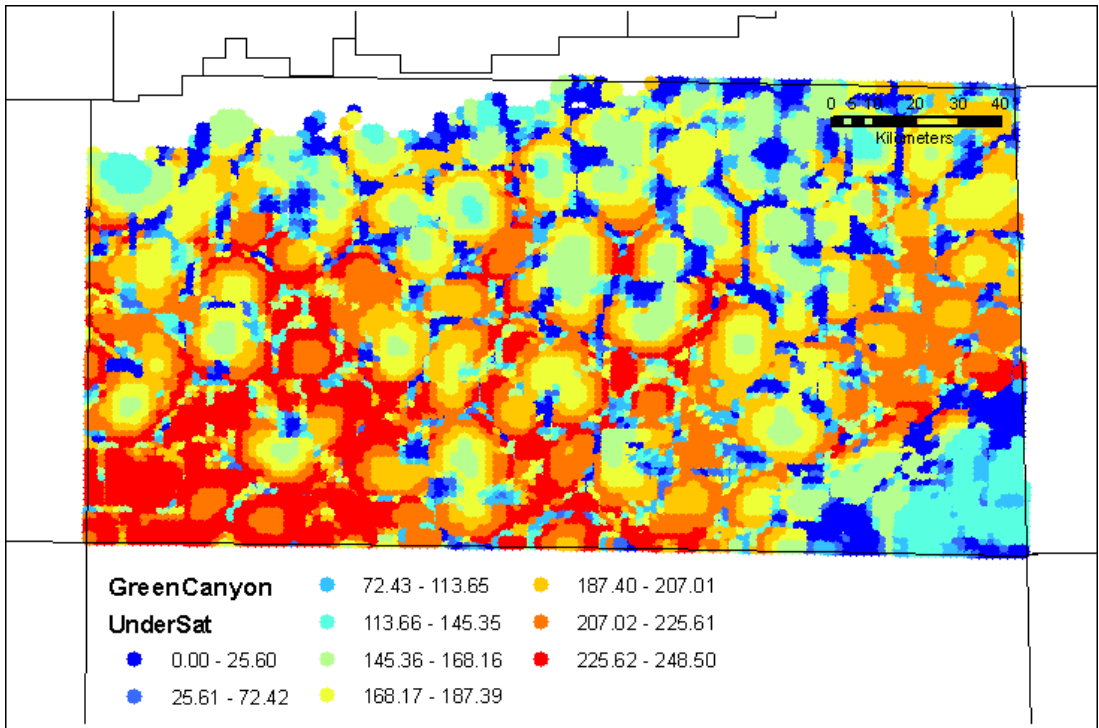


Figure 53. Thickness of the undersaturated zone in Green Canyon (units in meters).

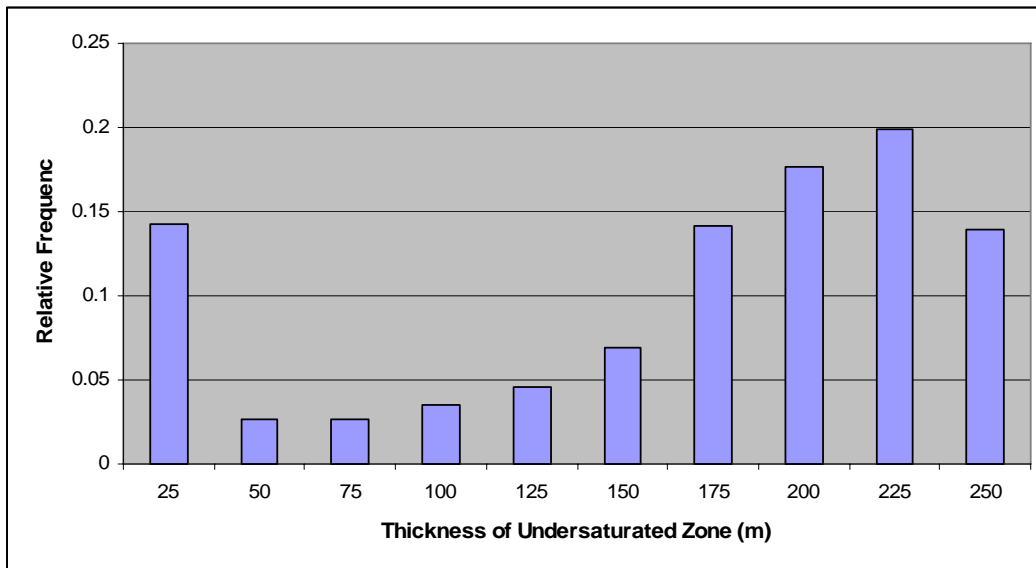


Figure 54. Relative frequency distribution of the thickness of the undersaturated zone in the Green Canyon area (mean thickness = 152 meters).

## 2. Calculating the Thickness of the Net Hydrate Stability Zone

On each Monte Carlo trial for each cell, the value of the UZ is subtracted from the realization of the thickness of the gross HSZ. The difference is the realization, for that trial and cell, of the net thickness of the HSZ. Net HSZ thicknesses are shown in figure 55. The frequency distributions of net HSZ thicknesses appear in figure 56.

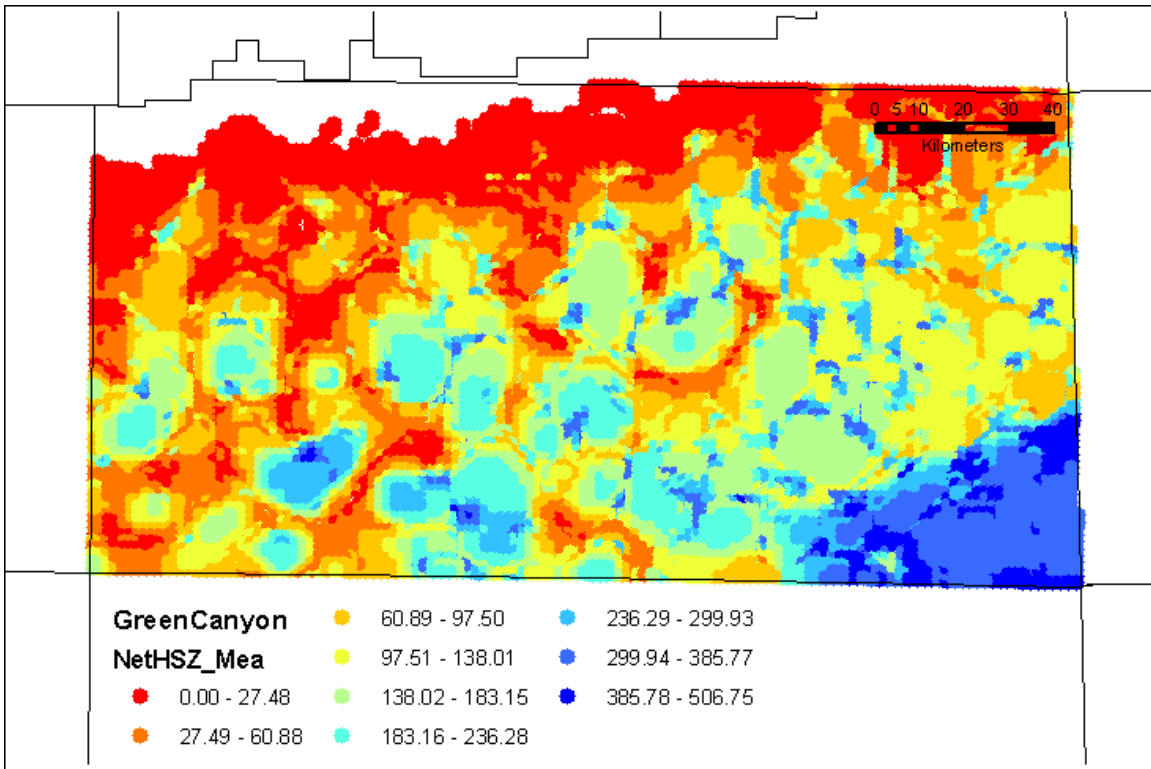


Figure 55. Mean net hydrate stability zone thickness in Green Canyon (units in meters).

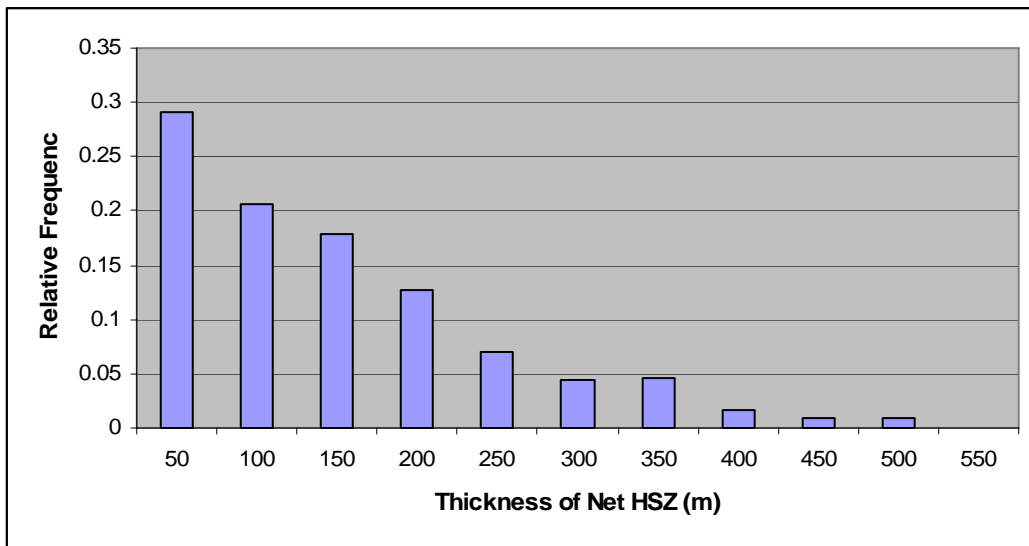


Figure 56. Relative frequency distribution of the thickness of the net hydrate stability zone in the Green Canyon area (mean thickness = 123 meters).

Calculating the distribution of the thickness of the net HSZ for each cell completes the role of the container module. The net HSZ defines the volume of total rock volume that meets the temperature, pressure, salinity, and methane-saturation requirements for the formation of hydrates – conditional on charge and the existence of effective pore space within the net HSZ.

## Concentration Module

The concentration module generates the magnitude of hydrates concentrated in the net HSZ, conditional on charge. That is, if there were no limitation on the volume of methane charge over the total rock volume of the net HSZ in a cell, how much methane would be reservoired in hydrate form? Two calculations must be done. First, calculate the distribution of porosity in the net HSZ; this distribution is a function of lithology and the depth of the midpoint thickness of the net HSZ. Second, calculate the distribution of the fraction of gross pore space occupied by methane hydrates.

### A. Calculation of Matrix Porosity of the Net Hydrate Stability Zone

Shedd and Hunt's mapping of the percent sand in the top 610 m of sediment below the seafloor across the study area provides a point estimate of the sand/shale ratio over the net HSZ in each cell. The gross matrix porosity of the net HSZ is estimated separately for sand and shale. Sand and shale in a cell are then weighted in proportion to the sand/shale ratio in that cell. For both sand and shale, porosity is evaluated at the depth below seafloor of the midpoint depth of the net HSZ. Fracture porosity in the bounds of the surficial seismic anomalies mapped by Shedd and Hunt are calculated separately.

Bulk matrix porosity as a function of depth of burial below the seafloor is modeled separately for sand and for shale. Because of the paucity of empirical data for the GOM fine grain sediments, the shale depth-porosity relationship in Eq. (3.1) is taken from Hamilton (1976). This regression model is adopted as the "pure" shale end member in this approach.

$$(3.1) \quad \text{Porosity} = 0.71 - \frac{0.00081}{(0.0050)} (\text{Depth}) + \frac{0.0000036}{(0.00000015)} (\text{Depth})^2$$

While standard errors of estimates of the three coefficients were available and are shown below the coefficients, a residual error was not reported; however, we determined by trial and error that a normally distributed additive error term with standard deviation 0.015 approximated the error structure reported by Hamilton.

Porosity from shallow sand is estimated from cores taken during the Joint Industry Project coring program at Keathley Canyon Block 151 (KC151). The model is shown below in Eq. (3.2), the parameter estimates in Table 11, and the graph of the fitted function and data are shown in figure 57.

$$(3.2) \quad \text{Porosity} = \text{SSH1} \times \exp(\text{SSH2} \times \text{Depth}(m)) + \text{Error}$$

**Table 11**  
**Parameter Estimates for Eq. (3.2)**

Parameter	Estimate	Std. Error	t-value	Pr(> t )
SSH1	0.5583	2.417e-03	230.98	<2e-16
SSH2	-8.932e-04	1.946e-05	-45.91	<2e-16

The residual standard error for estimation of Eq. (3.2) is 0.05839 on 2,798 degrees of freedom; the distribution of error is assumed to be normal.

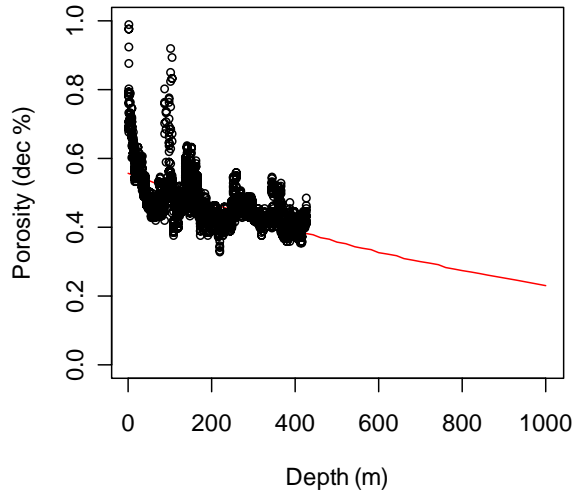


**Figure 57. Sand porosity and depth from KC151 used to estimate sand porosity for determination of void space.**

For each trial and each cell, the realization of the depth of midpoint thickness of the net HSZ is passed from the container module. This is the depth at which the equations for shale and sand porosity (Eqs. (3.1) and (3.2)) are evaluated. These two estimates of porosity represent end member or “pure” shale and sand porosities for the depth of the mid-point thickness of the net HSZ. These two end members’ porosities are averaged and weighted by the sand/shale ratio for the cell, derived from the Shedd-Hunt map of percent sand.

### **B. Calculation of Fracture Porosity in the Net Hydrate Stability Zone**

The team adopted a working assumption that fracture porosity would be a significant host for methane hydrates in areas covered by surficial seismic anomalies. Surficial seismic anomalies are assumed to be associated with either present or paleo venting of methane to the seafloor surface. If the flux of methane is high enough to vent to the surface, it is assumed that flux carried enough energy to create fractures in the sediments in the neighborhood of the vents.

There is no empirical database on the void space created by fractures in vent areas as a fraction of bulk rock volume. Therefore, we relied on a subjective estimate made by Dr. Sassen, who has extensive field experience with vent site samples. Dr. Sassen (*pers. comm.*, 2006) provided a triangular distribution of fracture void volume as a percent of bulk rock volume; this distribution has a minimum of 0 percent, a most likely value of 5 percent and a maximum value of 15 percent.

For cells covered by surficial seismic anomalies, there are two sources of void space in which hydrates can form. One is the matrix porosity in sand and shale facies, in proportion to the sand/shale ratio for the cell and the average porosity given the midpoint depth of the net HSZ. The other is void space created by fractures. These two sources of void space are summed for cells on surficial seismic anomalies. For cells not covered by surficial seismic anomalies, only matrix porosity is included.

### **C. Calculation of Hydrate Saturation as a Fraction of Void Space**

The steps above result in, for each trial and cell, a percent of bulk rock volume of the net HSZ that is occupied by void space. The percent of void space that is occupied by methane hydrates is a function of void-space type and lithology; this is hydrate saturation. Hydrate saturation is estimated separately for sand, shale, and fractured “reservoirs”.

The data to estimate the distributions of the shale and the sand matrices were furnished by Dr. Tim Collett, USGS. Data and summary statistics are presented in Table 12.

**Table 12**  
**Wells Used in the Analysis of Distributions of Shale and Sand Matrices and Associated Summary Statistics**

Type	Site	Well	Water Saturation (fraction)							Number of Observations
			Min.	1 <sup>st</sup> Qu.	Median.	Mean	3 <sup>rd</sup> Qu.	Max.	Std. Dev.	
Shale	Atwater	JIP-AT13	0.699	0.960	1.000	0.973	1.000	1.000	0.049	1,073
Shale	Atwater	JIP-AT14	0.864	0.953	0.984	0.973	1.000	1.000	0.031	653
Shale	Blake Ridge	BR-994	0.775	0.935	0.948	0.942	0.960	1.000	0.033	1,417
Shale	Blake Ridge	BR-995	0.788	0.927	0.940	0.936	0.954	1.000	0.033	1,686
Shale	Hydrate Ridge	HR1247	0.805	0.972	1.000	0.980	1.000	1.000	0.035	598
Shale	Hydrate Ridge	HR1248	0.819	0.942	0.975	0.963	1.000	1.000	0.040	591
Shale	Hydrate Ridge	HR1251	0.851	0.989	1.000	0.986	1.000	1.000	0.030	1,109
Sand	Mallik	M5138	0.373	0.644	0.731	0.708	0.791	0.888	0.113	302

The shale intervals in the Atwater, Hydrate Ridge, and Blake Ridge wells contain some influence of fractures; the saturation values from these sites were integrated in the study as shale reservoirs in an effort to capture the influence of (possibly widespread) fractures on gas hydrate saturation values in shales. There was reasonable agreement among distributional forms for all of the shale wells. After preliminary analysis, the combined dataset of BR-994 and BR-995 was used as the basis of the shale matrix model (see figure 58).

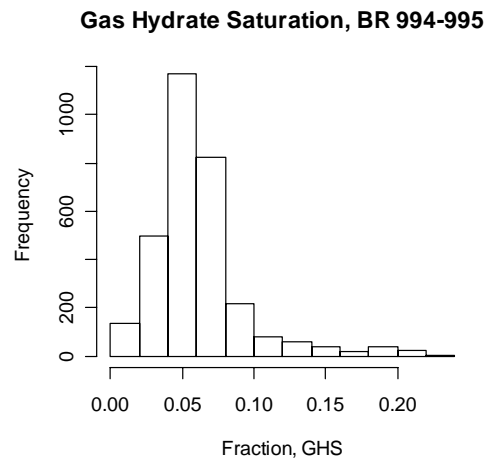


**Figure 58. Histogram of the combined BR-994 and BR-995 gas hydrate saturation (1 - water saturation).**

This distribution is nearly symmetric in the range 0 to 0.10 and then has a long right tail, which declines linearly from 0.10 to the maximum value of 0.225. Unfortunately, this distribution could not be accurately fit to a standard distributional form. Because of prior model limitations in specifying a more complex distribution, a triangular distribution with minimum, mode, and maximum of 0.0, 0.10, and 0.20 was specified. Subsequent model implementations will reflect a closer fit to the empirical data.

Hydrate saturation values in a sand matrix were based upon a distribution fitted to the Mallik M5L38 well (figure 59).



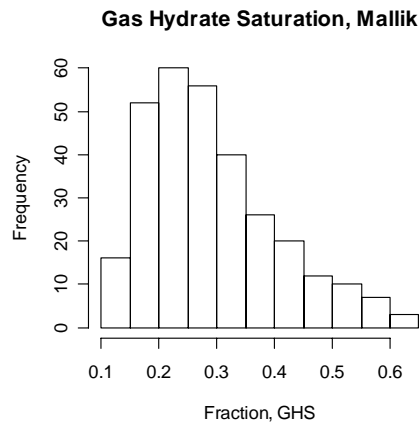


**Figure 59. Histogram of the fraction of gas hydrate saturation, Mallik M5L38 well**

Gas hydrate saturation in sands was modeled using a Beta distribution as  $Y = 0.11 + 0.52 * \text{Beta}(1.588, 3.604)$ , where the range of the Beta is 0 to 1. Because Mallik M5L38 is not pure sand, its distribution was modified, and a triangular distribution of the form (0.40, 0.60, 0.90) was developed. We expect that future model runs will include additional sand saturation values captured from a number of current or recent gas hydrate drilling programs.

The saturation of fracture void space in sands and shales also enters the model as a triangular distribution (0.70, 0.80, 0.90). Because very little empirical data exist, this distribution is based on expert judgment provided by Dr. Roger Sassen of Texas A & M University.

The three triangular distributions in Table 13 are assumed to be mutually independent.

**Table 13  
Distributions on Percent Hydrate Saturation of by Type of Void Space**

Void Space	Minimum	Most Likely	Maximum
Shale matrix	0	10	20
Sand matrix	40	60	90
Fractures (sand and shale)	70	80	90

#### **D. Estimation of Hydrate Concentration in the Net Hydrate Stability Zone**

Distributions of average matrix porosity and fracture void space (for anomaly cells) are combined via Monte Carloing to form a composite distribution of the percentage of the net HSZ bulk rock volume constituted by void space – available for hydrate formation. At each trial the total void space percentage for a cell, by type, is multiplied by a Monte Carloed value of saturation to create an empirical distribution of total volume available for charging in the net HSZ in each cell.

Monte Carloed mean concentrations in GC study area are shown in figure 60. The empirical distribution of percent concentration (as a percent of bulk rock volume) appears in figure 61.

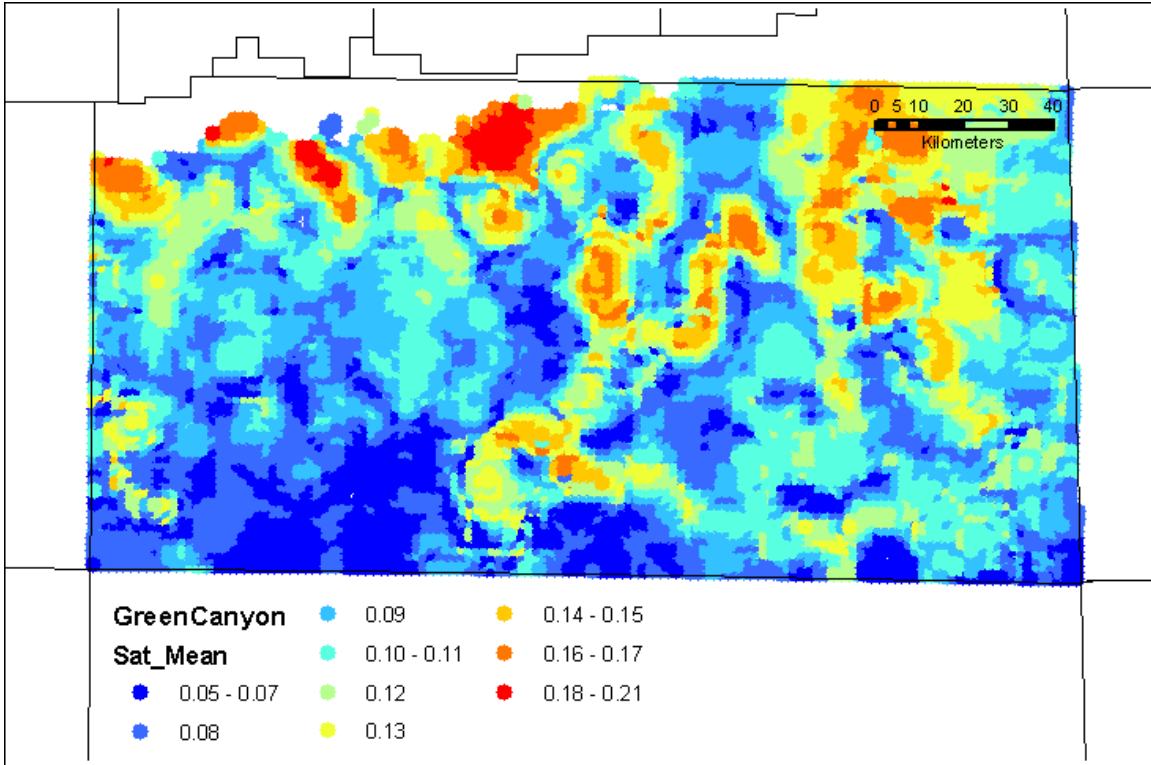


Figure 60. Hydrate concentration as a decimal percent of bulk sediment volume of the net HSZ in the Green Canyon study area.

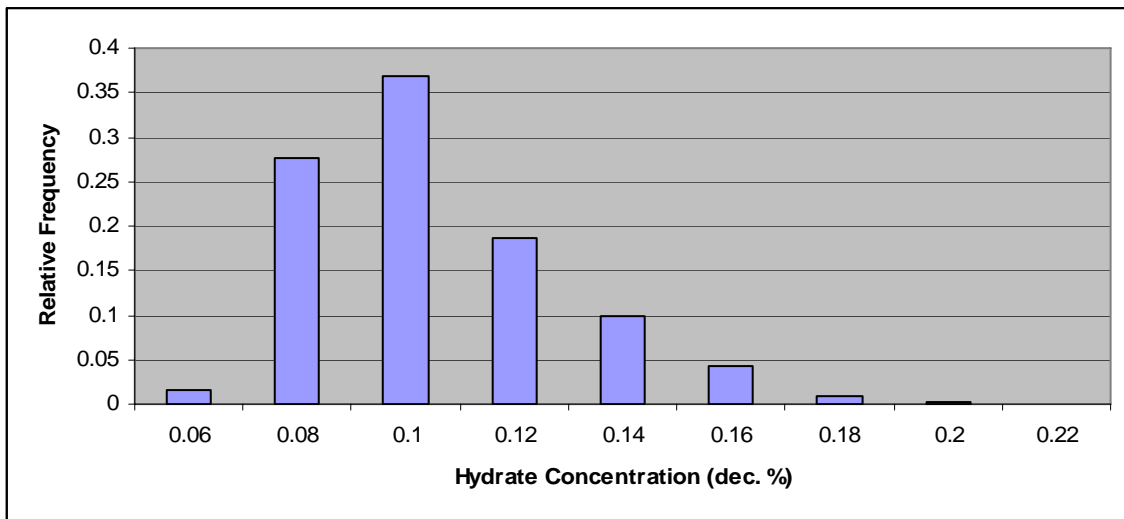


Figure 61. Relative frequency distribution of the hydrate concentration as a decimal percent of bulk sediment volume in the net HSZ, Green Canyon area (mean = 0.095).

## **Integration Module**

The final step in the analysis is relatively simple: at each Monte Carlo trial, the volume of in-place methane hydrates in a cell cannot exceed the accommodation space available in the net HSZ in that cell, so we set in-place methane hydrates equal to the minimum of the volume of charge and the volume of the accommodation space. Repetition of this comparison over a large number of trials produces an empirical frequency distribution of in-place methane hydrates in each cell, under reservoir temperature and pressure conditions. These volumes are then converted to standard temperature and pressure (STP) and reported using that convention. Finally, volumes of in-place hydrates in individual cells are aggregated to provide frequency distributions for larger geographic aggregates ranging from MMS protraction areas to the entire GOM study area.

### **A. Estimation of In-Place Hydrates at Reservoir Temperature and Pressure**

As we have adopted a mass balance approach in this assessment, the final step is a comparison of the mass (volume) of methane available to charge a cell with hydrates and the volume of effective void space available in which they can form. The final volume of in-place hydrates equals the smaller of those two values. For all cells, if the thickness of the net HSZ on a trial is equal to zero, a zero hydrate volume is assigned to the cell for that trial.

Cells covered by surficial seismic anomalies are treated differently from the majority of cells which are not covered by anomalies. On each trial, the charge module provides a volume of gas available to charge the net HSZ in each off-anomaly cell. The thickness of the net HSZ (produced by the container module) is multiplied by the percent of bulk net HSZ volume that can be filled with hydrates (produced by the concentration module) to yield a total volume of methane available to host hydrates.

If the volume of charge is greater than the volume available to accommodate hydrates, the accommodation volume is retained as hydrates in-place for that trial. If the volume of charge is less than the volume available to accommodate hydrates, the charge volume is retained as the in-place volume of hydrates.

However, for cells covered by surficial seismic anomalies, no comparison is made. It is assumed that if the volume of the charge is or has been enough to vent methane to the seafloor surface, there is enough charge volume to fill the available effective void space to its calculated capacity. In instances where the modeled charge does not fill the HSZ, the available void space is manually filled to capacity.

### **B. Conversion of In-Place Hydrate Volumes to Standard Temperature and Pressure**

Once the volume of hydrates in place at reservoir temperatures and pressures is determined, it must be converted to volume at STP. This conversion accommodates the effect of the changes of gas temperature and pressure on gas volume, the deviation of the gas from ideal, and the range of clathrate cage occupancy.

The conversion factor (equivalent to the formation volume factor in conventional petroleum engineering calculations) is a highly uncertain quantity, and there is no empirical data available to support assignment of a probability distribution to it. We use a subjective probability distribution provided by Dr. Collett (see figure 62):

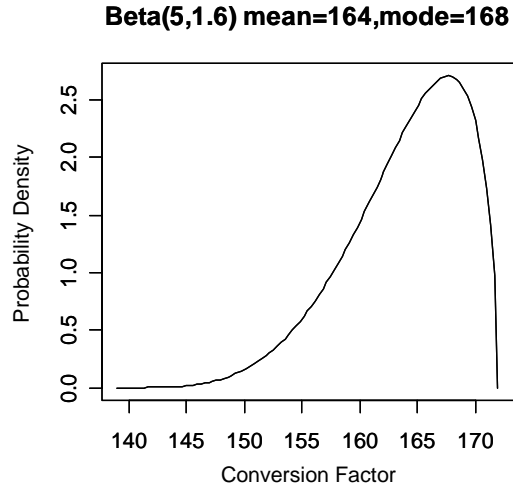


**Figure 62. Probability distribution of conversion factor to STP.**

A map of methane hydrate volumes in place, at STP for the GC protraction area, is shown in figure 63. The relative frequency distribution of cell volumes is shown in figure 64. A hydrate volume in place map for the entire GOM is presented in Chapter IV (Results).

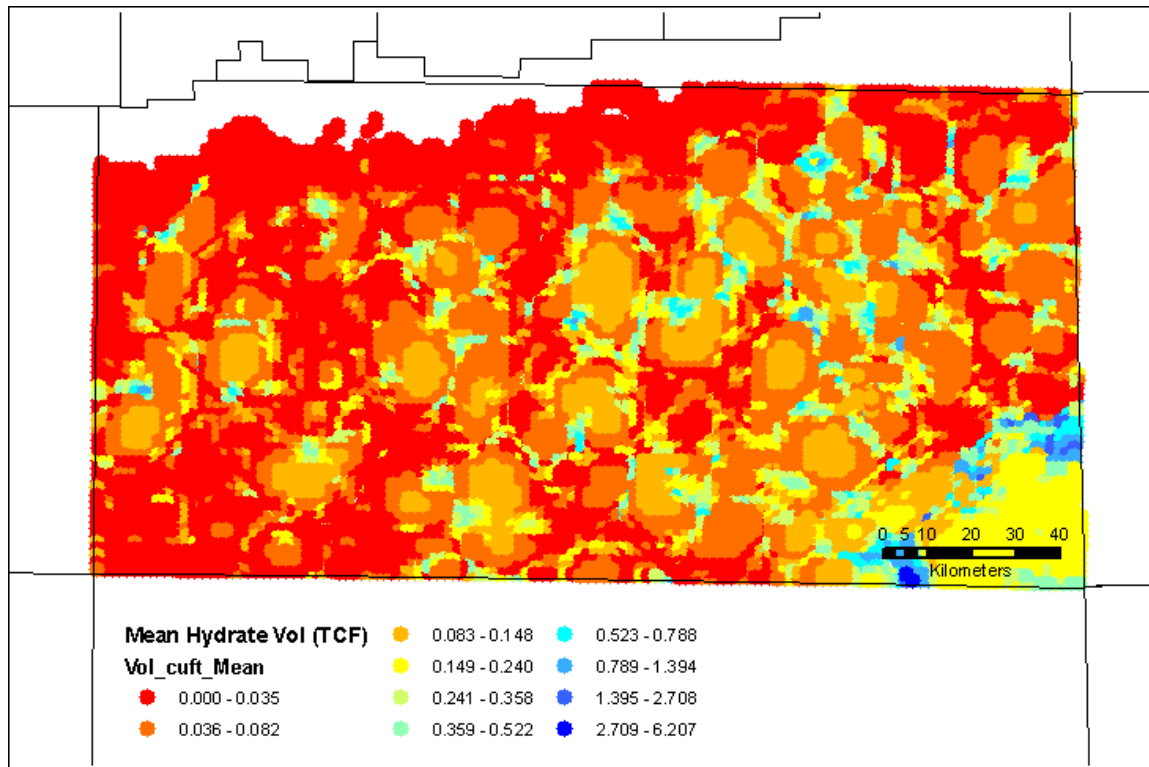


**Figure 63. Distribution of mean gas hydrate volume at STP in Green Canyon (values listed in trillion cubic feet).**

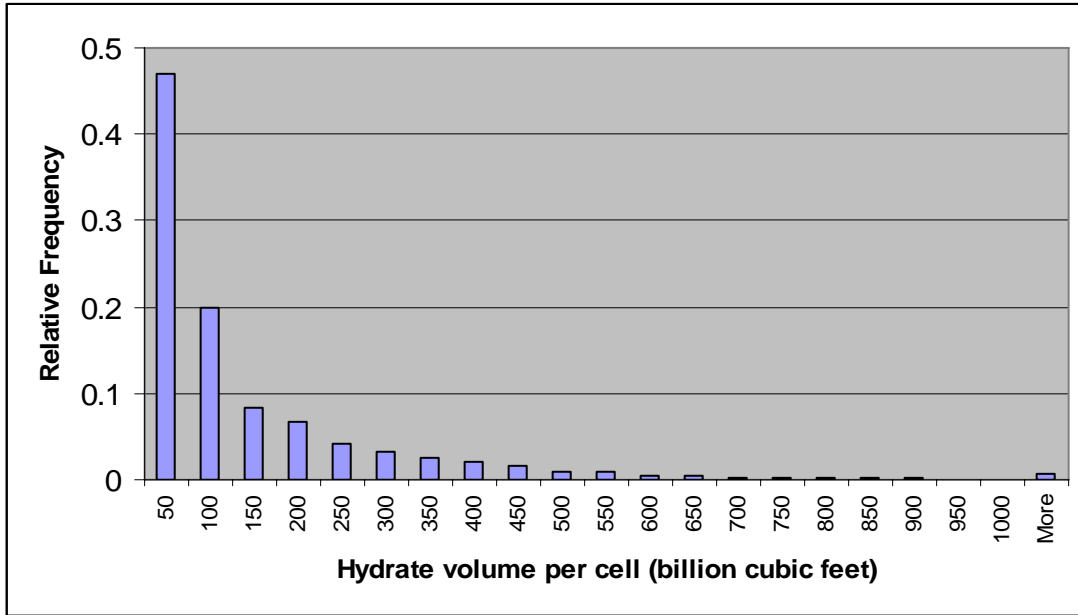


**Figure 64: Relative frequency distribution of mean in-place gas hydrate volume in Green Canyon (values in BCF per model cell). Mean value = 120.85 BCF in GC.**

**C. Aggregation of Cell Results to Larger Geographic Aggregates**

There are 202,079 cells within 1,155 basins in the GOM study area; the cells are stochastically independent. However, the only structurally induced dependencies appear in the migration module because methane generation is redistributed as a function of percent cell convexity within a catchment area. Subsequently there are no dependencies across cells.

The aggregate distribution of cell results for the GOM is computed by summing the volumes by trial across all cells. Let  $V_{ij}$  be the volume in cell  $j$  for the  $i^{\text{th}}$  trial. Then the volume  $V_i$  for the  $i^{\text{th}}$  trial is simply,  $V_i = \sum_{j=1}^{NC} V_{ij}$ , where NC is the number of cells.

The empirical distribution of aggregate volume in the entire GOM is constructed from the set  $\{V_i, i = 1, \dots, 1,000\}$  of 1,000 Monte Carloed aggregate volumes. The same procedure can be used to aggregate smaller regions such as Green Canyon.



### Chapter III. Underlying Geologic Data, Analysis, and Framework

The foundation for the in-place hydrate assessment for the Gulf of Mexico (GOM) rests on an empirical framework of geological and geophysical data and interpretations. These input data were developed over several years by MMS-GOMR personnel including Bill Shedd, Jesse Hunt, and Scott Edwards, using primarily the MMS proprietary database. In this chapter, the interpretive workflow is presented for each input and the criteria for the sometimes subjective nature of the interpretation are described. Detailed descriptions of the applicability of each input parameter to the methodology and model structure can be found in Chapter II (Methodology).

The four input data sets fundamental to the study include:

- (1) Seafloor bathymetry
- (2) Surficial seismic anomalies
- (3) Top salt depth
- (4) Areal sand distribution

The geophysical data used in this study consists of 154 individual time-migrated 3-D seismic volumes covering approximately 200,000 km<sup>2</sup> across the upper and lower slopes of the GOM. Approximately 225,000 km<sup>2</sup> of time-migrated 2-D seismic data were used in areas where 3-D coverage was absent, including the Florida platform and some ultra-deepwater areas (see figure 65). Limited deepwater areas in the southeastern part of the study area are void of any seismic data coverage and have not been included in this study. All interpretations were made on the best-available time-migrated data for any given area, with depth-migrated seismic data used only to validate and verify interpretations in areas of complex salt tectonic activity.

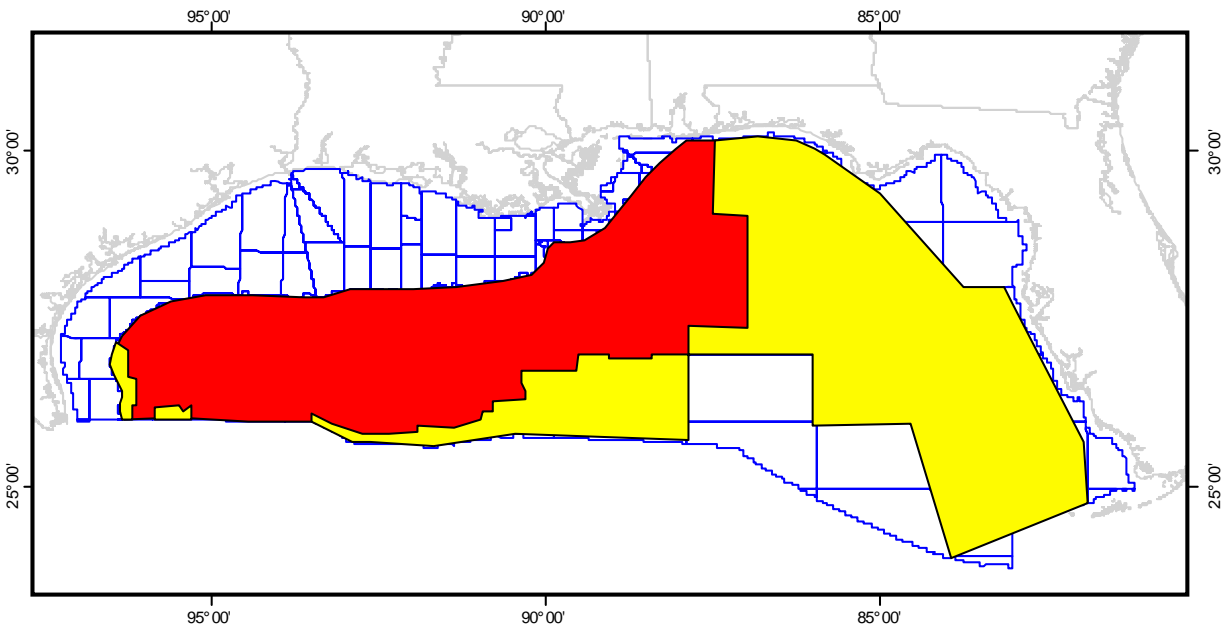


**Figure 65. Seismic data coverage available for the hydrate assessment. Red area indicates 3-D data coverage; yellow area indicates 2-D data coverage. Uncolored areas were either void of seismic data coverage or did not meet the water-depth criteria.**

## Seafloor Bathymetry

The seafloor bathymetry interpretation of the GOM is a critical input parameter for both the HSZ thickness module and the charge module. Bathymetric variations influence the thickness of the HSZ through the associated changes in temperature and pressure conditions. In order to accurately predict the methanogenic rates that drive the charge module, initial seafloor temperature is combined with a geothermal gradient to provide an estimate of sediment temperature at a given depth. In addition, the bathymetry interpretation is used foundationally to calculate two other input parameters: distribution of surficial seismic anomalies and depth to top salt.

The objective of the seafloor bathymetry mapping project was to establish a cohesive interpretation of the seafloor depth across the GOM basin. The seafloor horizon was interpreted in each time-migrated seismic survey as the first strong peak event, representing the positive acoustic impedance contrast between the water column and the subsurface. This seafloor interpretation was made with a very high degree of confidence for several reasons, including the relatively uniform velocity of the overlying water column and the relatively high frequency of the seismic signal.

A varying number of seed lines were interpreted for each survey, depending on the complexity of the seafloor geometry and the highly variable amplitude response. Aside from some high dip and structurally-complex areas that needed extensive manual interpretation, an automatic picking algorithm was utilized to generate an interpretation across the full volume of each 3-D survey. All available lines on the 2-D seismic data were interpreted and processed with a simple gridding algorithm to provide complete coverage (see figure 66).

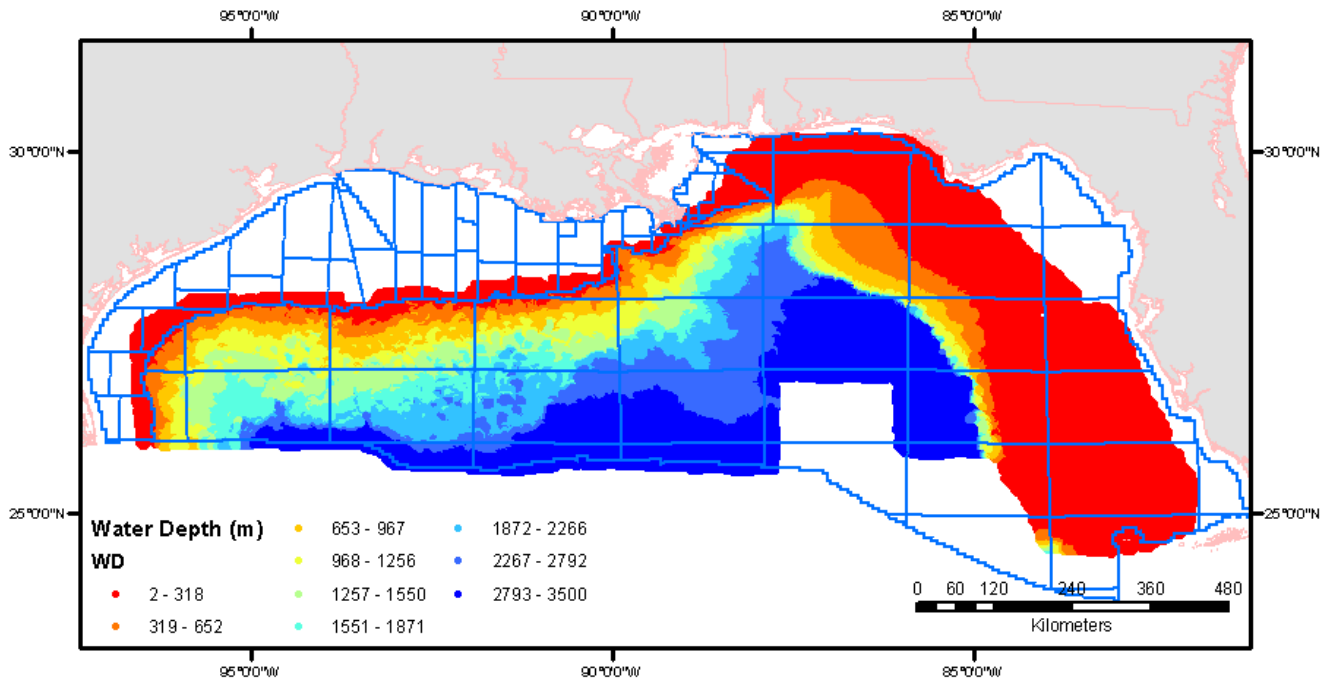


**Figure 66. Seafloor bathymetry across the study area (depth in meters).**

The seafloor measurement was converted from two-way travel time to subsea depth by assuming a water column velocity of 1487.4 meters/second (4880 ft/sec). Each of the 202,079 cells in the study area was assigned a single value for water depth.



## Surficial Seismic Anomalies

A seafloor amplitude anomaly is an extracted component of the seismic data that measures the type of acoustic response (positive/negative) and the intensity of the response, expressed in relation to the background seismic response (see figure 67). Typically, these anomalies are found where the seafloor substrate comprises something other than the typical soft mud and silt found across the majority of the GOM. This study has documented the abundance of these anomalies across the deepwater GOM (see figure 68). The anomalies often coincide with active or paleo-vents of methane to the seafloor, which themselves tend to be coincident with basin margins and shallow fault systems. The location and size of these anomalies are important input parameters that were incorporated into the charge module, where they serve as a direct hydrocarbon indicator for the shallow section and allow for the HSZ to be manually filled to capacity.

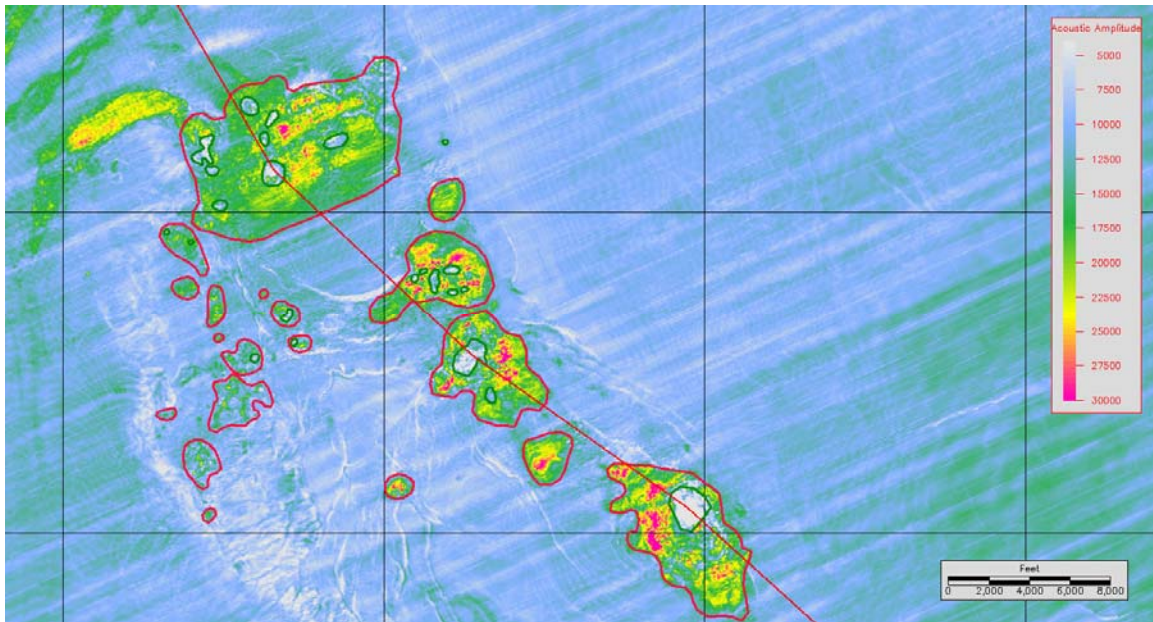


**Figure 67. Amplitude extraction of the seafloor in the Gulf of Mexico. Strong positive amplitude anomalies, interpreted to represent hydrate, hard grounds, and chemosynthetic communities, are outlined by red polygons. Green polygons indicate weak positive and negative anomalies, interpreted to be high-flux vent sites.**

The objective of the seafloor seismic anomaly mapping project was to extract the amplitude from the previously defined bathymetric depth map. Due to time and data storage constraints, the seafloor amplitude interpretations were not normalized among all seismic surveys. As such, potential anomalies were identified using a subjective process separating the anomalous zones from the background response, rather than a quantitative measure of absolute amplitude.

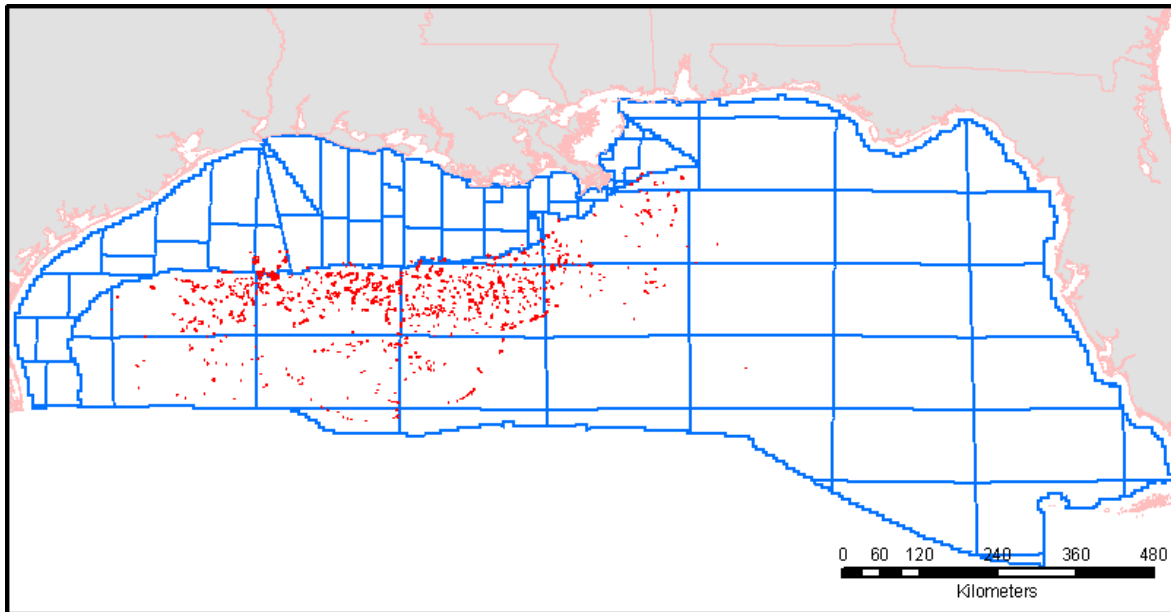


**Figure 68. Location of all deepwater seafloor anomalies identified in the Gulf of Mexico.**

The high positive amplitude responses were outlined and interpreted as areas with extensive authigenic carbonates, hydrates, and chemosynthetic communities, all of which are believed to be associated with active venting of methane at the seafloor (see figure 69). An anomalously strong positive reflection coefficient would be expected at each of these seafloor environments. Those areas with low positive responses or negative responses (phase reversals from peak to trough), often embedded within the high positive areas, were interpreted as areas of very high flux rates with gas saturated muds. The velocity of the water column is often greater than that of this seafloor environment, resulting in a weak positive to negative reflection coefficient. Mud volcanoes, with rapid but intermittent flux rates often displaying weak amplitude response, but characteristic conical shapes on the time display and seismic cross-sections, were also identified.

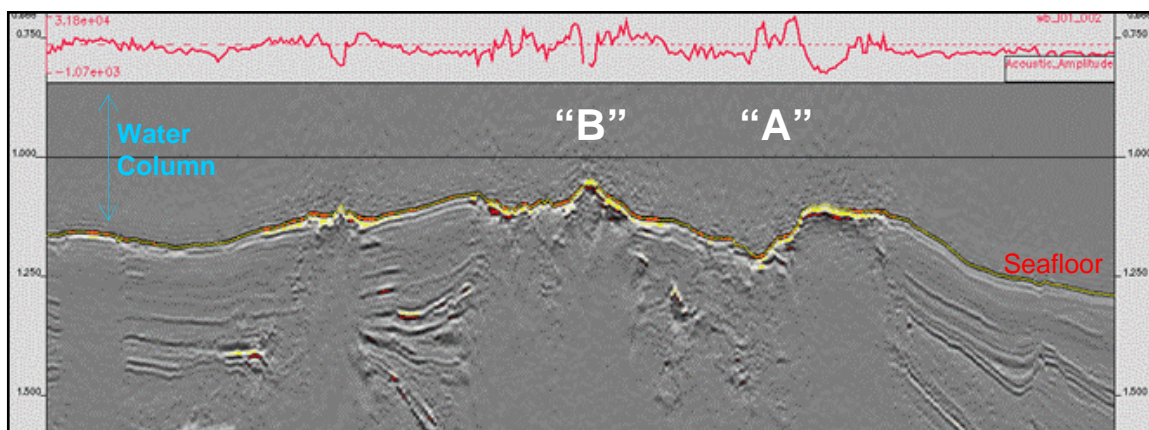


**Figure 69. Seismic section with depth units in two-way time (one second of water = 743.7 meters). Event “A” identifies a high positive amplitude response on the seafloor, interpreted to be a hard ground feature. Event “B” identifies a negative response, interpreted to be a methane-rich vent site.**

Amplitude anomalies that did not show direct evidence of seepage on the seismic cross-sections were not outlined. These areas were identified as either sediment flows from active seeps nearby, turbidite flows of sand-rich sediment over hemiplegic mud, or exposure of salt or dense saline brines on the seafloor.

The surficial seismic anomalies, and the associated high flux of methane interpreted to accompany them, serve as a direct indicator of methane gas in the shallow subsurface and on the seafloor. As such, the areal extent of the anomalies is used as a proxy to identify areas in the GOM where the gas hydrate stability zone should theoretically be filled to capacity. This is also described in the container module section of Chapter II (Methodology).

The amplitude anomalies are of varying shapes and sizes that depict the actual spatial distribution on the seafloor. As a result, when the anomalies were first applied to the GOM in-place hydrate model to measure the spatial impact, only 15 percent (700 of 4,700) of the anomalies intersected the middle of a grid cell (a cell measures 5,000 feet by 5,000 feet; 2.32 km<sup>2</sup>). Believing that these anomalies are spatially-significant hydrocarbon indicators that are not recognized by the model as such, the MMS geoscientists added a 762-m (2,500-ft) buffer to the perimeter of each anomaly (see figure 70). The result is evident: the same 4,700 anomalies are now intersected on nearly 3,700 occasions. This provides an acceptable level of anomaly recognition and a quantifiable impact on the in-place resources.

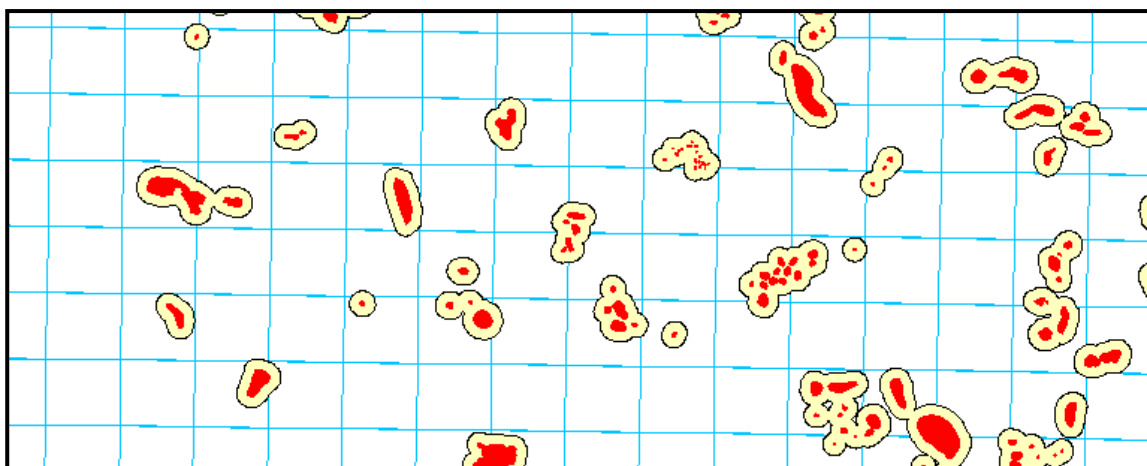


**Figure 70. Sub-regional example of surficial amplitude anomaly polygons (solid red) and the 762-m buffer (yellow) installed for better representation of the anomalies with respect to the model's cellular structure. Light blue squares are OCS blocks measuring 5760 acres.**

### **Top of Salt (Basement)**

The depth from the seafloor to the top of salt in the GOM is an important input parameter for two modules: the charge module and the HSZ thickness module. For the charge module, the top of salt serves two primary functions. First, it is interpreted to serve as the base of the Neogene sedimentary section that is available to contribute to the generation of biogenic methane. Second, in areas where allochthonous salt is emplaced near the seafloor, the top of salt geometry is used to define migration flow direction. This geometry ultimately controls the shape of the catchment basins and the distribution of the dip-migrated methane gas. The presence or absence of shallow salt is also a critical component in the calculation of the HSZ thickness in the container module. Salt influences the thickness of the HSZ by raising both local sediment temperatures and pore water salinities.

The objective of the top of salt mapping project was to establish a continuous interpretive surface at the top of salt (or similar correlative surface) across the entire GOM study area. The dataset used for the top of salt interpretation consists of the same 2-D and 3-D time-migrated seismic volumes that were used for the

bathymetric interpretation. Shallow and deep salt bodies were subjectively identified in the GOM using a series of predictable characteristics, including: the presence of a strong seismic peak on the top of the salt body, resulting from a positive impedance contrast between the overlying sedimentary unit and the salt; a homogenous appearance and shape that is often in sharp contrast with the surrounding rock; and evidence of cohesive mobility and influence on the adjoining sedimentary section that results in deformed beds and angular contacts. In areas where multiple salt bodies exist, only the shallowest feature was interpreted. Depth to the top of salt (or basement) ranges from several meters below the seafloor on the slope to several thousand meters on the abyssal plain (see figure 71).

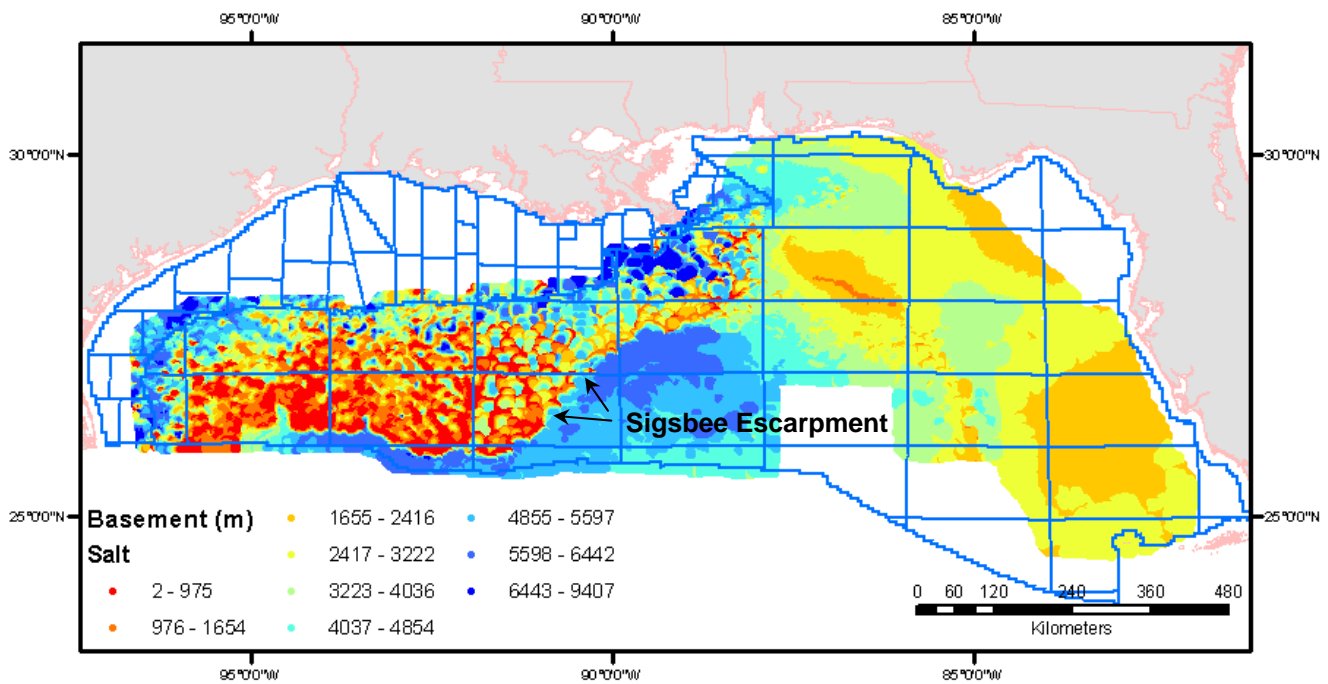


**Figure 71. Subseafloor depth to top of salt (or basement) in meters. The Sigsbee Escarpment represents the southern extent of shallow salt in the GOM basin. Dark blue colors in the upper slope indicate deep mini-basins.**

To avoid null values, the top salt surface was mapped to all points across the GOM. In many parts of the GOM, especially near the middle of most minibasins on the upper slope, all shallow salt has been evacuated, and only a welded surface remains. Salt welds are identified by many of the same features as a salt body, including prominently strong positive seismic reflectors accompanied by discordant beds below and downlapping bedding features above. For the purpose of the hydrate assessment, a salt weld is mapped in a similar fashion and serves the same purpose as the top of salt.

Identifying a continuous top of salt surface in areas south and east of the Sigsbee Escarpment is not possible because of the periodic absence of either depositional or emplaced salt (see figure 72). In this environment, shallow salt bodies are rarely found, but deep salt features are sometimes identifiable at the autochthonous level, meaning that they have remained in the same relative stratigraphic position as when deposited in the Callovian Stage of the Jurassic. In cases where neither shallow nor deep salt can be identified, the top of salt surface is interpreted along the top of the basement structure. The top of basement is interpreted to be the relative chronostratigraphic equivalent of the autochthonous Louann Salt. The basement is identified seismically by a strong reflector at the base of the deepest bedded feature in the basin and by relative stratigraphic position defined by biostratigraphic well control.



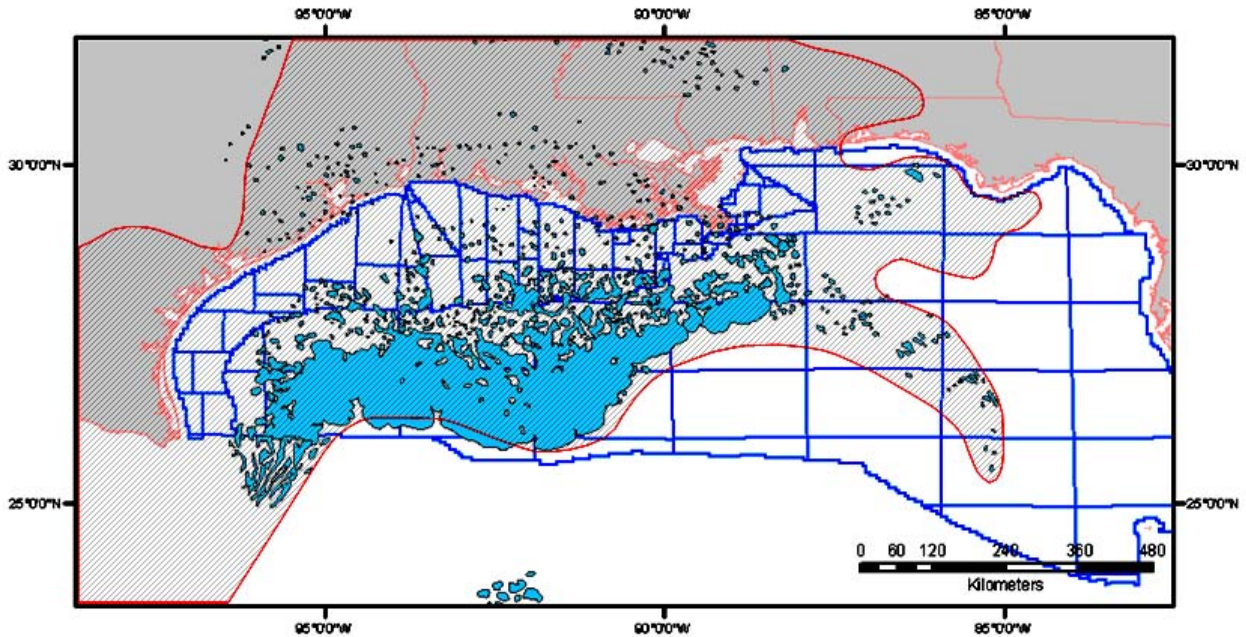


**Figure 72. Gulf of Mexico basin map showing present day allochthonous salt (light blue) and depositional limit of autochthonous salt (hatched area). Note that neither of the two is present in the southeastern part of the study area (Simmons, 1992; Pindell and others, 2000).**

The combined interpretation of shallow allochthonous salt bodies, mid-level salt welds, deep autochthonous salt features, and basement structure provides a single contiguous interpretation across the GOM with a depth unit of two-way time (milliseconds). This surface must then be converted into two products: an isopach of the water bottom to the top of salt (thickness), and a top of salt structure (depth). The isopach is calculated by applying a uniform sediment velocity of 1,841 meters/second (6,040 ft/s) to the isochronal interval from water bottom to top of salt. While we recognize that this uniform velocity represents an unlikely state in nature, no attempt was made to account for the assumed increase in sediment velocity with depth. The top of salt depth structure is calculated by summing the isopach thickness with the previously-calculated water bottom depth structure.

### **Sand Distribution**

The areal distribution and vertical concentration of sand and shale volumes in the GOM are important input parameters in both the charge and concentration modules of the in-place assessment model. In the charge module, the relationship between water flux in the source rock and methanogenic productivity is presumed to be direct. We invoke the end member physical properties of sands and shales to model water flux (using permeability as a variable) and apply them through the candidate section using the sand/shale ratio defined here. The sand and shale content of the HSZ is used to define the distribution of porosity and the saturation of available pore space in the concentration module.

In the future, the distribution of sand will be needed to satisfy the working assumption that, initially on the OCS, gas hydrate will only be technically and economically recovered from sandy reservoirs. The relatively high porosity and permeability found in sands within the HSZ is essential to the accumulation of gas hydrate in high concentrations and the ability to flow the dissociated gas during the production process.

The objective of the sand count project was to quantitatively define the sand component in the HSZ using the empirical database of the MMS GOMR. The HSZ was assumed (1) to include no more than the first 610 m (2000 ft.) of section immediately below the mudline, and (2) to not exist in water depths less than 200 m. While we do recognize modeled HSZ thicknesses greater than 610 m in the GOM, the depth cutoff for the sand count was selected to provide a meaningful sample thickness.

Over a period of nearly two calendar years (2005 - 2006), all wells in the GOM located in greater than 200 m of water were evaluated to determine if they contained log suites in the upper 610 meters (2000 ft) of section. In general, most of the recent wells had logging while drilling data with 500 m or more of available logged section, while many of the older wireline logs covered 500 meters or less of available section. Wells that contained logs with less than 300 m of available section were not used in this study. Only one well per deepwater platform was included in the study, regardless of availability.

Based on the criteria outlined above, 841 wells were selected for lithologic analysis (see figure 73). The gamma ray log curve was used to identify a shale baseline, and individual sand body thicknesses were recorded where the gamma ray fell below the baseline. For each well, the sand body thicknesses are summed and then divided by the total log thickness evaluated, generating a percent-sand value in the shallow section. These 841 values served as hard data points and were geographically referenced (latitude, longitude).

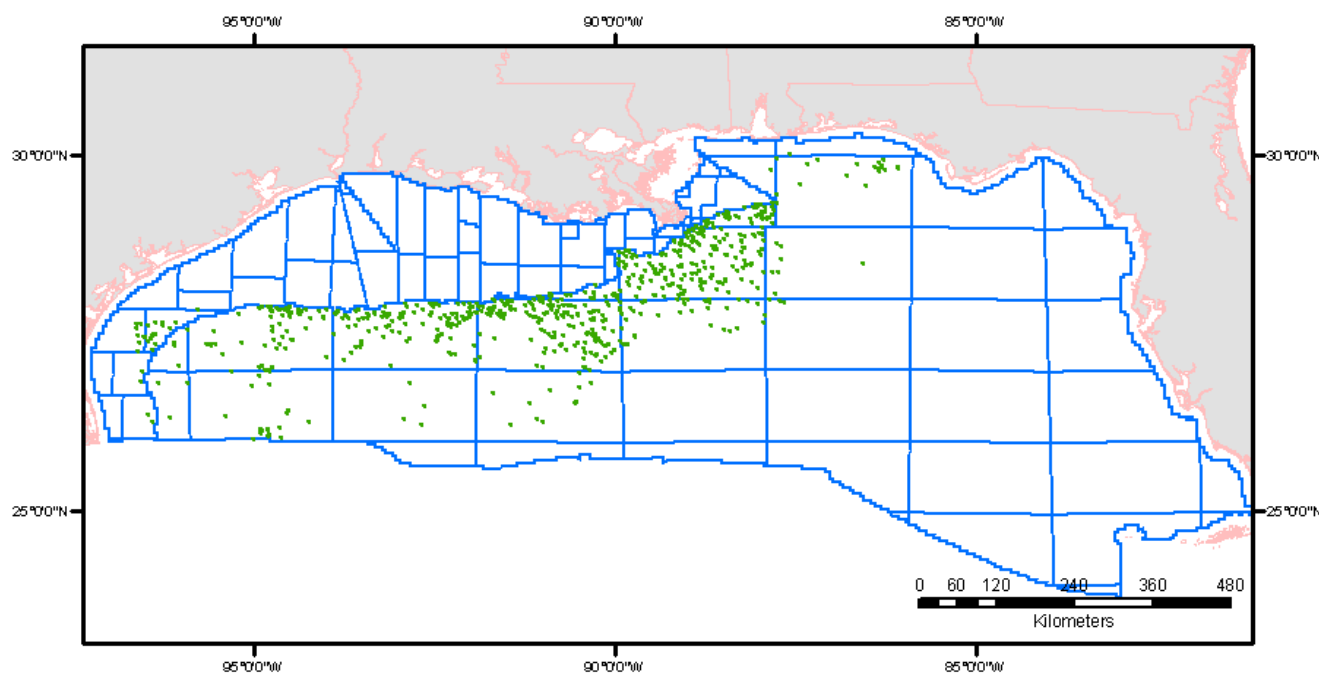


**Figure 73. Location of wells included in sand count study.**

The sand percent values were gridded as a first approximation of the areal distribution of sand-rich facies. Interpretive “soft” data points were added to the scatter set where sediment isopach maps and seismic stratigraphic analysis indicated sand-prone facies. These sand-prone facies are assumed to be found in established sand fairways, in the centers of minibasins, and in those areas just downdip of the Pleistocene shelf edge deltas. The MMS seismic database described in previous sections was also used for the interpretation and validation of the soft data points.

Ultimately, data from all sources were integrated into a single database and gridded to produce a GOM-wide estimation of the sand percent in the shallow section (see figure 74).

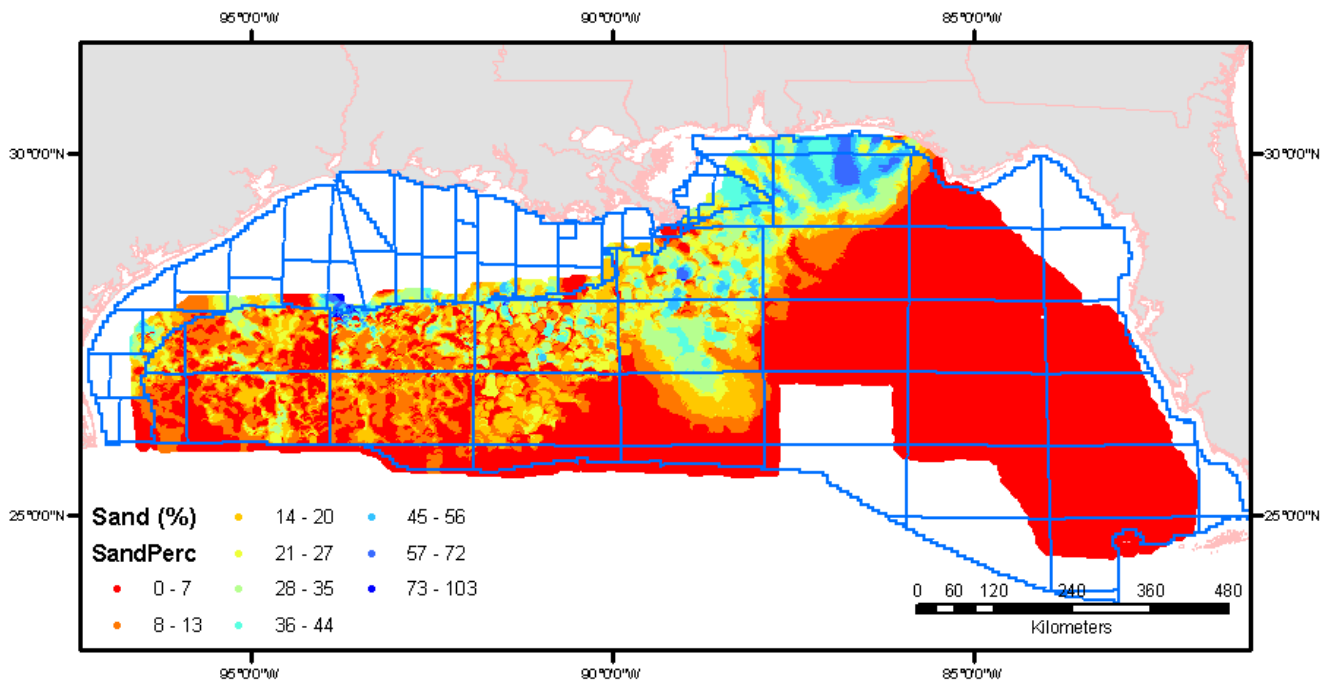


Figure 74. Distribution of sand in the shallow subsurface.





## Chapter IV. Results

### In-Place Resources

The in-place results of this preliminary gas hydrate resource estimate for the Gulf of Mexico (GOM) Outer Continental Shelf are presented in Table 14 and figure 75. Estimated in-place resources are presented as a range of values where the mean is the average or expected value. The 95<sup>th</sup> and 5<sup>th</sup> percentile correspond to a 95-percent probability and a 5-percent probability, respectively, of there being at least as much gas in-place in the GOM as listed. For instance, there is a 95-percent chance that at least 11,112 thousand cubic feet (TCF) of gas hydrate are in-place in the GOM, and a 5-percent chance that more than 34,423 TCF are in-place. Due to the preliminary nature of the MMS hydrate assessment model and the underlying assumption of the fully independent relationship between cells, however, more emphasis should be placed on the mean value and adjacent fractiles, and less on the distal outliers. Also, because individual geologic plays were not identified for this assessment, aggregated results are provided here for the entire GOM, without regard to geologic play or trap type.

**Table 14**  
**In-place Gas Hydrate Resources for the Gulf of Mexico**

Region	95%	mean	5%
Gulf of Mexico	11,112 TCF	21,444 TCF	34,423 TCF

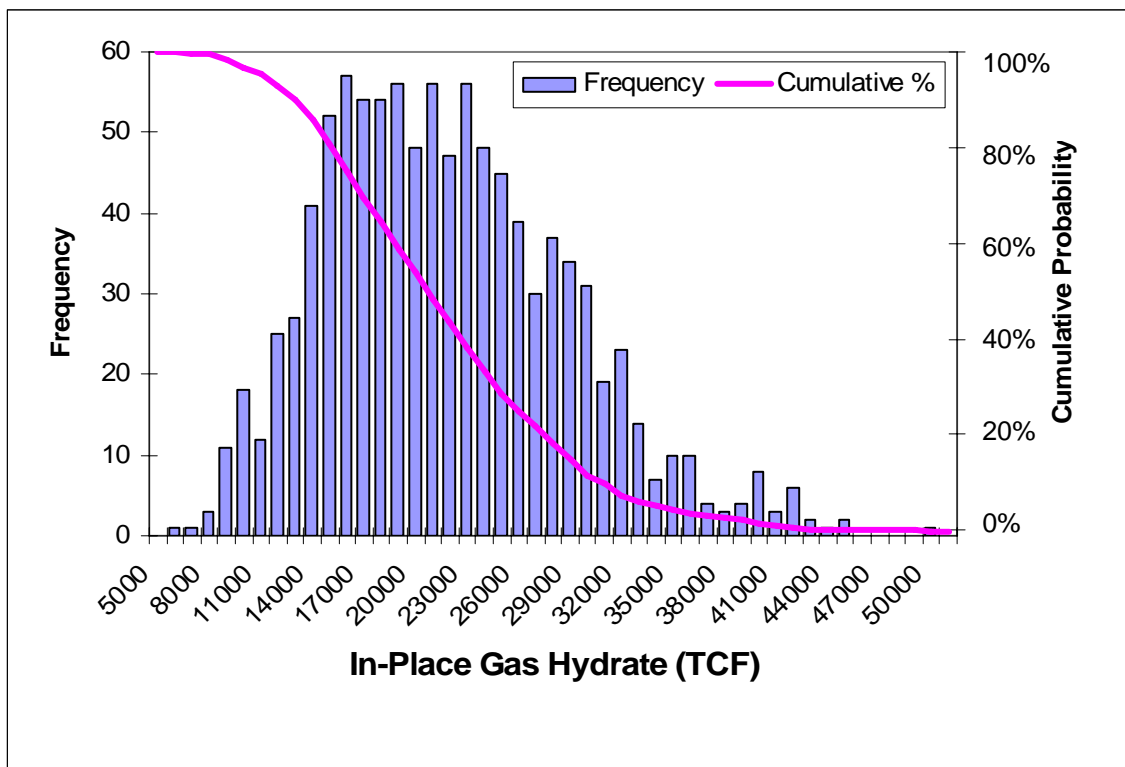


**Figure 75. Distribution of in-place gas hydrate resources, Gulf of Mexico.**

The spatial association of the underlying geologic data inputs for the in-place hydrate model allows several intermediate and final products to be displayed in map view. The mean in-place volume for the GOM, displayed in trillion cubic meters, is shown in figure 76.

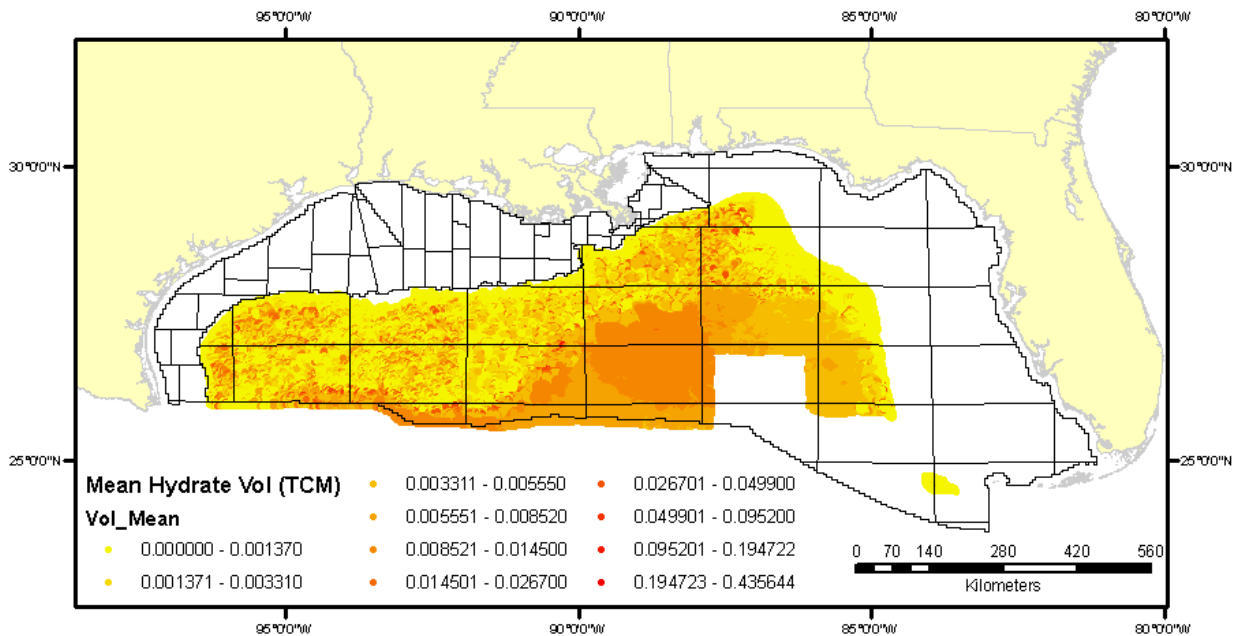


**Figure 76. Mean in-place gas hydrate volume in trillion cubic meters.**

The areal distribution of the in-place volume is heavily influenced by the geometry of the input datasets. For instance, large areas void of any significant hydrate accumulation are present across the salt mini-basin province that comprises much of the upper slope (yellow areas on figure 76). These areas often coincide with very-shallow salt features that occupy the bulk of, and sometimes the entire, hydrate stability zone. Also, areas that offered a thick sedimentary section, such as the deep mini-basins and much of the abyssal plain, provided an abundant supply of biogenic gas from the generation model. The sand-rich cone of the Mississippi Fan is evident due to enhanced methanogenesis and gas generation in sandy sedimentary sections.

Many subjective decisions and interpretations of physical processes also shaped the final volume distribution. The presumed migration mechanism (dip vs. vertical; described in chapter II) varied from the rugose upper slope and Florida Escarpment to the relative homogeneity of the abyssal plain. As a result, all gas generated in most of the abyssal plain remained in the cell of origin, providing a relatively uniform distribution of in-place resources in this physiographic province. Conversely, gas generated in the upper slope was subject to distribution based on stratal dip, creating rich accumulations along the positive margins of the mini-basins. Gas hydrate is modeled to accumulate along the front of the Sigsbee Escarpment in much the same manner.

### Aggregation

Because the total number of cells (202,079) exceeded the software capacity for the model inputs, the in-place model was run on four data sets in the GOM (West, Central, East1, East2) that each contained approximately 50,000 model cells. One thousand trials were executed within each dataset, where a single trial produced an in-place resource value for every cell. These values were summed by data area to obtain the trial's total in-place resource value for that particular data area. The distribution of in-place resources by data area is reported in table 15.

The four data areas were aggregated into a GOM-wide distribution by a Monte Carlo procedure under an assumption of cell independence, where the results in the four areas are believed to be completely independent of one another. While a true subsurface state of nature undoubtedly includes certain dependencies between physical processes, the task of empirically supporting dependency assumptions and physically modeling the

relationships is beyond the scope of this study. In general, an assumption of partial dependency would be preferable to either fully independent or fully dependent.

The assumption of independence used in this study has compressed the range of values from the low point of the distribution to the high point of the distribution, thereby creating an illusion of more certainty in the numbers than actually exists. This effect can be seen in the 5%:95% column of table 15 which represents the ratio of the 5-percent and 95-percent values. An assumption of full dependency, although unreasonable, would result in a maximum possible total GOM ratio of 7.5 to 1. Consequently, the more probable state of nature of a partial dependency would have a ratio ranging from 3.1 to 1 to 7.5 to 1. The mean value would remain the same regardless of which assumption was used.

**Table 15**  
**In-place Gas Hydrate Resources for the Four Data Areas, Gulf of Mexico (trillion cubic feet).**

<b>Region</b>	<b>95%</b>	<b>Mean</b>	<b>5%</b>	<b>5% : 95%</b>
West	1,209 TCF	4,626 TCF	9,925 TCF	8.2 to 1
Central	3,111 TCF	11,476 TCF	23,179 TCF	7.5 to 1
East 1	881 TCF	3,154 TCF	6,385 TCF	7.2 to 1
East 2	652 TCF	2,187 TCF	4,236 TCF	6.5 to 1
<b><i>Gulf of Mexico</i></b>	<b><i>11,112 TCF</i></b>	<b><i>21,444 TCF</i></b>	<b><i>34,423 TCF</i></b>	<b><i>3.1 to 1</i></b>

### **Sand Reservoirs**

At the time of this publication, the in-place resources had not been subjected to further modeling that could predict the technically- and economically-recoverable components of the resource base. The next paragraph describes, in general, the limited state of knowledge thus far as it relates to the ultimate producibility of gas hydrate. Based on this information, we present a subset of the in-place resources by lithology of the sediment host, with the assumption that this is a necessary first step on the road to a full technically-recoverable analysis.

Commercial exploration for gas hydrate in the marine environment is in the very early stages of inception. Globally, marine exploration programs are underway in a number of countries, with high-profile efforts taking place in India, China, Japan, Korea, and to a lesser extent, the United States. Most of these government-funded research ventures have been successful at achieving their stated goals of discovering, logging, and coring high concentrations of gas hydrate. At this time, no marine hydrate accumulation has been developed commercially, due in part to the relatively poor understanding of possible production technologies for gas hydrate in this environment.

The in-place results presented in this report comprise hydrate accumulations hosted in sands, shales, and fractures in the GOM. Recent laboratory research and onshore field-based production testing indicate that porous and permeable sandstone reservoirs have the capacity to produce gas from hydrate using existing technologies (Moridis and Reagan, 2007; Hunter, 2007). Alternatively, no such field-based tests exist for fine-grained hosts that in most cases contain relatively low concentrations of gas hydrate.

The MMS in-place assessment model structure provides an opportunity to report resources by sedimentary host. Based on the recent test results that suggest sandy reservoirs offer the best chance for near-term production, the in-place results of this assessment are presented here as a mean in-place volume in sandstone reservoirs. Mechanically, this is accomplished by determining the fractional measure of saturate-able void space in sands per cell, then applying this fraction to the mean volume captured in the in-place model run. This fractional methodology is applied to each cell in the GOM study area. Saturate-able void space in fractures is not considered in this equation due to the relatively insignificant contribution of fracture void space to the overall total in-place hydrate volume.

Saturate-able void space for sands and shales is calculated by gaining the product of porosity, hydrate saturation, and sand percent. Porosities for sands and shales are calculated using the equations described in chapter II of this report (Eqs. (3.2) and (3.1), respectively). The only variable is depth, which is captured as the mid-point depth of the net HSZ from the in-place model run results. Hydrate saturation of the available pore space is taken as the midpoint value of the triangular saturation distributions described earlier in the methodology report (0.60 for sands and 0.10 for shales). The sand percent is a single value for each cell determined from the sand distribution maps described in chapter III.

The workflow described above provides, by lithologic facies, a unitless measure of the saturate-able void space, by cell. The total saturate-able void space per cell is the sum of the sand and shale values. The percent of saturate-able void space in sand reservoirs per cell is then calculated as the sand void divided by the total void. The product of the sand void fraction and the mean hydrate volume by cell equals the amount of hydrate in sand reservoirs by cell.

Table 16 shows the mean estimate of gas hydrate in-place in sand reservoirs. Only the mean value is reported, as the saturate-able void in sand is calculated in a non-stochastic manner. Additionally, this fractional value is only applied to the mean estimate of the total in-place resource volume. The mean sand-only volume is just over 30 percent of the mean in-place value generated for all reservoirs. Updated releases of the MMS hydrate assessment will contain results from a stochastic technically recoverable model that will only consider sand-hosted resources as candidates for commercial production.

**Table 16**  
**Sand-only Gas Hydrate Resources for the Gulf of Mexico (trillion cubic feet).**

Region	95%	mean	5%
Gulf of Mexico	n/a	6,717 TCF	n/a

### Map View

Because the sand-only volume is a derivative of the mean in-place volume, the results are available to be displayed in map view (see figure 77). The two most significant variables in the sand-only hydrate volume calculation are areal sand distribution (see figure 74 in chapter III) and mean in-place volume (see figure 76). The influence of both is clearly seen in figure 77.

As expected, vast areas in the eastern GOM and in the abyssal plain that were void of any sand component (sand % = 0) are also void of any hydrate resources in sandy reservoirs. Areas along the front of the Sigsbee Escarpment and the margins of mini-basins that contain a rich endowment of in-place resources often retain a relative abundance of sand-only resources. The well-defined, sand-rich cone of the Mississippi Fan stands out as an area that sees very little of its in-place resource base removed, especially in the most proximal position of the fan lobe.

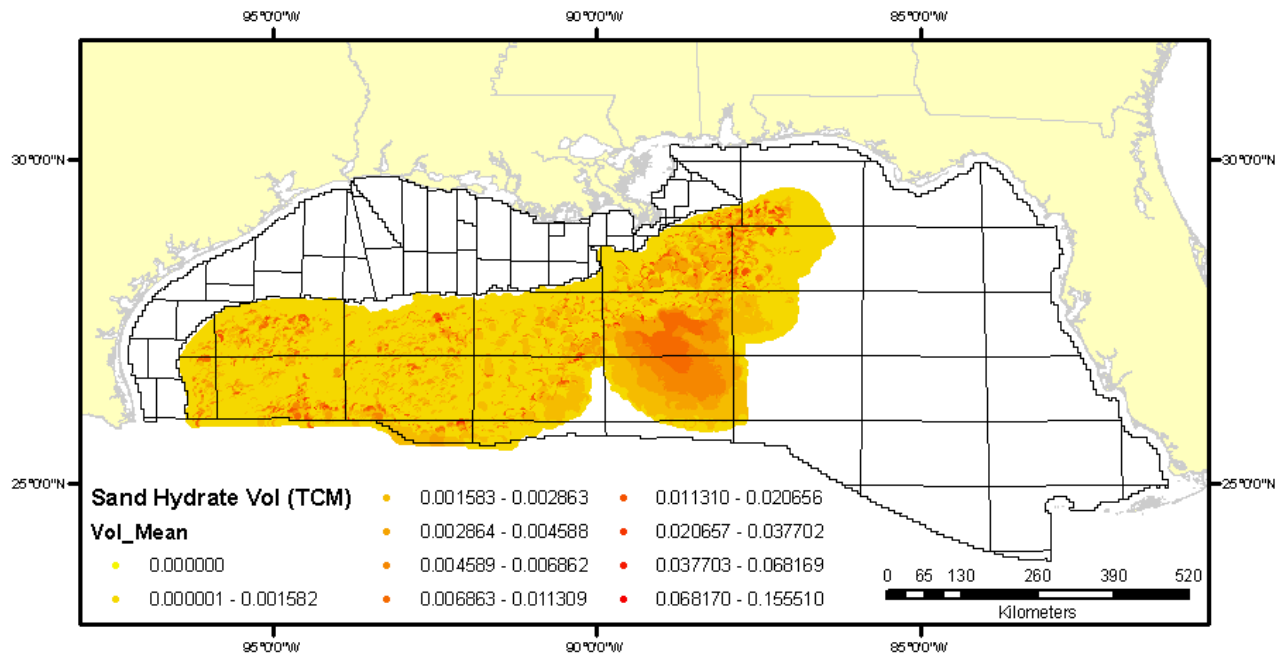


**Figure 77. Sand-only gas hydrate resource volume, Gulf of Mexico (trillion cubic meters).**

**Disclaimer**

The MMS in-place gas hydrate model incorporates varying levels of uncertainty at all levels of input. At this time, the results are not intended to describe commercial or potentially-commercial gas hydrate prospects or accumulations in any specific location, nor should they be used as an indicator of economic feasibility of any given model cell, OCS tract, or geographic area.



## Chapter V. Future Work

The in-place gas hydrate resources described in this report were generated as a means to test the functionality and the predictive accuracy of the MMS in-place assessment model and model methodology. As a result, the gas hydrate resources described in this report will be replaced with final assessment results once all changes have been made to the model.

Most importantly, the model needs to be revised so that it can accommodate all areas of all OCS regions. This includes some parts of the deepwater GOM, where lack of data precluded inclusion in this effort, as well as all of the Atlantic, Pacific, and Alaskan OCS. Also, the MMS does not typically, by practice, report in-place results for national assessments. Our intent is to enhance this current model so that a trial run provides a technically and economically-recoverable run in addition to the in-place resource.

Although not entirely inclusive, a number of the proposed changes to the model structure are described below:

- (1) Develop a sub-model to generate a thermogenic gas component.
- (2) Determine how the rates of methanogenesis estimated for the seafloor vary with respect to depth.
- (3) Incorporate more TOC data.
- (4) Evaluate available WBT measurements.
- (5) Develop technically- and economically-recoverable modules.

These improvements and many others will evolve over the next few years as we learn more about the character and distribution of marine hydrate accumulations. Readers of this initial release are encouraged to forward any suggestions for model improvement to:

*Matthew Frye*  
Resource Evaluation Division  
matt.frye@mms.gov

## References

- Berggren, W.A., Kent, D.V., Swisher, C.C., and Aubry, M.P., 1995, A revised Cenozoic geochronology and chronostratigraphy: Geochronology Time Scales and Global Stratigraphic Correlation, SEPM Special Publication 54: p. 129-212.
- Bouma, A., Coleman, J. M., Meyer, A. W., et al., 1986, *Init. Repts. DSDP*, 96: Washington (U.S. Govt. Printing Office).
- Bruno, R.S., and Hanor, J.S., 2003, Large-scale fluid migration driven by salt dissolution, Bay Marchand dome, offshore Louisiana: Gulf Coast of Geological Societies Transactions, v. 53, p. 97-107.
- Collett, T.S., 1995, Gas hydrate resources of the United States, *in* Gautier, D.L., Dolton, G.L., Takahashi, K.I., and Varnes, K.L., eds., 1995 National assessment of United States oil and gas resources on CD-ROM: U.S. Geological Survey Digital Data Series 30.
- Collett, T.S., 1997, Resource potential of marine and permafrost associated gas hydrates, *in* Max, M.D., Pallenbarg, R.E., and Rath, B.B., eds., Oceanic gas hydrate: guidance for research and programmatic development at the Naval Research laboratory: Proceedings Workshop Naval Research Laboratory Gas Hydrates Research Progress, Washington, DC, p. 51.
- Collett, T.S., 2002, Energy resource potential of natural gas hydrates: American Association of Petroleum Geologists Bulletin, V. 86, no. 11, p. 1971-1992.
- Dallimore, S.R., and Collett, T.S., 2005, Scientific results from the Mallik 2002 gas hydrate production research well program, *in* Dallimore, S.R., and Collett, T.S., eds., Scientific results from the Mallik 2002 gas hydrate production research well program, Mackenzie Delta, Northwest Territories, Canada, Geological Survey of Canada Bulletin 585, p. 1-36.
- Deming, J. W., and Huston, A.L., 2000, An oceanographic perspective on microbial life at low temperatures with implications for polar ecology, biotechnology, and astrobiology, *in* Seckbach, J., ed., Journey to diverse microbial worlds, Kluwer Academic Publishers, Netherlands, p. 149-160.
- D'Hondt, S., Jorgensen, B.B., Miller, D.J., Batzke, A., Blake, R., Cragg, B.A., Cypionka, H., Dickens, G.R., Ferdelman, T., Hinrichs, K.-U., Holm, N.G., Mitterer, R., Spivack, A., Wang, G., Bekins, B., Engelen, B., Ford, K., Gettemy, G., Rutherford, S.D., Sass, H., Skilbeck, C.G., Aiello, I.W., Guerin, G., House, C.H., Inagaki, F., Meister, P., Naehr, T., Niitsuma, S., Parkes, R.J., Schippers, A., Smith, D.C., Teske, A., Wiegel, J., Padilla, C.N., and Acosta, J. L. S., 2004, Distributions of microbial activities in deep seafloor sediments: Science v. 306, p. 2216-2221.
- Dobrynin, V.M., Korotajev, Yu. P., and Plyushev, D.V., 1981, Gas hydrates--A possible energy resource, *in* Meyer, R.F., and Olson, J.C., eds., Long-Term Energy Resources: Boston, Pitman, Publishers, p. 727-729.
- Evans, M., Hastings, N., and Peacock, B., 2000, Statistical distributions. 3rd ed., J. Wiley and Sons, Inc., New York.
- Fredrickson, J. K., McKinley, J. P., Bjornstad, B.N., Long, P. E., Ringelberg, D. B., White, D. C., Sufliata, J. M., Krumholz, L., Colwell, F. S., Lehman, R. M., and Phelps, T. J., 1997, Pore-size constraints on the activity and survival of subsurface bacteria in a Late Cretaceous shale-sandstone sequence, northwestern, New Mexico: Geomicrobiology Journal, v. 14, p. 183-202.



- Hanor, J.S., 2007, Pre-production spatial variation in formation water salinity in a deepwater Gulf of Mexico field, *in* Bullen, T., and Wang, Y., eds., *Water-Rock Interaction*, Taylor and Francis Group, London, p. 505-508.
- Hanor, J.S., 2004, The role of salt dissolution in the geologic, hydrologic, and diagenetic evolution of the northern Gulf Coast sedimentary basin, *in* Post, P.J., ed., *Salt-sediment interactions and hydrocarbon prospectivity: concepts and case studies for the 21st century*, 24th Annual Gulf Coast Section SEPM Foundation Research Conference, p. 464-501.
- Hamilton, E.L., 1976, Variations of density and porosity with depth in deep-sea sediments: *Journal of Sedimentary Petrology*, v. 46, no. 2, p. 280-300.
- Holder, G.D., Angert, P.F., John, V.T., and Yen, S., 1982, A thermodynamic evaluation of thermal recovery of gas from hydrates in the earth: *Journal of Petroleum Technology*, May 1982, p. 1127-1132.
- Hood, K.C., Wenger, L.M., Gross, O.P., and Harrison, S.C., 2002, Hydrocarbon systems analysis of the northern Gulf of Mexico: delineation of hydrocarbon migration pathways using seeps and seismic imaging, *in* Schumacher, D., and LeSchack, L.A., eds., *Surface exploration case histories: Applications of geochemistry, magnetics, and remote sensing*, AAPG Studies in Geology 48 and SEG Geophysical References Series No. 11, p. 25-40.
- Hunter, R.B., 2007, Resource characterization and quantification of natural gas-hydrate and associated free-gas accumulations in the Prudhoe Bay – Kuparuk River area on the North Slope of Alaska: 1Q2007 Quarterly Progress Report, Cooperative Agreement Award Number DE-FC-01NT41332.
- Jackson, B. E., and McInerney, M. J., 2002, Anaerobic microbial metabolism can proceed close to thermodynamic limits: *Nature*, v. 415, p. 454-456.
- Johnson, N. L., and Kotz, S., 1972, *Distributions in statistics: continuous multivariate distributions*, Wiley Series in Probability and Mathematical Statistics, John Wiley & Sons, Inc., New York-London-Sydney.
- Jones, M.S., 2003, The regional geothermal heat flow regime of the north-central Gulf of Mexico continental slope, Texas Tech University, MS Thesis, 135 p.
- Kvenvolden, K.A., 1993, A primer in gas hydrates, *in* Howell, D.G., ed, *The future of energy gases: U.S. Geological Survey Professional Paper 1570*, p. 279-292.
- Lein, A.Y., Namsaraev, G.B., Trotsyuk, V.Y. & Ivanov, M.V., 1981, Bacterial methanogenesis in Holocene sediments of the Baltic Sea, *Geomicrobiol. J.*, v. 2, p. 299-315.
- Lochte, K., and Turley, C.M, 1988, Bacteria and cyanobacteria associated with phytodetritus in the deep sea, *Nature*, London, v. 333, p. 67-69.
- Meyer, R.F., 1981, Speculations on oil and gas resources in small fields and unconventional deposits, *in* Meyer, R.F., and Olson, J.C., eds., *Long-Term Energy Resources*: Boston, Pitman, p. 49-72.
- Milkov, A. V. and Sassen, R., 2001, Estimate of gas hydrate resource, northwestern Gulf of Mexico continental slope: *Marine Geology*, v. 179, p. 71-83.
- Moridis, G.J., and Reagan, M.T., 2007, Gas production from oceanic class 2 hydrate accumulation, OTC 18866, 2007 Offshore Technology Conference, Houston, TX.
- Moridis, G.J., Seol, Y., and Kneafsey, T.J., 2006, Studies of reaction kinetics of methane hydrate dissociation in porous media: Topical Report, Lawrence-Berkley National Laboratory Press.

- Nowlin, W. D., Jr., Jochens, A.E., DiMarco, S.F., Reid, R.O., and Howard, M.K., 2001, Deepwater physical oceanography reanalysis and synthesis of historical data: Synthesis Report, OCS Study MMS 2001-064, U.S. Dept. of the Interior, Minerals Management Service, Gulf of Mexico OCS Region, New Orleans, LA, 528 p.
- O'Brien, J.J., and Lerche, I., 1988, Impact of heat flow anomalies around salt sheets in the Gulf Coast on hydrocarbon maturity: model and observations: Transactions of the Gulf Coast Association of Geological Societies, vol. 38, p. 213-245.
- Parkes, R. J., B. A. Cragg, J. C. Fry, R. A. Herbert, and J. W. T. Wimpenny, 1990, Bacterial biomass and activity in deep sediment layers from the Peru margin. *Phil. Trans. Roy. Soc. Lond., A* 331:139-153.
- Parkes, R. J., Cragg, B.A., Bale, S. J., Getliff, J. M., Goodman, K., Rochelle, P. A., Fry, J. C., Weightman, A. J., and Harvey, S. M., 1994, Deep bacterial biosphere in Pacific Ocean sediments: *Nature* v. 371, p. 410-413.
- Parkes, R. J., Webster, G., Cragg, B. A., Weightman, A. J., Newberry, C. J., Ferdelman, T. G., Kallmeyer, J., Jorgensen, B.B., Aiello, I. W., and Fry, J.C., 2005, Deep sub-seafloor prokaryotes stimulated at interfaces over geological time: *Nature*, v. 436. p. 390-394.
- Paull, C.K., Ussler III, W., Lorenson, T., Winters, W., and Dougherty, J., 2005, Geochemical constraints on the distribution of gas hydrates in the Gulf of Mexico: *Geo-Marine Letters*, v. 25, no. 5, p. 273-280.
- Pindell, J., Kennan, L., and Barrett, S., 2000, Putting it all together again: *AAPG Explorer*, v. 21, October 2000.
- Pooladi-Darvish, M., 2004, Gas production from hydrate reservoirs and its modeling: *Journal of Petroleum Technology*, v. 56, no. 6, p. 65-71.
- Price, P.B. and Sowers, T., 2004, Temperature dependence of metabolic rates for microbial growth, maintenance and survival: *Proceedings of the National Academy of Sciences*, v. 101, no. 13, p. 4631-4636 (March 30, 2004).
- Rice, A.L., Biller, D.S.M., Fry, J.C., John, A.W.G., Lampitt, R.S., Mantoura, R.F.C. & Morris, R.J., 1986, Seasonal deposition of phytodetritus to the deep-sea floor, *Proc. Royal Society of Edinburgh Section B-Biological Sciences* (88):265-279.
- Senior, E., Lindstrom, E.B., Banat, I.M & Nedwell, D.B., 1982, Sulfate reductin and methanogenesis in the sediment of a salt marsh on the east coast of the United Kingdom, *Appl. Environ. Microbiol.* v. 43, p. 987-996.
- Simmons, G. R., 1992, The regional distribution of salt in the northwestern Gulf of Mexico: styles of emplacement and implications for early tectonic history: Ph.D. dissertation, Texas A&M University, College Station, Texas, 180 p.
- Sloan, E.D., Jr., 1998, *Clathrate hydrates of natural gases*: Marcel Dekker, Inc., New York, 641 p.
- Soloviev, V.A., 2000, Global estimation of gas content in submarine gas hydrate accumulations: VI International Conference on Gas in Marine Sediments, St. Petersburg, Russia, p. 123-125.
- Spinelli, G.A., Giambalvo, E.R., and Fisher, A.T., 2004, Sediment permeability, distribution, and influence on fluxes in oceanic basement, *in* Davis, E.E., and Elderfield, H., eds., *Hydrogeology of the Oceanic Lithosphere*: Cambridge University Press, p. 151-188.

## Appendix A

### Details of Derivation of Productivity Function for a Single Species

The modified version of Arrhenius' law appearing in figure 19 possesses four qualitative features discussed earlier and repeated here for completeness:

1. Methane production strictly adheres to Arrhenius' Law as in Eq. B.1 for  $T_{sf}(WD) < T < T^* - \delta$ ,  $\delta$  is a small positive constant. In units of  $x$ ,  $T_{sf}(WD) / T^* = x_0 < x < 1 - \varepsilon$ ,  $\varepsilon = \delta/T^*$ .
2. At  $T = T^* - \delta$ , Eq. B.2 equals  $\exp\{\phi x (T - T^*)\}$  and is "smooth" (i.e., first derivatives as  $T$  approaches  $T^* - \delta$  from above and from below are equal). Equivalently at  $x = 1 - \varepsilon$ , Eq. (1.18) equals  $\exp\{\phi x (x - 1)\}$  and is "smooth" in the sense just cited.
3. Methane production peaks at  $T = T^*$  or, in terms of  $x$ , at  $x = 1.0$ .
4. Methane production declines to a small value  $\kappa > 0$  at  $2T^*$  ( $x = 2$ ).

Both  $\varepsilon$  and  $\kappa$  are "tuning" parameters that can be chosen to make the shape of the rate function conform to our best understanding of how methanogenic productivity behaves as a function of temperature and to reduce generation above 70 °C to a negligible amount.

A fifth feature is that the rate of production of methane by a single species of methanogenic archaea for temperatures at and above  $T^* - \delta$  is proportional to the function  $f_2(x) = C x \exp\{-\lambda x^\beta\} x^\alpha$ .<sup>17</sup>

To construct a rate function with all of these properties define

$$(A.1) \quad f_1(x) = \exp\{-\phi(1-x)\} \quad \text{if } x_0 \leq x < 1 - \varepsilon,$$

$$f_2(x) = C \times \exp\{-\lambda x^\beta\} x^\alpha \quad \text{if } 1 - \varepsilon \leq x < \infty, \alpha > 0$$

and

$$(A.2) \quad f_2(2) = \kappa.$$

Eq. (A.1) says that the functions  $f_1$  and  $f_2$  meet at  $x = 1 - \varepsilon$ ; (i.e.,  $f_1(1 - \varepsilon) = f_2(1 - \varepsilon)$ ) or at  $x = 1 - \varepsilon$

$$(A.3) \quad \exp\{-\phi(1-x)\} = C \times \exp\{-\lambda x^\beta\} x^\alpha$$

Eq. (A.3) says that the maximum rate of production occurs at  $x = 1$ ; i.e.  $f_2(x) = 0$ . At  $x = 1$ ,  $\alpha = \lambda\beta$ .

With  $\alpha = \lambda\beta$ , at  $x = 1 - \varepsilon$ , Eq. A.3 becomes

$$(A.4) \quad \exp\{-\phi\varepsilon\} = C \times \exp\{-\lambda(1-\varepsilon)^\beta\} \times (1-\varepsilon)^{\lambda\beta}$$

or

$$(A.5) \quad \ln C = -\phi\varepsilon + \lambda(1-\varepsilon)^\beta - \lambda\beta \ln(1-\varepsilon).$$

<sup>17</sup> Multiply by the product of the intercept and scale factor  $A_0(T_0(WD)) \times A$ . Change subscripts to conform to earlier notation to find the rate of methane productivity in grams of methane/gram of organic carbon/million years at a given temperature ratio  $x$ .

In order to assure smoothness we impose the condition that the derivatives of  $f_1$  and  $f_2$  at  $x = 1 - \varepsilon$  are equal. Given  $\alpha = \lambda\beta$ , equal derivatives at  $x = 1 - \varepsilon$  lead to

$$(A.6) \quad \phi \exp\{-\phi(1-x)\} = C \exp\{-\lambda x\} x^{\lambda\beta} \times \left(\frac{\lambda\beta}{x}\right) [1-x^\beta]$$

at this particular value of  $x$ . Using Eq.(A.4), Eq. (A.6) yields

$$(A.7) \quad \phi = \frac{\lambda\beta}{1-\varepsilon} [1-(1-\varepsilon)^\beta]$$

or

$$(A.8) \quad \frac{\phi(1-\varepsilon)}{\beta[1-(1-\varepsilon)^\beta]} = \lambda.$$

This last relation allows us to express Eq. (A.5) as

$$(A.9) \quad \ln C = -\phi\varepsilon - \frac{\phi(1-\varepsilon)}{\beta} + \lambda \times [1 - \beta \ln(1-\varepsilon)].$$

If we define

$$(A.10) \quad h(\beta) = \frac{\phi(1-\varepsilon)}{1-(1-\varepsilon)^\beta},$$

we can write Eq. (A.5) as

$$(A.11) \quad \ln C = -\phi\varepsilon + h(\beta) \times \left[ \frac{(1-\varepsilon)^\beta}{\beta} - \ln(1-\varepsilon) \right].$$

We also require Eq. (A.4) that  $f_2(2) = C x \exp\{-\lambda 2^\beta\} 2^{\lambda\beta} = \kappa$  or

$$(A.12) \quad \ln C = \ln \kappa + \lambda 2^\beta - \lambda\beta \times \ln 2.$$

Substituting Eq. (A.8) in this equality gives

$$(A.13) \quad \ln C = \ln \kappa + h(\beta) \times \left[ \frac{2^\beta}{\beta} - \ln 2 \right].$$

Together, Eq. (A.9) and Eq. (A.13) yield an equation in  $\beta$  alone:

$$(A.14) \quad 0 = \ln \kappa + \phi\varepsilon + h(\beta) \times \left[ \frac{2^\beta - (1-\varepsilon)^\beta}{\beta} + \ln\left(\frac{1-\varepsilon}{2}\right) \right].$$

### Algorithms

To recover  $\beta$ ,  $C$  and  $\lambda$  by direct calculation of  $\beta$ :

1. Solve Eq. (A.14) for  $\beta$ ;
2. Given  $\beta$ , solve Eq. (A.8) for  $\lambda$ ;
3. Given  $\beta$  and  $\lambda$ , solve Eq. (A.9) or Eq. (A.13) for  $C$ .

The structure of Eq. (A.14) becomes clearer if we define constants  $A = -(\ln \kappa + \phi \varepsilon) / \phi(1 - \varepsilon)$  and  $B = \ln(\frac{1-\varepsilon}{2})$  so that

$$(A.15) \quad A = h(\beta) \times \left[ \frac{2^\beta - (1-\varepsilon)^\beta}{\beta} + B \right]$$

or equivalently

$$(A.16) \quad A \times [1 - (1-\varepsilon)^\beta] - B - \frac{2^\beta - (1-\varepsilon)^\beta}{\beta} = 0.$$

An alternative spreadsheet algorithm is:

1. Create a column of values of  $\beta$ ;
2. For each value of  $\beta$ , solve Eq. (A.8) for  $\lambda$ ;
3. Given each  $(\beta, \lambda)$  pair, solve Eq. (A.8) for a value of  $\ln C$  and Eq. (A.13) for a value of  $\ln C$ .
4. Find a  $(\beta, \lambda)$  pair for which the two values for  $\ln C$  found from Eq. (A.9) and Eq. (A.13) are equal.

The  $(\beta, \lambda)$  pair found in Step 4 constitutes a solution to Eq. (A.9) and Eq. (A.13).



## Appendix B

### Model of Methanogenic Productivity of a Single Species of Methanogenic Archaea

Seafloor temperature,  $T_{SF}$ , is a function of water depth,  $WD$ , ( $T_{SF}(WD)$ ). For a single species of methanogen at the seafloor, there is a minimum rate of production of methane  $A_{SF}(T_{SF}(WD))$ , which is a function of seafloor temperature and other features of the seafloor environment. The value assumed by  $A_{SF}(T_{SF}(WD))$  scales the intercept of the rate function shown in figure 17. For temperature  $T_{SF}(WD)$  at the seafloor, it incorporates the collective influence on productivity of *all other* variables that impact productivity.

If all conditions at the seafloor, other than temperature, could be held constant, as temperature traverses a temperature interval beginning at seafloor temperature and terminating at a temperature ( $T^*-\delta$ ) below peak productivity temperature  $T^*$ , the rate of productivity  $A_{SF}(T)$  increases according to a strict form of Arrhenius' Law as shown in Eq. (B.1), with  $\Phi_0 = \ln(2)/10$ :

$$(B.1) \quad A_{SF}(T) = A_{SF}(T_{SF}(WD)) \times \exp\{\phi_0 \times (T - T_{SF}(WD))\} \quad \text{for } T_{SF}(WD) \leq T < \infty.$$

In Eq. (B.1), productivity,  $A_{SF}(T)$ , increases exponentially as temperature ( $T$ ) rises and has no finite upper bound. In practice, the temperature domain for which Arrhenius' Law is a reasonable model of methane productivity stops, according to Dr. Colwell, at a temperature below a maximum productivity temperature,  $T^*$  between 35 °C and 45 °C.

Let  $[T_{SF}(WD), T^* - \delta]$  with  $\delta > 0$  be the temperature domain for which Arrhenius' Law is assumed to hold. We describe next how to assure that the rate function smoothly transitions at  $T^* - \delta$  from Eq. (B.1) to a unimodal function with a finite maximum value that, above the maximum value, declines sharply to a trivial level of production ( $\kappa > 0$ ) at terminal temperature, here taken to be  $T_\kappa = 70$  °C.

It is convenient to rescale temperature  $T$  and do the analysis in terms of the ratio  $x = T/T^*$  (the ratio of  $T$  to peak temperature  $T^*$ ). To this end, let  $A_I = \exp\{\phi_0 x (T^* - T_{SF}(WD))\}$  and rewrite Eq. (B.2) as

$$(B.2) \quad A(T) = A_{SF}(T_{SF}(WD)) \times A_I \times \exp\{\phi_0 \times (T - T^*)\} \quad \text{for } T_{SF}(WD) \leq T < \infty.$$

In terms of rescaled temperature  $x \equiv T/T^*$ ,  $\phi = \phi_0/T^*$  and  $x_0 \equiv T_{SF}/T^*$  Eq. (B.2) is

$$(B.3) \quad A(x) = A_{SF}(T_{SF}(WD)) \times A_I \times \exp\{-\phi \times (1 - x)\} \quad \text{for } x_0 \leq x < \infty.$$

Properties of the modified law are:

1. Methane production strictly adheres to Arrhenius' Law as in Eq. (B.2) for  $T_{SF}(WD) < T < T^* - \delta$ ,  $\delta$  is a small positive constant. In units of  $x$ ,  $T_{SF}(WD)/T^* = x_0 < x < 1 - \varepsilon$ ,  $\varepsilon = \delta/T^*$ .
2. At  $T = T^* - \delta$ , Eq. (B.2) equals  $\exp\{\phi_0 x (T - T^*)\}$  and is "smooth" (i.e., first derivatives as  $T$  approaches  $T^* - \delta$  from above and from below are equal). Equivalently at  $x = 1 - \varepsilon$
3. Methane production peaks at  $T = T^*$  or, in terms of  $x$ , at  $x = 1.0$ .
4. Methane production declines to a small value  $\kappa > 0$  at  $2T^*$  ( $x = 2$ ).

Both  $\varepsilon$  and  $\kappa$  are "tuning" parameters that can be chosen to make the shape of the rate function conform to our best understanding of how methanogenic productivity behaves as a function of temperature and to reduce generation above 70 °C to a negligible amount.

The rate of production of methane by a single species of methanogenic archaea for temperatures at and above  $T^* - \delta$  is assumed to be proportional to the function  $f_2(x) = C x \exp\{-\lambda x^\beta\} x^\alpha$  (figure B.1).

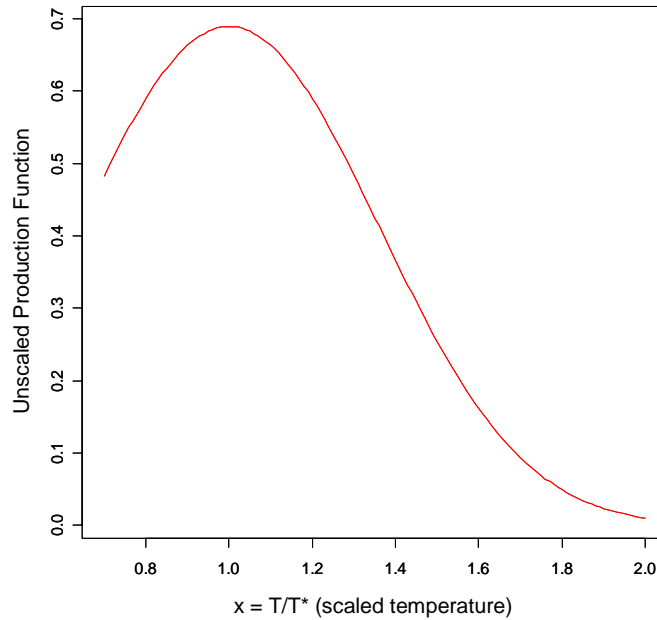


**Figure B.1.** A plot of  $f_2(x) = C x \exp\{-\lambda x^\beta\} x^\alpha$  versus  $x$ .

In figure B.2, a plot of  $f_2(x)$  for  $0.70 \leq x \leq 2.0$  is generated as follows:

1. Rescale by a maximum temperature of 35 °C so that  $x = 1.0$  is a maximum rescaled temperature value. Then  $\phi_0$  becomes  $\phi = 0.069315 \times 35 = 2.426025$ .
2. Choose a match point at  $T^* - \delta = 24.5$  °C; then  $\varepsilon = 0.30$ . This implies that strict adherence to Arrhenius' Law ends at 24.5 °C.
3. At 24.5 °C, transition to a function that peaks at 35 °C and declines as temperature increases beyond 35 °C.
4. At 70 °C,  $x=2$  and we choose  $\kappa = 0.01$  at this temperature. This means that, at 70 °C, methane production is one hundredth of the initial methane production rate  $A_0(d) \times A_1$ . These choices of  $\varepsilon$  and  $\kappa$  yield  $\beta = 2.99684$  and  $\lambda = 0.863019$ .

Here  $f_2(x) = 1.633398 x \exp\{-0.863019 x^{2.99684}\} x^{2.58633}$  and  $\exp\{-\phi(1-\varepsilon)\} = \exp\{-0.727808\}$  at the meet point  $x = 0.70$ ; function values are 0.4829 at  $x = 0.70$ . Paste  $\exp\{-\phi(1-x)\}$  for  $x = x_0, \dots, 0.70$  onto figure B.1 to get the complete function in figure B.2.

Figure B.2 honors Arrhenius' Law from water bottom temperature to a temperature of  $0.70 \times 35$  °C, then transitions to a unimodal function with a peak at 35 °C. As the temperature ratio  $x$  traverses  $[1, \infty]$ , the rate of methane productivity declines; at 70 °C and above, productivity is insignificant ( $\kappa = 0.01$  implies that the rate of productivity at 70 °C is 1/100 of the peak productivity rate).

The domain of the rate function shown in figure B.2 is in dimensionless units (Temperature  $T/T^*$ ). When multiplied by  $A_{SF}(T_{SF}(WD)) \times A_1$ , the vertical axis measures the rate of methane productivity at seafloor conditions in grams of methane/gram of organic carbon/million years (for details, see Appendix A).



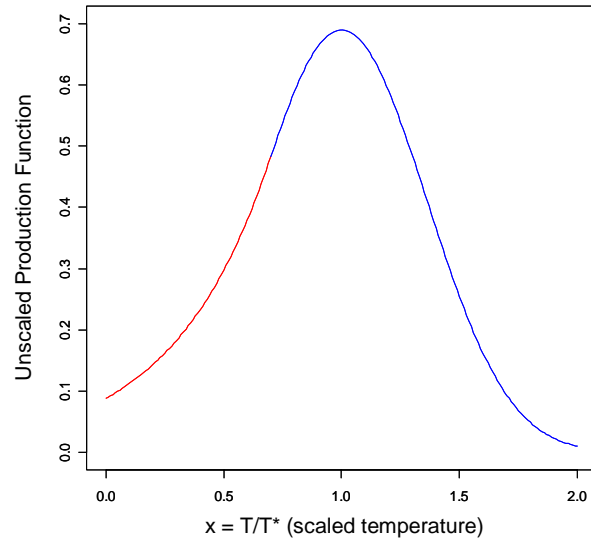


**Figure B.2. Modified Arrhenius' Law for rate of methane production by a single species of methanogen (in grams of methane/gram of organic carbon/million years) as a function of sediment temperature. The red, initial part of the function is a graph of a strict form of Arrhenius' Law. The blue section is a unimodal function "smoothly pasted" to the strict form of Arrhenius' Law; this function declines rapidly as x increases above 1.0. The x-axis is the variable x (defined in the text); the y-axis is unscaled rate of methanogenic production.**



## Appendix C

### Details of Derivation of Productivity Function for a Community of Multiple Species

Recall that we want to capture the collective impact on the rate of methane production of a *mixture of many species of methanogens*. Under reasonable assumptions about how methanogenic species are mixed, as the number species in an ecosystem increases, the peak of the production rate function produced by mixing may “smooth out” and vary slowly in the neighborhood of a single absolute maximum rate. If so, it is reasonable to model the rate function as mesa-like in a neighborhood of an absolute maximum rate in place of mixing individual rate functions.

To accommodate a relatively “flat” peak in the neighborhood of the temperatures associated with maximum productivity, we modified the form of the function described for the productivity of a single methanogenic species as a function of temperature. Figure 18 is an example of a mesa-like function that allows a smooth transition to it from a strict form of Arrhenius’ Law.

The function generating the graph shown in figure 19,  $x^\beta(1-x)^\beta$ , is flexible enough to capture the collective impact of many species on methane production--each with a different maximum productivity over the temperature domain assumed to encompass these maxima (35 °C – 45°C).<sup>18</sup>

The mathematics of smooth pasting a mesa-like function, like that in figure 18, to an exponential form of Arrhenius’ Law for temperatures below about 35 °C (below about 0.875 in the scale of the graph) appear here. The magnitude of variation in the production rate as  $x$  traverses the domain of this function (here 35 °C – 45 °C) is controlled by the parameter  $\beta$ .

#### Mesa Functions

For completeness, we state again the principal assumptions used to construct a mesa-like rate function.

1. Methane production peaks at  $T^*$  and adheres strictly to an exponential version of Arrhenius’ Law for  $T(WD) < T < T^* - \delta$ ,  $\delta =$  a positive constant.

We rescale for notational convenience and express temperature in units  $x$  of  $T^*$ :  $T(WD)/T^* = x_0 < x < 1 - \varepsilon$ ,  $\varepsilon = \delta/T^*$ . The rate function peaks at  $x = 1.0$  in units of  $T^*$ .

The exponential version of Arrhenius’ law is of the form:

$$(C.1) \quad f(x|\phi) = \exp\{-\phi(1-x)\}, \text{ for } 0 < x < 1 - \varepsilon \equiv x_0.$$

2. The function  $f(x|\phi)$  is smooth pasted at  $x = x_0$  to a function  $f_2$  that has these properties:

- (a) At  $x = x_0$ ,  $f_2(x) = f(x|\phi)$  and  $f_2'(x) = f'(x|\phi)$ ; i.e., pasting is smooth at the meet point;
- (b)  $f_2$  peaks at  $x = 1$  but varies little in a pre-specified neighborhood  $(x_*, x^*)$  of the peak; the amount of variation of  $f_2$  as  $x$  traverses  $(x_*, x^*)$  is controllable.

The domain of the mesa function

$$(C.2) \quad f_2(x) \equiv C \times \exp\{\lambda[(x^* - x)(x - x_*)]^\beta\}$$

---

<sup>18</sup> This mesa-like function need not be symmetric: use  $x^\eta(1-x)^\beta$ ,  $\eta \neq \beta$ .

is restricted to  $x^* \leq x \leq x^*$  and the meet points, mode of the mesa function and limit points of the domain of  $f_2(x)$  are ordered according to  $x^* < x_0 < I < x_1 < x_2 < x^*$ .

3. At  $x = x_1$ , the function  $f_2$  is smooth pasted to a function  $f_3$  that declines rapidly.

4. At a prescribed temperature  $x = x_2 > x^*$ ,  $f_3$  is less than or equal to a small positive number  $\kappa$ .

#### Equal function Values at $x = x_0$

As  $f(x/\phi) = f_2(x)$  at  $x = x_0$ , if we define  $U_0 = (x^* - x_0)(x_0 - x^*)$  and  $\kappa_0 = \phi(1 - x_0)$ , then

$$(C.3) \quad K_0 = \ln C + \lambda \times U_0^\beta \text{ or } \lambda = \frac{K_0 - \ln C}{U_0^\beta}$$

#### Equal Derivatives at $x = x_0$

Also define  $U_1 = x^* + x^* - 2x_0$ . Then equal derivatives at  $x = x_0$  give

$$(C.4) \quad \lambda\beta = \frac{\phi}{U_1 \times U_0^{\beta-1}}$$

The parameter  $\beta$  determines how much  $f_2$  varies in a neighborhood of the peak value (here 1.0). Because  $U_1$ ,  $U_2$  and  $\phi$  are known constants, fixing  $\beta$  is sufficient to determine  $\lambda$  and  $C$  using Eqs. (C.3) and (C.4). In particular,

$$(C.5) \quad \ln C = K_0 - \frac{\phi \times U_0}{\beta \times U_1}$$

#### Gamma Function Matched to Mesa Function at $x = x_1$

At  $x = x_1 = 1 + \eta < x^*$ , smooth paste  $f_3(x) = K x \exp\{-\gamma x\} x^\alpha$  to the mesa function.

Define constant terms  $U_2 = (x^* - x_1)(I - x^*)$  and  $U_3 = x^* + x^* - 2x_1$ . If we set  $f_3(x) = f_2(x)$  at  $x = x_1$ , then

$$(C.6) \quad \ln K - \gamma x_1 + \alpha \ln x_1 = \ln C + \lambda \times U_2^\beta \equiv C_1$$

Equal Derivatives at  $x = x_1$ ,  $f_3'(x_1) = f_2'(x_1)$ , imply that

$$(C.7) \quad \frac{\alpha}{x_1} - \gamma_1 = -\lambda\beta \times U_3 \times U_2^{\beta-1} \equiv C_2$$

**Condition 4** says that, the rate of production of hydrates is very small at a prescribed temperature  $x_2 > x^*$ ; namely, at  $x = x_2$ ,  $f_3(x_2) = \kappa$ ,  $\kappa$  = a small constant:

$$(C.8) \quad \ln K + \alpha x_2 - \gamma \ln x_2 = \ln \kappa$$

Given  $\beta$ ,  $\lambda$  and  $C$ , the three equations, Eq. (C.5), (C.7), and (C.8) possess a unique solution in  $\alpha$ ,  $\gamma$  and  $\kappa$  so that all four conditions imposed on the shape of the rate function are met.

#### Algorithm

Steps 1 - 5 match Arrhenius' Law to the mesa function  $f_2(x)$  at  $x = x_0$

1. Specify a numerical value of  $\beta$ .
2. Choose  $\frac{1}{2}(x^* + x^*) > x_0 > 0$  and then compute  $U_0 = (x^* - x_0)(x_0 - x^*)$  and  $U_1 = x^* + x^* - 2x_0$ .

3. Compute  $\lambda = \frac{\phi}{\beta \times U_1 \times U_0^{\beta-1}}$

4. Given  $\beta$  and  $\lambda$ , compute  $\ln C = K_0 - \frac{\phi \times U_0}{\beta \times U_1}$ ,  $K_0 \equiv -\phi(1 - x_0)$ .

5. Compute  $U_2 = (x^* - x_l)(x_l - x_*) > 0$  and  $U_3 = x^* + x_* - 2x_l$ .<sup>19</sup>

To smooth paste  $f_3(x) = K x \exp\{-\gamma x\} x^\alpha$  to  $f_2(x)$  at  $x = x_l$ , solve

$$(C.9) \quad \ln K - \gamma x_l + \alpha \ln x_l = C_1$$

$$(C.10) \quad \frac{\alpha}{x_l} - \gamma = C_2$$

and

$$(C.11) \quad \ln K - \gamma x_2 + \alpha \ln x_2 = \ln \kappa$$

for  $\gamma$ ,  $K$  and  $\alpha$

5. Subtract Eq. (C.8) from Eq. (C.6) to get

$$(C.B.1) \quad \gamma(x_2 - x_1) + \alpha \ln\left(\frac{x_1}{x_2}\right) = C_1 - \ln \kappa.$$

6. Write Eq. (C.7) as  $\alpha = (C_2 + \gamma)x_l$  and substitute into Eq. (C.9):

$$(C.B.2) \quad \gamma \times [(x_2 - x_1) + x_l \ln\left(\frac{x_1}{x_2}\right)] = C_1 - C_2 x_l \ln\left(\frac{x_1}{x_2}\right) - \ln \kappa.$$

7. Use Eq. (C.9) and Eq. (C.10) to compute  $\alpha$  and  $\gamma$ .

8. Given  $\gamma$  and  $\alpha$  compute  $\ln K = C_1 + \gamma x_l - \alpha \ln x_l$ .

In order for  $f_2$  to exhibit mesa-like behavior, the parameter  $\beta$  must be positive and small. The mesa function shown in figure 18 has  $\beta = 0.10$ ,  $\lambda = 0.70$ ,  $x_* = 0.80$ , and  $x^* = 1.2$ . Choice of  $\beta = 0.02$  really flattens the function!

The value  $x_l$  at which  $f_3(x)$  is matched to  $f_2(x)$  must be less than  $x^*$  but great enough to allow smooth pasting of a function with negative slope at  $x_l$ . Initial conditions for the rate functions in figure B.2 and figure 19 are  $x_0 = 0.805$ ,  $x_l = 1.18$ , and  $x^2 = 2.0$ , and  $\kappa = 0.01$ .

<sup>19</sup> If  $x^*$  and  $x_*$  are chosen to be equidistant from the peak at 1.0, then as  $x_l$  is greater than 1.0,  $U_3 = x^* + x_* - 2x_l < 0$  so that  $\gamma_2$  is positive.



## Appendix D

### Method for Recovering Price and Sowers Data

This appendix presents a simple statistical model based on Arrhenius' Law and a description of how it is used to extract data from Price and Sowers (2004) figure 1 (our figure 20).

#### Data Generating Process Models

To account for dependence of the rate of methane production at the seafloor on variables in addition to temperature, expand the domain of  $A_{SF}(T_{SF}(WD))$  to include other explanatory variables—water flux, for example. Let  $\mathbf{g}$  denote a realization of these “other variables” and define the rate of methane productivity at seafloor to be a function of both  $\mathbf{g}$  and  $T_{SF}(WD)$ .

Then an Arrhenius-like data generating process model for  $Y(T, \mathbf{g}) =$  Methane Production Rate at Temperature  $T$ , given  $T_{SF}(WD)$  and  $\mathbf{g}$  is:

$$(D.1) \quad Y(T, \mathbf{g}) = A_{SF}(T_{SF}(WD), \mathbf{g}) \times \exp\{\phi \times (T - T_{SF}(WD))\} \times \delta_k$$

Here  $\delta_k, k = 1, \dots, n, \dots$  are mutually independent positive random variables with possibly different means and variances; probability distributions of the  $\delta_k$ s may depend on characteristics of the geologic environment. While some observable explanatory variables other than (observable) temperature can be modeled, others remain “hidden” in the  $\delta_k$ s. That is, properties of probability distributions of the  $\delta_k$ s may depend on these hidden variables.

In particular, initial productivity at the seafloor is a function of the mix of archaea found in that environment. “Sorting out” the contribution to productivity of individual archaea is a formidable task. We assume here that Price and Sowers data measures an “aggregate”  $A_{SF}(T_{SF}(WD))$  in each particular geological environment examined.

We begin with a data generating process model for data from a study of methane productivity in one specific geological environment. This is a simple benchmark model useful for making inferences about methane production rates from each of the “Maintenance” studies appearing in Price and Sowers. Occam's Razor suggests that, without considerably more insight into how these studies were conducted, how data were gathered and what statistical methods were applied, we keep our choice of model simple.

#### Data Generating Process for a Single Study

By a “single study” we mean a dataset gathered from one particular geological environment. If we adopt Eq. (D.1) as a model of observations and know  $T_{SF}(WD)$  with certainty, then the intercept term  $A_0 \equiv A_{SF}(T_{SF}(WD), \mathbf{g})$  and functional form of and parameters of the probability distributions of error terms  $\delta_k, K=1, \dots$  are the only remaining features of Eq. (D.1) not known with certainty.

Suppose that, for a given study, error terms  $\delta_k, k = 1, \dots$  possess a common probability distribution. Multiply both sides of Eq. (D.1) by  $\exp\{\delta_k (T(WD) - T)\}$  and set the observable quantity

$$(D.2) \quad Z_k \equiv Y_k \times \exp\{\phi \times (T(WD) - T)\} = A_{SF}(T_{SF}(WD), \mathbf{g}) \times \Delta_k$$

The rate  $Y_k$  is now scaled to be temperature independent, and the right hand side is a (positive) quantity  $A_0$  multiplied by an uncertain error term  $\Delta_k > 0$ .

To complete specification of Eq. (D.2) as a data generating process model, we must identify the composition of  $\mathbf{g}$  and describe how  $A_0$  depends on  $(T_{SF}(WD))$  and  $\mathbf{g}$ . Should we assume, for example, that all explanatory

variables composing  $\mathbf{g}$  are fixed and common for all observations in one particular study? Or that some components of  $\mathbf{g}$  can vary from observation to observation? Which elements of  $\mathbf{g}$  are observable?

Our initial treatment of Price and Sowers' "Maintenance" data assumes that, for each individual "Maintenance" data study, explanatory variables  $\mathbf{g}$  and water bottom temperature ( $T_{SF}(WD)$ ) are fixed and common to all of this study's measurements.<sup>20</sup>

We also assume that, for a given study, the random variables  $\Delta_k$  are independent and possess common means  $M = 1.0$  and, variances  $Var(\Delta_k) = V$ . Then seafloor temperature adjusted rate measurements  $Z_1, \dots, Z_k, \dots, Z_n$  have a common mean  $E(Z_k) = A_0$  and a common variance  $Var(Z_k) = A_0^2 \times V$ . If a study yields temperature adjusted measurements  $Z_1, \dots, Z_k, \dots, Z_n$ , the average  $\hat{M} = \frac{1}{n} \sum_{k=1}^n Z_k$  is a simple unbiased estimator of  $A_0$ ; given

$A_0$ , an unbiased variance estimator for  $Var(\Delta_k)$  is  $S^2 = \frac{1}{n-1} \sum_{k=1}^n (Z_k - \bar{Z})^2 / A_0^2$ .<sup>21</sup>

### Price and Sowers' Graphical Data

Each individual Maintenance Data point in Price and Sowers' graph represents an "experiment" or "study". Figure 20 equips each "experimental" point with an "error bar", so in principle, calculation of an estimator of the variance of  $\Delta_k$  can be imputed from this graphical display. If detailed numerical data for each "experiment" become available we can, as stated earlier, do a meta-analysis of the collection of Maintenance Data experiments appearing in their figure 1, which would put estimates of the intercept term on more solid ground. However, our only source of data at this time is Price and Sowers graph. We impute summary statistics of individual experiments from it.

Accurate recovery of each relevant data point and its associated measurement error is a problem. While we reviewed most of the articles Price and Sowers used to guide their calculation of metabolic rates, it is difficult or impossible to reconstruct exactly what they did to arrive at figure 20 error bars. The data in Table D.1 is extrapolated from figure 20 points and error bars.

**Table D.1**  
**Maintenance Data Recovered from Figure 20**

Label	Temperature (°C)	Metabolic Rate	Confidence Interval
A <sub>2</sub>	28	$8 \times 10^{-4}$	$(2 \times 10^{-4}, 6 \times 10^{-4})$
A <sub>1</sub>	13	$9 \times 10^{-5}$	$(2 \times 10^{-5}, 8 \times 10^{-5})$
B <sub>2</sub>	2	$8 \times 10^{-5}$	$(5 \times 10^{-5}, 3 \times 10^{-4})$
E <sub>1</sub>	15	$2 \times 10^{-5}$	$(8 \times 10^{-6}, 3 \times 10^{-5})$
B <sub>1</sub>	2	$4 \times 10^{-6}$	$(10^{-6}, 10^{-5})$
E <sub>2</sub>	14	$4 \times 10^{-6}$	$(10^{-6}, 6 \times 10^{-6})$
E <sub>3</sub>	15	$2 \times 10^{-6}$	$(8.5 \times 10^{-7}, 3 \times 10^{-6})$
C	-15	$8 \times 10^{-8}$	$(10^{-8}, 2 \times 10^{-7})$

<sup>20</sup> However, both  $T_{SF}(WD)$  and  $\mathbf{g}$  may vary from study to study. Each individual study possesses a data generating process model, like that in Eqs. (D.1) and (D.2) for a restricted temperature range.

<sup>21</sup>  $S^2 / \bar{Z}^2$  is not an unbiased estimator of  $Var(\Delta_k)$ .



**Estimation of  $A_0 = A_{SF}(T_{SF}(WD))$**

Each metabolic rate in Column 3 of Table D.1 is to be interpreted as the *mean* of a set of measurements of metabolic rates made in a *given study*. Rates in Column 3 are not adjusted to seafloor temperature; if we assume that seafloor temperature is  $T = 2\text{ }^\circ\text{C}$  and that the data generating process model (Eqs. (D.1) and (D.2)) obtains, a simple average of

$$(D.3) \quad \begin{aligned} & \text{Mean Metabolic Rate} \times \exp\{\phi \times (T(WD) - T)\} \\ & = \text{Mean Mean Metabolic Rate} \times \exp\{0.0693 \times (2 - T)\} \end{aligned}$$

is an unbiased estimator of  $A_0$ . Values of seafloor adjusted mean metabolic rates  $\hat{M}^{(j)}$   $j = 1, \dots, 8$  are shown in Column 4 of Table D.2.

**Table D.2**  
**Metabolic Rate Mean Values Adjusted to Seafloor Temperature**

Label	Temperature ( $^\circ\text{C}$ )	Metabolic Rate ( $10^{-6}$ Units)	Adjusted to Seafloor Temperature ( $10^{-6}$ Units)
A <sub>2</sub>	28	800	131.95
A <sub>1</sub>	13	90	41.90
B <sub>2</sub>	2	80	80.00
E <sub>1</sub>	15	20	8.12
B <sub>1</sub>	2	4	4.00
E <sub>2</sub>	14	4	1.74
E <sub>3</sub>	15	2	0.81
C	-15	0.08	0.26

Although data point C is for  $-15\text{ }^\circ\text{C}$ , well below seafloor temperature, we include it to show how one point with rather large leverage can influence sample statistics. These point estimates are measured in the same units as the vertical axis in Price and Sowers' graph.

*Metabolic rates adjusted to seafloor temperatures in Table D.2 vary by over two orders of magnitude. This suggests that explanatory variables other than temperature affect these rates and that a model based on temperature alone is not likely to be robust.*

A rough approximation to variances of mean adjusted metabolic rates supports this conclusion: variances of individual estimators  $\hat{M}^{(j)}$  are small relative to the spread of values of these estimators. That is, within-estimator variability is small relative to between-estimator variability.

**Capturing Uncertainty About  $A_0 \equiv A_{SF}(T_{SF}(WD), \mathbf{g})$**

The average of methane production rates - scaled to seafloor temperatures - for Maintenance data studies appearing as data points in figure 20 from Price and Sowers is, as stated above,  $34 \times 10^{-6}$  in Price and Sowers' units. Point C in figure 20 represents a study in which data were gathered at approximately  $-15\text{ }^\circ\text{C}$ , far below the approximately  $2\text{ }^\circ\text{C}$  at seafloor in the GOM. If we drop this data point the average is  $38.4 \times 10^{-6}$  — a 13-percent increase.

We discuss below how to use figure 20 to impute point estimates of the variance of the mean value of an individual study and a point estimate of the variance of individual study means.

These point estimates are used to assign values to parameters of a lognormal distribution which, in turn, is employed in the Monte Carlo routine to represent uncertainty about  $A_{SF}(T_{SF}(WD), \mathbf{g})$ .

If the confidence intervals shown in column 4 of Table D.1 are indeed 95-percent confidence intervals about a sample mean metabolic rate at a given temperature we can compute an estimate of the variance (or standard deviation) of each sample mean at a given temperature. To this end, we conjecture that Price and Sowers assume measurements at a given temperature are normally distributed with common mean and variance. If so, then the width of a typical confidence interval is about  $2 \times 1.96 = 3.92$  times the *sample* standard deviation.<sup>22</sup>

Table D.3 below displays confidence interval widths extrapolated from figure 20.

**Table D.3**  
**Standard Deviations Imputed from Individual Study CI WIDTHS**

Label	Unadjusted Metabolic Rates	Unadjusted Confidence Intervals	Unadjusted Widths	Standard Deviation of Sample Means
A <sub>2</sub>	$8 \times 10^{-4}$	$(2 \times 10^{-4}, 6 \times 10^{-4})$	$4 \times 10^{-4}$	$1.02 \times 10^{-4}$
A <sub>1</sub>	$9 \times 10^{-5}$	$(2 \times 10^{-5}, 8 \times 10^{-5})$	$6 \times 10^{-5}$	$1.53 \times 10^{-5}$
B <sub>2</sub>	$8 \times 10^{-5}$	$(5 \times 10^{-5}, 3 \times 10^{-4})$	$25 \times 10^{-5}$	$6.38 \times 10^{-5}$
E <sub>1</sub>	$2 \times 10^{-5}$	$(8 \times 10^{-6}, 3 \times 10^{-5})$	$22 \times 10^{-6}$	$5.61 \times 10^{-4}$
B <sub>1</sub>	$4 \times 10^{-6}$	$(10^{-6}, 10^{-5})$	$9 \times 10^{-6}$	$3.00 \times 10^{-8}$
E <sub>2</sub>	$4 \times 10^{-6}$	$(10^{-6}, 6 \times 10^{-6})$	$6 \times 10^{-6}$	$1.53 \times 10^{-6}$
E <sub>3</sub>	$2 \times 10^{-6}$	$(8.5 \times 10^{-7}, 3 \times 10^{-6})$	$2.15 \times 10^{-6}$	$5.49 \times 10^{-5}$
C	$8 \times 10^{-8}$	$(10^{-8}, 2 \times 10^{-7})$	$19 \times 10^{-8}$	$5.0 \times 10^{-8}$

The standard deviations of individual data points in Column 5 of Table D.3, which are in fact either the mean of a sample or, in one case a regression line are not adjusted to seafloor temperatures. We wish to emphasize that

the formula  $\frac{\nu}{\sqrt{n}} \cong \frac{Width}{3.92}$  yields a point estimate of the standard deviation  $\frac{\nu}{n}$  of a *sample mean composed of n observations*. Sample sizes of studies Price and Sowers use to construct figure 19 are not available; sample sizes may vary by a large amount from study to study.

*Once again, the estimates presented below are based on an eyeball interpolation of Price and Sowers graphical presentation.* Notice, for example, that the confidence intervals shown above are not symmetric about their midpoints.

Table D.4 below shows standard deviations of sample means of each study adjusted to seafloor temperature using Eq. (D.3).

---

<sup>22</sup> If X is Normal with mean  $\mu$  and variance  $\nu^2$  then  $\bar{X} = \frac{1}{n} \sum_{i=1}^n X_i$  has mean  $\mu$  and variance  $\frac{\nu^2}{n}$ . A 95% confidence interval is  $(\bar{X} - 1.96 \frac{\nu}{\sqrt{n}}, \bar{X} + 1.96 \frac{\nu}{\sqrt{n}})$ . Here  $\bar{X}$  is the mean of our interpolation of metabolic rates from Price & Sowers' graph--shown in Column 3 above-- and  $2 \times 1.96 \frac{\nu}{\sqrt{n}}$  is the confidence interval width so that the sample standard deviation  $\frac{\nu}{\sqrt{n}} \cong \frac{Width}{3.92}$ .

**Table D.4**  
**Standard Deviations of Sample Means Adjusted to Seafloor Temperature**

Label	Unadjusted Metabolic Rates	Temperature	Unadjusted Standard Deviations of Sample Means (10 <sup>-6</sup> P&S Units)	Temperature Adjusted Standard Deviations of Sample Means (10 <sup>-6</sup> P&S Units)
A <sub>2</sub>	8×10 <sup>-4</sup>	28	102	0.17
A <sub>1</sub>	9×10 <sup>-5</sup>	13	15.3	0.47
B <sub>2</sub>	8×10 <sup>-5</sup>	2	63.8	1.00
E <sub>1</sub>	2×10 <sup>-5</sup>	15	561	0.41
B <sub>1</sub>	4×10 <sup>-6</sup>	2	0.03	1.00
E <sub>2</sub>	4×10 <sup>-6</sup>	14	1.53	0.44
E <sub>3</sub>	2×10 <sup>-6</sup>	15	54.9	0.41
C	8×10 <sup>-8</sup>	-15	0.05	3.23

A comparison of standard deviations in Table D.5 with those in Table D.4 makes it clear that variation about the mean of seafloor temperature and adjusted methane production rates within a given study is much smaller for all eight studies than variation of this rate among studies.

**Table D.5**  
**Between Studies Summary Statistics for Temperature Adjusted Metabolic Rates (10<sup>-6</sup> Units)**

Metabolic Rate	Unadjusted	Adjusted to Seafloor Temp
Average with All Observations	125	33.6
Average w/0 C	143	38.4
Standard deviation with all Observations	275	48.8
Standard deviation w/0 C	292	50.6

**Assignment of Lognormal Distribution to  $A_0 \equiv A_{SF}(T_{SF}(WD), g)$**

As stated earlier, we shall assign a lognormal distribution to  $A_0$ . Parameters are chosen so that  $A_0$  has mean value 38.4 and variance 50.6<sup>2</sup>. With  $A_0$  measured in 10<sup>-6</sup> units of methane productivity, and  $A_0 \sim N(\mu\sigma^2)$ , this mean and variance imply  $\mu = 1.61$  and  $\sigma^2 = 4.08$ . These two key parameters are in the units Price and Sowers use. For the generation model, they are converted in the manner described in Appendix E.

**Permeability Ratios Used to Rescale Seafloor Temperature Productivity**

Use the sand/shale ratio developed by Shedd and Hunt for each cell to calculate the permeability ratio.

$$(D.4) \quad \frac{Sandperm(d) \times FractionSand(d) + Shaleperm(d) \times FractionShale(d)}{Sandperm(WD) \times FractionSand(WD) + Shaleperm(WD) \times FractionShale(WD)}$$

Here  $Sandperm(d)$  [ $Shaleperm$ ] denotes sand [shale] permeability at depth  $d$  in meters. Let  $g'$  be composed of explanatory variables other than those appearing in the product of seafloor temperature methane productivity rate and the ratio  $\rho(Perm)$ . Then

$$(D.5) \quad Y_k(T, \rho(Perm), \mathbf{g}') = \rho(Perm) \times A_{SF}(T_{SF}(WD), \mathbf{g}') \times \exp\{\phi \times (T - T_{SF}(WD))\} \times \delta_k$$

for temperatures in the domain for which Arrhenius' Law holds.

Computation of methane production rate in a sedimentary interval at a point in geological time is done using of Eqs. (D.4) and the modified form of Arrhenius' Law described earlier. Some elements of Eqs. (D.4) and (D.5) are directly measurable and assumed to be known with certainty; others are not known with certainty and so must be assigned probability distributions to render the model well posed and computable. To set the stage for a detailed discussion of how the data generating process is used to Monte Carlo values of methane productivity, here is a bird's eye overview of how uncertainty about the rate of methane production  $A_0 = A_{SF}(T_{SF}(WD), \mathbf{g}')$  is incorporated into Monte Carlo simulation of methane productivity:

- The rate of methane production of a sedimentary unit at a point in geological time at seafloor temperature is not known with certainty. We adopt the average of methane production rates—scaled to seafloor temperature—of Price and Sowers Maintenance data set as the mean of  $A_0$  and assign a lognormal distribution to it as described above. Recall that the variance of  $A_0$  is chosen to reflect the more than two orders of magnitude variation among the means of Maintenance data studies appearing in figure 20 (see Table D.3).
- The sedimentary section in each cell (thickness from seafloor to top of salt) is divided into five stratigraphic units. The ratio in  $\rho(Perm)$  in Eq. (D.4) is computed for each stratigraphic unit at each of five geologic time periods. In contrast to the value of  $A_0$  - which is held fixed for all stratum/time steps in a Monte Carlo trial within a cell -  $\rho(Perm)$  varies with each stratum/time step.
- Values of the rate of methane productivity  $Y_k(T, \rho(Perm), \mathbf{g}')$  in Eq. (D.4) are generated for each sedimentary unit at each of five periods of geologic time by first, generating a Monte Carloed value of  $A_0 = A_{SF}(T_{SF}(WD), \mathbf{g}')$ , then Monte Carloing a value of  $\rho(Perm)$ , followed by generation of a value of the residual error term  $\delta_k$ .
- The ratio in Eq. (D.4) is, at each stratum/time step, the product of the ratio of sediment permeability mixtures at the midpoint depth of the unit to the estimated permeability at the seafloor - multiplied by seafloor productivity. It varies at each stratum/time step.

## Appendix E

### Conversion of Price and Sowers' Units to Units Used in Generation Model

This Appendix documents how data on methanogenic productivity from Price and Sowers' article are converted to units used in the generation model. The sample mean and sample variance of Price and Sowers' Maintenance Data are taken to be the mean and variance of a lognormal distribution of seafloor productivity,  $A_{SF}$ , which is, in turn, used to scale the methane productivity rate function shown in figure 18. Appendix D explains how this sample is used to compute values of parameters for a lognormal distribution, transforming Price and Sowers' units to those used in this study.

The conversion to generation model units is done as follows:

1. From Appendix D, the mean (M) of the lognormal distribution on  $A_{SF}$  is  $3.8 \times 10^{-5}$ , and the standard deviation (S) of the distribution is  $5.06 \times 10^{-5}$ . Both of these values are in Price and Sowers units – “g C/g C/h”.
2. Price and Sowers' units are interpreted to mean “grams of carbon in methane generated per gram of carbon in methanogenic archaea cells per hour.”
3. Dr. Colwell translates Price and Sowers' units (“g C/g C/h”) to femtomoles of methane generated per cell per day (“fmol CH<sub>4</sub>/cell/day”) of 200 g C/g C/h to 1 fmol CH<sub>4</sub>/cell/day. In his units, M =  $7.6 \times 10^{-3}$  fmol CH<sub>4</sub>/cell/day ( $3.8 \times 10^{-5} \times 200$ ), and S =  $1.01 \times 10^{-2}$  fmol CH<sub>4</sub>/cell/day ( $5.06 \times 10^{-5} \times 200$ ).
4. There are  $1 \times 10^{15}$  femtomoles in 1 mole. Therefore, M =  $7.6 \times 10^{-18}$  moles CH<sub>4</sub>/cell/day ( $7.6 \times 10^{-3} \times 10^{-15}$ ), and S =  $1.01 \times 10^{-17}$  moles CH<sub>4</sub>/cell/day ( $1.01 \times 10^{-2} \times 10^{-15}$ ).
5. The density of microorganisms is assumed to be  $1.48 \times 10^9$  cells per cubic centimeter (cm<sup>3</sup>) of sediment at the seafloor. This value is the median of the data provided in Table E.1 below.

**Table E.1**  
**Density of Microorganism Cells in Sediments**

Microorganism Density (cells/cc)	Source
$1.05 \times 10^9$	Parkes et al., 1990
$5.94 \times 10^9 - 4.32 \times 10^{11}$	Lochte and Turley, 1986
$3.24 \times 10^{10}$	Rice et al., 1986
$1.9 \times 10^9$	Parkes et al., 1994

6. Based on conversations with Dr. Colwell and others, we assume that 1 percent of the microorganisms in seafloor sediments are methanogens. This is derived from an estimate of 10 percent of microorganisms on the seafloor belonging to the archaeal group and perhaps 10 percent of that number being methanogens. Then the density of methanogens in seafloor sediments is  $1.48 \times 10^7$  methanogen cells/cm<sup>3</sup> sediment ( $1.48 \times 10^9 \times 0.01$ ).
7. Multiplication of the median density of cells of methanogens per cubic centimeter of sediment times the value of methane production in moles/cell/day yields M =  $1.12 \times 10^{-10}$  moles of methane/cm<sup>3</sup> of sediment/day ( $7.6 \times 10^{-18} \times 1.48 \times 10^7$ ) and S =  $1.49 \times 10^{-10}$  moles of methane/cm<sup>3</sup> of sediment/day ( $1.01 \times 10^{-17} \times 1.48 \times 10^7$ ). Three estimates from the literature are shown in Table E.2. The mean value (M) is close to that of Parkes.

**Table E.2**  
**Productivity of Methanogens in Sediments**

Methanogenic Productivity (moles CH <sub>4</sub> /cm <sup>3</sup> sediment/day)	Source
1.8 x 10 <sup>-10</sup>	Parkes et al., 1990
0 – 2.8 x 10 <sup>-11</sup>	Senior et al., 1982
1 x 10 <sup>-11</sup> – 2 x 10 <sup>-8</sup>	Lein et al., 1981

8. The mass of a mole of methane is 16 grams. Conversion of productivity in moles of methane to grams yields  $M = 1.79 \times 10^{-9}$  grams of methane/cm<sup>3</sup> sediment/day ( $1.12 \times 10^{-10} \times 16$ ) and  $S = 2.38 \times 10^{-9}$  grams of methane/cm<sup>3</sup> sediment/day ( $1.49 \times 10^{-10} \times 16$ ).
9. There are  $1 \times 10^6$  cubic centimeters in one cubic meter. Conversion of production in cubic centimeters to cubic meters of sediment yields  $M = 1.78 \times 10^{-3}$  grams of methane/m<sup>3</sup> sediment/day ( $1.78 \times 10^{-9} \times 10^6$ ) and  $S = 2.38 \times 10^{-3}$  grams of methane/m<sup>3</sup> sediment/day ( $2.38 \times 10^{-9} \times 10^6$ ).
10. There are  $3.65 \times 10^8$  days per million years. Conversion of production per day to production per million years yields  $M = 6.5 \times 10^5$  grams of methane/m<sup>3</sup> sediment/million years ( $1.78 \times 10^{-3} \times 3.65 \times 10^8$ ) and  $S = 8.69 \times 10^5$  grams of methane/m<sup>3</sup> sediment/million years ( $2.38 \times 10^{-3} \times 3.65 \times 10^8$ ).

Other than the assumptions above, this conversion requires the following notes:

1. The unit-converted rate,  $A_{SF}$ , from Price and Sowers' units to grams methane/m<sup>3</sup> sediment/million years assumes that  $A_{SF}$  is linear in total organic carbon (TOC).
2.  $A_{SF}$  is measured in terms of sediments with TOC normalized to 1 (i.e., units of 1%).
3. A change from Price and Sowers' units to grams methane/m<sup>3</sup> sediment/million years multiplicatively rescales sample statistics M and S and adds a constant to the parameter  $\mu$  of the lognormal distribution assigned to  $A_{SF}$ .
4. M and S are scaled to production per 1,000,000 years, so that they are congruent with the scale of other parameters used in the generation model. In fact, if the mean rate, M of productivity *at the seafloor surface*, persisted for 1,000,000 years and sediment TOC = 1percent, methanogens would produce a mass of methane roughly 100 times greater than the mass of organic carbon in the sediments. This will not happen in the model because of two reasons:
  - a. The rate of productivity at the seafloor ( $A_{SF}$ ) is the starting point for calculation of productivity which is then scaled by the ratio of the permeability of sediments at depth to the permeability at the seafloor. This is typically a reduction greater than a factor of 100 for depths over which methanogenesis occurs.
  - b. When cumulative methane production reaches the asymptotic limit of conversion of organic carbon to methane (a mean of 18% of organic carbon by mass in the case of the GOM), the model terminates methanogenesis.

# Appendix F

## Calculating GOM Accumulation Density

Appendix F contains a description of an MMS effort that was led by engineers and geoscientists in the Resource and Economic Analysis Unit, Office of Resource Evaluation, Gulf of Mexico Region. The primary goal of the effort was to define the spatial accumulation density of hydrocarbon pools on the OCS shelf for the purpose of supporting the MMS conventional oil and gas assessment. The results have been adopted as a proxy to migration and trapping efficiency for the Gulf of Mexico (GOM) gas hydrate assessment model.

### Background

The MMS maintains an inventory of over 60 geologic plays that serve as the foundation for our comprehensive play-based approach to resource assessment and analysis of hydrocarbon potential. A major strength of the play-based approach is that it maintains a strong relationship between information derived from oil and gas exploration activities and the geologic model employed by assessment teams. A play is defined as a group of pools that share a common history of hydrocarbon generation, migration, reservoir development, and entrapment. Extensive effort is involved in developing play models, delineating the geographic limits of each play, and compiling data on critical geologic and reservoir engineering parameters. These parameters are critical inputs in the determination of the total quantities of discovered and undiscovered resources in each play.

### Methodology

The MMS believes that the best measure of actual accumulation density using the MMS plays is found in the most mature plays, i.e. those that have at least 75 percent of resources classified as discovered. Using this maturity criteria, 18 GOM unaggregated shelf plays and 9 aggregated shelf plays were incorporated into this study (see Table 6 and Table 7 of chapter II, respectively). Aggregated plays comprise several shorter time units summed to the Series level, such as the Upper, Middle, and Lower Pleistocene Progradational plays aggregated to become the Pleistocene Progradational play.

The group of hydrocarbon pools that comprise an MMS play are themselves made up of many *Formation Sands*, which are uniquely identified in each MMS-designated oil or gas field. A pool often contains many *Formation Sands* that are stacked vertically with varying degrees of lateral overlap. The accumulation density for each play is expressed as a percentage where the numerator equals the productive area of the play and the denominator equals the total area of the play. The productive area is determined by summing the area (acres) of all *Formation Sands* within a play, and total play area is defined as the geologic play limit.

### Results

On most occasions, the accumulation density of the aggregated plays is greater than the unaggregated because the Play Area (denominator) is often the same, while the Formation Sand Area (numerator) sum tends to increase. Results for both data sets range from less than 1 percent to just over 7 percent. These results were made available to those involved with the development of the MMS hydrate assessment model methodology to be incorporated as needed.





# Appendix G

## Operating Instructions and Description of Programs, V 3.38 Jack Schuenemeyer & Ray Faith (9/21/2007)

### Introduction

The first section of this report describes input and output files and operating instructions for the Gulf of Mexico (GOM) gas hydrate assessment model. Mathematical details of specific sub-models are described elsewhere in this report. This model has been tested and run on the GOM, and results analyzed for reasonableness by geologists and other subject matter experts. Additional sensitivity analysis is required and some of the data used to formulate models may be updated. The authors welcome any comments, suggestions and corrections. We recommend that the user read all of the operating instructions before beginning a run.

The second section of this report is a brief overview of the FORTRAN model and programs.

### Installing R

If R (an open source code statistical and graphics language) is installed on your computer, graphics and summary statistics will be generated once cell computations are completed. To install R on your computer:

1. From the internet go to [www.r-project.org](http://www.r-project.org)
2. Left click on Download CRAN (left side of screen)
3. Scroll down to USA and left click on a USA site
4. In Downloads and Install you will see Linux, MacOS X and Windows. Left click on your operating system.
5. In R for Windows (for example) click on base.
6. You will see R-2.5.1 for Windows (or the current release number)
7. Left click on README.R-2.5.1 to see installation instructions
8. After reviewing instructions click on R-2.5.1-win32.exe
9. In the file download window, click on RUN or SAVE (the download on this release is about 29MB).
10. For the remaining steps (by the Windows installer) choose defaults.
11. Return to the R homepage for R manuals if needed.

### Operating Instructions

These instructions present input files, run time instruction, output files and compilation.

#### Input Files

Prior to making a run, two input files and the executable code need to be in place, an Excel file called Setup.xls, which contains parameter information, and a text file containing the input data by cell.

12. Setup.xls – Model input specification and model parameters. This file contains Visual Basic code, which allows the user to execute the model by left clicking on the RUN button. An output file will be produced showing values of parameters and other settings. The Setup.xls file consists of two parts.
  - a. User changes. These are changes the user many need or wish to make prior to any run.
    - (i) Study Name. A description name of the study. This will be the name of the Excel (.xls) file containing the results.
    - (ii) Input Data File Name. Name and location of the input cell data. In the example (Display 1) the file name is GBdata\_short.txt. Note that this must be a text (.txt) file.

It can be created as an Excel or .csv file but then must be saved *as a tab-delimited text file*. GardenBanks is the folder containing the input data file.

(iii) Ntrials (The number of trials) is currently set at 1,000. If the user desires additional accuracy at the more extreme percentiles, this number may be increased up to a maximum of 4,000.

(iv) CellSize is the linear size of a square cell in feet. It is currently set at 5,000 feet.

(v) The next four lines are used to save detailed cell by trial output. These files contain results for individual cells and trials. They are: charge in trillion cubic meters (tcm), net hydrate stability zone (HSZ) thickness (meters), concentration (fraction), and volume (tcm). They may be extremely large. For example, if there are 50,000 cells in the Input Data file and 1,000 trials, then 50,000,000 records would be written. A file description is presented in Display 2, Results. To generate these files change the 0 to 1 in SaveChargeCT, SaveNetHSZCT, SaveConcenCT and/or SaveVolumeCT.

b. The parameter estimates were derived from scientific literature, expert judgment and analysis of data. They are based on the best available information for the GOM. They can be changed by the user, but caution must be used including a review of the scientific methodology presented elsewhere in this report.

13. InputData.txt – the input data for each cell of each basin in the study. *The name of this file and the Input Data File Name in Setup.xls must be identical.* The input data is by row. Each row is a cell and consists of the following variables:

- a. an area or region identification (AreaID),
- b. latitude (Lat), longitude (Lon), which are cell mid-points,
- c. sand percent (SandPerc),
- d. water depth in meters (WD),
- e. vertical depth in meters to top of basement (Salt),
- f. anomaly,
- g. basin identification (BasinID),
- h. curvature (Curve), and
- i. vertical migration (Vertical), an indicator variable (0 = off-anomaly, migration mixing ratio (MigRat) specified in Setup.xls is used, 1 = seismic anomaly, migration is completely vertical).

A portion of a sample data file is shown below. Each row represents a cell.

Area ID	Lat	Long	SandPerc	WD	Salt	Anomaly	Basin ID	Curve	Vertical
TS02	27.1266	-92.67472	5	1203	256	0	2	0	0
TS02	27.5534	-92.43088	40	892	3589	0	2	0	0
TS02	27.5534	-92.27848	30	949	5808	0	2	0	0
TS02	27.5686	-92.27848	30	904	6078	0	2	0	0
TS02	27.5838	-92.29372	29	863	6645	0	2	0	0

Computation of the curvature (Curve) of the basement surface is done in ArcGIS with the Curvature tool in the Spatial Analyst extension.

Display 1 Setup.xls

Run Model

Parameter	Type	Value1	Value2	Value3	Value4	Description
Study Name		Garden Banks				Title for this study
Input Data File Name		Garden Banks\GBData_short.txt				Input Data Set pathname
Ntrials	Constant	1,000				Number of trials (0<Ntrials<2,000)
Cellsize	Constant	5,000				Linear size of cell (in feet)
SaveChargeCT	Constant	0				Save Charge Cell by Trial Output (0=No, 1=Yes)
SaveNetHSZCT	Constant	0				Save NetHSZ Cell by Trial Output (0=No, 1=Yes)
SaveConcernCT	Constant	0				Save Concentration Cell by Trial Output (0=No, 1=Yes)
SaveVolume CT	Constant	1				Save Volume Cell by Trial Output (0=No, 1=Yes)
GeoThermal Gradient	Beta	1.43	2.66	14	76	Geothermal Gradient (alpha, beta, shift, scale)
BottomTempCoeffs	Constant	18.23	-0.003136	4.101		Temp (defC) = a*exp(b*Depth(m)) + c + Error
BottomTempError	Normal	0	0.4425			Error term in above (Note: only standard deviation is used)
Zeta	Normal	1.23	0.09			Local Salt – scale (mean, std dev)
Nu	Normal	0.03	0.003			Local Salt – shale (mean, std dev)
Mu	Normal	214	58.8			Hydrate stability temp – shift (mean, std dev)
Pi	Normal	0.11	0.01			Hydrate stability temp – scale (mean, std dev)
GammaA	Beta	2.5	0.3	44.4	1	Phase stability eqns, w/anomalies
DeltaA	Beta	0.3	2.5	8.4	2	Phase stability eqns, w/anomalies
GammaNo	Beta	2.5	0.3	49.1	1	Phase stability eqns, w/anomalies
DeltaNo	Beta	0.3	2.5	8.8	2	Phase stability eqns, w/anomalies
P1stMy	Gamma	1.638	1			Total Thickness of Sediment – Pleistocene (shape, scale)
PlioMy	Gamma	1.5	1			Total Thickness of Sediment – Pliocene (shape, scale)
UMMy	Gamma	0.976	1			Total Thickness of Sediment – Upper Miocene (shape, scale)
MMMy	Gamma	0.976	1			Total Thickness of Sediment – Middle Miocene (shape, scale)
LMMMy	Gamma	1.133	1			Total Thickness of Sediment – Lower Miocene (shape, scale)
SandPermCoeffs	Constant	10.85	-0.000258			Perm(md) – (Lambda * [a + b * Depth(m)] = Error] + 1)^(1/Lambda)
Lambda	Constant	0.153				Lambda in Sand Permeability Equation
SandPermError	Normal	0	2.541			Error term in above (Note: only standard deviation is used)
Omega	Normal	0.84	0.08			Shale porosity as fn of depth (mean, std dev)
Tau	Normal	-0.125	0.01			Shale porosity as fn of depth (mean, std dev)
Omicron	Normal	0.0037	0.00037			Shale permeability as fn of depth (mean, std dev)
Chi	Normal	1.7	0.17			Shale permeability as fn of depth (mean, std dev)
TOC	Weibull	3.3517	0.94			Total Organic Carbon
OmtQual	Weibull	2.483	131			Asymptotic conversion efficiency (shape, scale)
MigRat	Normal	0.6	0.1			Migration mixing ration (mean, std dev)
SSFracVoid	Triangular	0	0.05	0.15		Anomaly Fracture Void – Sand (min, most likely, max)
SHFracVoid	Triangular	0	0.05	0.15		Anomaly Fracture Void – Shale (min, most likely, max)
SS1Coef	Constant	0.5583				Porosity = SS1Coef * exp(SS2Coef * Depth(m)) + Error
SS2Coef	Constant	-0.0008932				Shallow sand porosity (Note: must be negative)
SSPorError	Normal	0	0.05839			Error term in above (Note: only standard deviation is used)
SH1Coef	Constant	0.7196				Shallow shale porosity (poly regression model)
SH2Coef	Constant	-0.00081				Shallow shale porosity
SH3Coef	Constant	0.0000036				Shallow shale porosity
ShPorError	Normal	0	0.015			Shallow sand porosity error (Note: only standard deviation is used)
FracSat	Triangular	70	80	90		% saturation of fracture void volumes in anomalies only – sand/shale (min, most likely, max)
SandSat	Triangular	40	60	90		% saturation mix pore volumes – sand (min, most likely, max)
SHSat	Triangular	0	10	20		% saturation mix pore volumes – shale (min, most likely, max)
SedDensity	Constant	2.1				Sediment Density at seafloor (in g/cc)
MigrationEff	Hard	1	0			Migration Efficiency (factor in final volume)(0 < MigrationEff <=1 )
TrappingEff	Wired	1	0			Trapping Efficiency (factor in final volume)(0 < TrappingEff <= 1)
FormationVolFactor	Beta	5	1.6	139	33	Formation Volume Factor 139 < fvf < 172

Distribution Parameters				
Normal	mean	standard deviation		
Beta	alpha	beta	location	scale
Gamma	shape	scale		
Weibull	shape	scale		
Triangular	minimum value	peak value	maximum value	

### Prior to Running the Model

1. If the input data are first constructed as an Excel file, the user needs to make the Excel columns wide enough so that, when the values are written as a text file, they don't lose digits of accuracy. Leave the first (label) line in when saving the file.
2. The InputData.txt must be sorted by BasinID.
3. The Setup.xls and GOM.exe must be in the same directory. Output will also appear in this directory. The InputData.txt file may be in another directory; however, the address must be specified in the Input File Name in Setup.xls.
4. R must be installed if graphic output and summary statistics are desired.
5. Graphics output will be placed in the main output file, which will have the name specified in Study Name (Display 1); however, individual jpeg files are also written with generic names. These files must be renamed or copied to another directory to be saved; otherwise they will be overlaid by new output.

### Running the Model

1. Left click on the button labeled "Run Model" in the Setup.xls workbook.
2. While the model is running, a DOS window will open up that will display the steps of the model as these run. The longest running step is the one in which the distribution of biogenic gas levels are generated for each cell.

*Run Time* will vary as a function of the computer. If the input data file contains 50,000 cells, a run on a 1.8 GHz PC with 1 GB RAM takes approximately 20 minutes.

*Space Requirements* vary depending on the output options chosen. The basic output will be approximately 65 MB. Options exist to write four detailed data files (described below), which increase storage requirements by an additional 6 GB.

### Results

1. StudyName.xls is the main output file. A description of the worksheets follows:
  - a. **Run\_Settings** is an output reproduction of Setup.xls plus a time stamp. We recommend that this sheet be compared with Setup.xls to ensure parameters were read correctly.
  - b. **Results** reproduces the cell input data and provides cell output consisting of the following variables:
    - (i) Basin Generation
    - (ii) Percent Convex
    - (iii) Gross Hydrate Stability Zone Thickness (HSZ) in meters
    - (iv) Generation (Gen)
    - (v) Dip Migration (DipMig)
    - (vi) Charge (Charge) in cubic meters
    - (vii) Undersaturated Zone Thickness (UnderSat) in meters
    - (viii) Net Hydrate Stability Zone Thickness (NetHSZ) in meters
    - (ix) Saturation (Sat)
    - (x) Volume in trillions of cubic meters (tcm) (Vol)
    - (xi) Volume in trillions of cubic feet (tcf) (Vol\_cuft)

For variable (iii) through (xi), the following statistics are computed: mean; standard deviation; the minimum; the 10, 20, 30, 40, 50, 60, 70, 80 and 90 percentiles; and the maximum. A total of 118 variables are written for each cell, including input variables.

c. **Aggregate** displays aggregate result by trial. The variables are:

- (i) Trial number
- (ii) Charge (sum over all cells) in tcm
- (iii) Concentration (cell average) (0 to 1)
- (iv) Net HSZ (cell average) in meters
- (v) Volume (sum over all cells) in tcm

2. If R has been installed, graphics and basic statistics are included as worksheets in the Results file as follows:

- a. concen – a density plot of concentration
- b. nethst – a density plot in original and log units of net HSZ
- c. charge\_mton – a density plot of charge in metric tons
- d. charge\_bcum – a density plot of charge in billions of cubic meters
- e. vol – a density plot in original and log units of volume
- f. fourway – a scatter plot matrix of concentration, netHSZ, charge and volume
- g. Statistics – summary statistics for concentration, netHSZ, charge and volume

Individual cell and trial files

Four files provide individual output information for each cell and each trial. The files are:

- 1. Volumect.csv for volume (units are tcm),
- 2. Nethszct.csv for net hydrate stability zone thickness,
- 3. Chargect.csv for charge (tcm) and
- 4. Concenct.txt for concentration (0 to 1)

These are extremely large as the number of records is the number of trials times the number of cells. The formation for each of the files is: Cell number, Basin ID, Latitude, Longitude, Trial number and volume. Sample output from volumect.csv is shown in Display 2. These files are optional (see Display 1).

**Display 2** Sample output from file volumect.csv.

Cell	BasinID	Latitude	Longitude	Trial	Volume
393	225	27.83477	-92.5248	95	7.12E-04
393	225	27.83477	-92.5248	216	6.42E-04
393	225	27.83477	-92.5248	249	4.59E-03
393	225	27.83477	-92.5248	287	4.22E-03
393	225	27.83477	-92.5248	382	2.43E-05
393	225	27.83477	-92.5248	434	5.85E-04
393	225	27.83477	-92.5248	502	8.67E-04
393	225	27.83477	-92.5248	711	7.23E-04

## Description of System

### Model Components

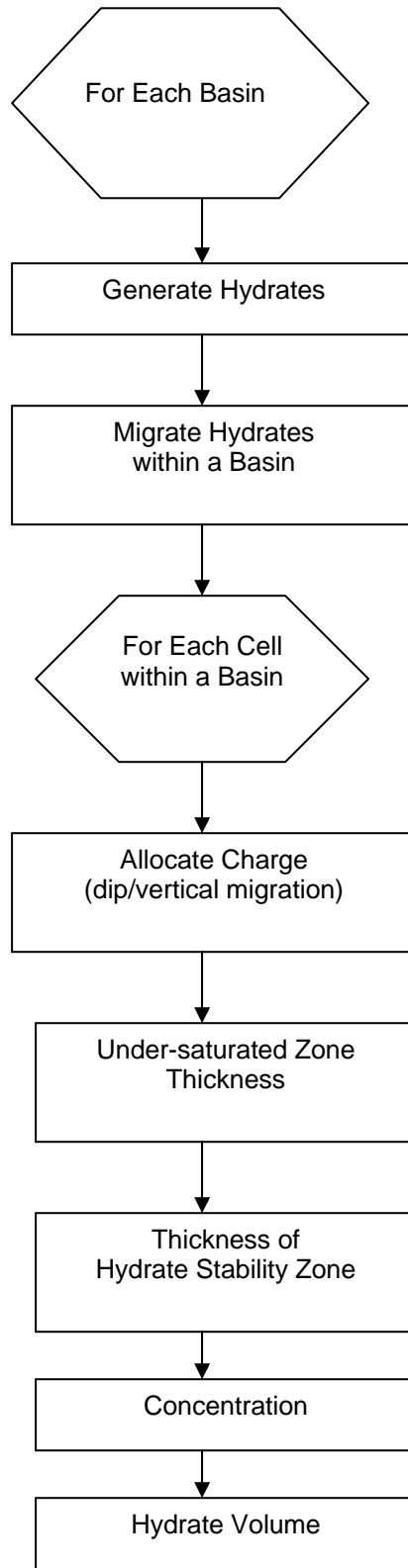
The model consists of a main program and 39 separate subprograms (functions subroutines). A flow chart and summary of these algorithms are presented later. These routines were programmed in FORTRAN version 90 and may be compiled by any compiler of this version or later. The compiled version is called GOM3.38. In addition, a simple R script<sup>23</sup> is provided that will read in output files for further graphical and/or statistical analysis.

Display 3 shows the general model structure for the GOM gas hydrate model. The generation and migration modules are executed for each basin. Gas hydrates are generated for each cell in a basin by replication of the model 1,000 times (trials). The migration module distributes hydrates across a basin within each trial to cells as a function of percent convexity within a cell. Once this allocation is made, subsequent modules are executed for each cell within a basin. In order of execution these modules are: charge, under-saturated zone thickness, hydrate stability zone thickness, concentration, and volume.

---

<sup>23</sup> R is an open source language. See <http://www.r-project.org>

**Display 3. System Flow Chart**



A brief description of each program is provided in the order of execution.

1. **main.f** Calls subprograms that read the data and parameter files, initializes curvature and arrays, saves parameters and then executes routines to generate hydrates. At the conclusion this program writes results.
2. **initran** (in ran.f) A function to generate (0,1) uniform random numbers.
3. **inputc** Reads parameters from Control.txt.
4. **inputd** (in input.f) Reads input data file InputData.txt.
5. **params** (in params.f) Creates random deviates of the parameters for each trial.
6. **outputp** (in outparams.f) Saves output of params in a file.
7. **initbasins** (in initbasins.f) Determines which cells are in each basin.
8. **curvature** (in curvature.f) Calculates relative curvature for each cell within each basin.
9. **generate** (in gener.f) Computes the generation amount for each trial, for each cell within each basin. Major subcomponents of this model are:
  - a. Estimating thickness of the five strata.
  - b. Computing midpoint thickness for each stratum and time.
  - c. Estimating sediment temperature for each stratum and time.
  - d. Generating a random deviate for the maximum initial production.
  - e. Computing midpoint shallow sand permeability for each stratum and time.
  - f. Computing shallow sand porosity for each stratum and time.
  - g. Computing midpoint shale permeability.
  - h. Computing average rock bulk permeability.
  - i. Scaling permeability by water bottom permeability.
  - j. Computing an intercept.
  - k. Computing generation potential for each stratum.
  - l. Integrating Arrhenius' Law over thickness to obtain incremental generation for each stratum and time.
  - m. Computing the cumulative generation for each stratum that does not exceed generation potential.
  - n. Computing the cumulative generation for the cell-trial.
10. **migration** (in migration.f)—Computes for each cell and trial within a basin computes migration volume as a function of amount generated (see generate) and percent convexity (see curvature).
11. **gencharge** (in charge.f)—Computes charge as a function of vertical migration or dip driven migration distribution.
12. **undersat** (in undersat.f)—Estimates undersaturated zone thickness.
13. **hsz** (in hsz.f)—Estimates thickness of hydrate stability zone (HSZ).
14. **concentration** (in concentration.f)—Calculates sand and shale porosities, total effective void space per meter of net HSZ by sand, shale and fractures and finally, the total void space available for charging.
15. **vols** (in vols.f)—Compute volume as a function of net HSZ thickness, cell size, saturation and charge. Final result is adjusted by migration efficiency.
16. **outputall** (in outputresults.f)—Writes results.txt file.